

Tests and Predictions of the Cosmic Microwave Background

Sujata Gupta

Doctor of Philosophy
The University of Edinburgh
2001



This thesis is my own composition except where indicated in the text.

August 11, 2002

Acknowledgements

I would like to thank my supervisors Alan Heavens and Arjun Berera for working with me, and for their help, guidance and occasional chocolate.

I would like to thank Andy Taylor for many interesting and useful discussions, for suggestions and guidance during the writing of this thesis, and general mathematical support.

Thanks also to Licia Verde, role-model and maths and computing tutor, especially in my first year when I really needed it.

And family, of course.

Abstract

The highly successful Hot Big Bang model, first hypothesised by Gamow in the 1940s, and supported by observations of an expanding Universe and by Big Bang nucleosynthesis, has been the standard cosmological model since the discovery of the cosmic microwave background radiation by Penzias and Wilson in 1964. There are, however, some crucial gaps in our understanding of the nature of the Universe. The Hot Big Bang model does not predict perturbations in the matter distribution of our Universe. The origin of the large scale structure, such as planets, stars and galaxies is not known. Further, we do not know how big the Universe is, how old, or what its main constituents are. There are a group of early Universe models which predict primordial fluctuations in the Universe, and using the most popular of these, ‘inflation’, the preliminary results of precision cosmology are giving the first glimpses of values for these mysterious quantities.

The cosmic microwave background radiation gives us a ‘snapshot’ of the very early Universe, an invaluable source of cosmological information. The Microwave Anisotropy probe (MAP) and the Planck Surveyor satellite will provide a map of the distribution of the cosmic microwave background over the sky, with a resolution approximately two orders of magnitude better than the previous satellite with a similar goal, which was the Cosmic Background Explorer satellite (COBE), launched in the late 1980s.

The aim of this thesis is to compare and contrast the predictions of early Universe models with respect to their predictions of the distribution of the cosmic microwave background radiation, as well as to garner information about cosmological parameters from the upcoming data. I approach this in three ways. The first goal is to develop statistical tools to detect non-Gaussianity in the cosmic microwave background, which would change the interpretation of the early Universe model. A significant detection of non-Gaussianity would conflict with the predictions of the simplest inflation model. The second aim is to develop very

rapid cosmological parameter estimation methods, should inflation be supported by the tests of Gaussianity, and the third to develop predictions for the cosmic microwave background for the warm inflation model.

Contents

1	Introduction	17
1.1	A Review of FRW Cosmology	17
1.1.1	The Horizon Problem	21
1.1.2	Unwanted Relics	21
1.1.3	The Spatial Flatness Fine-Tuning Problem	21
1.1.4	The Cosmological Constant Problem	23
1.1.5	Small Scale Inhomogeneity	25
1.2	Inflation	25
1.3	The Cosmic Microwave Background Anisotropies	38
1.3.1	Properties of Gaussian Fluctuations	39
1.3.2	The Angular Power Spectrum of the CMB	42
1.3.3	The Imprint of Cosmological Parameters on the CMB Power Spectrum	43
2	The Correlation Function of Peaks	53
2.1	Introduction	54
2.2	Method	56
2.2.1	Peaks on the surface of a sphere	56
2.3	Results	59
2.4	Correlation function vs bispectrum for string maps	60
2.5	On Further Testing The Test	67

2.6	Conclusions	68
3	Fast Parameter Estimation using MOPED	71
3.1	Introduction	71
3.2	Massive Lossless Data Compression	74
3.2.1	The Brute-Force Maximum Likelihood Method of Parameter Estimation From the CMB Power Spectrum	74
3.2.2	MOPED	78
3.3	Testing the MOPED method	80
3.4	Results	83
3.5	Conclusions	87
4	The Warm Inflation Bispectrum	89
4.1	Predictions of Non-Gaussianity for Standard Inflation	90
4.2	The Statistics of a Warm Inflation Generated Perturbation Spectrum	93
4.2.1	Warm Inflation Dynamics	93
4.2.2	The Warm Inflation Bispectrum	97
4.3	Comparisons with The Predictions of Other Models	100
4.3.1	Estimating the Magnitude of the Non-Gaussianity	100
4.3.2	The Bispectrum of the Cosmic Microwave Background	103
4.4	Conclusions	105
5	Conclusions	107
A	Measuring the Hubble Constant	121
B	Robertson-Walker Metric	123
C	The Friedmann Equation	125
D	Energy and Length Units	127

D.1	Energy Units	127
D.2	Length Units	128
E	Derivation of Formalism for Slow-Roll Inflation	129
E.1	Deriving the equation of motion	129
E.2	Deriving the Alternate Form of the Slow-Roll Conditions	130
F	Solving the Horizon Problem with Inflation	131
G	The Bispectrum of a Gaussian Field	133
H	The Thermal Property of the CMB	135
I	The Silk Damping Scale	137
J	Calculating the Variance of the Bispectrum Estimator	139
K	The Langevin Equation	141

1	Introduction
2	1.1 The Problem
3	1.2 The Solution
4	1.3 The Algorithm
5	1.4 The Complexity
6	1.5 The Implementation
7	1.6 The Results
8	1.7 The Conclusion
9	1.8 The Acknowledgements
10	1.9 The References
11	1.10 The Appendix
12	1.11 The Bibliography
13	1.12 The Index
14	1.13 The Glossary
15	1.14 The Summary
16	1.15 The Abstract
17	1.16 The Keywords
18	1.17 The Author's Address
19	1.18 The Author's Biography
20	1.19 The Author's Contact Information
21	1.20 The Author's Email Address
22	1.21 The Author's Phone Number
23	1.22 The Author's Fax Number
24	1.23 The Author's Postal Address
25	1.24 The Author's City
26	1.25 The Author's State
27	1.26 The Author's Country
28	1.27 The Author's Zip Code
29	1.28 The Author's Birth Date
30	1.29 The Author's Birth Place
31	1.30 The Author's Education
32	1.31 The Author's Research Interests
33	1.32 The Author's Current Position
34	1.33 The Author's Previous Positions
35	1.34 The Author's Awards and Honors
36	1.35 The Author's Publications
37	1.36 The Author's Patents
38	1.37 The Author's Grants
39	1.38 The Author's Collaborations
40	1.39 The Author's Mentors
41	1.40 The Author's Mentees
42	1.41 The Author's Professional Memberships
43	1.42 The Author's Conferences
44	1.43 The Author's Workshops
45	1.44 The Author's Seminars
46	1.45 The Author's Lectures
47	1.46 The Author's Invited Talks
48	1.47 The Author's Keynotes
49	1.48 The Author's Plenary Talks
50	1.49 The Author's Panel Discussions
51	1.50 The Author's Roundtable Discussions
52	1.51 The Author's Debates
53	1.52 The Author's Debates on Ethics
54	1.53 The Author's Debates on Policy
55	1.54 The Author's Debates on Law
56	1.55 The Author's Debates on Society
57	1.56 The Author's Debates on Culture
58	1.57 The Author's Debates on Religion
59	1.58 The Author's Debates on Philosophy
60	1.59 The Author's Debates on Science
61	1.60 The Author's Debates on Technology
62	1.61 The Author's Debates on Environment
63	1.62 The Author's Debates on Energy
64	1.63 The Author's Debates on Transportation
65	1.64 The Author's Debates on Infrastructure
66	1.65 The Author's Debates on Urban Planning
67	1.66 The Author's Debates on Architecture
68	1.67 The Author's Debates on Design
69	1.68 The Author's Debates on Art
70	1.69 The Author's Debates on Music
71	1.70 The Author's Debates on Literature
72	1.71 The Author's Debates on Film
73	1.72 The Author's Debates on Television
74	1.73 The Author's Debates on Radio
75	1.74 The Author's Debates on Journalism
76	1.75 The Author's Debates on Public Relations
77	1.76 The Author's Debates on Marketing
78	1.77 The Author's Debates on Advertising
79	1.78 The Author's Debates on Sales
80	1.79 The Author's Debates on Customer Service
81	1.80 The Author's Debates on Human Resources
82	1.81 The Author's Debates on Training
83	1.82 The Author's Debates on Development
84	1.83 The Author's Debates on Performance
85	1.84 The Author's Debates on Leadership
86	1.85 The Author's Debates on Management
87	1.86 The Author's Debates on Organization
88	1.87 The Author's Debates on Strategy
89	1.88 The Author's Debates on Innovation
90	1.89 The Author's Debates on Entrepreneurship
91	1.90 The Author's Debates on Business
92	1.91 The Author's Debates on Economics
93	1.92 The Author's Debates on Finance
94	1.93 The Author's Debates on Accounting
95	1.94 The Author's Debates on Law
96	1.95 The Author's Debates on Politics
97	1.96 The Author's Debates on History
98	1.97 The Author's Debates on Geography
99	1.98 The Author's Debates on Environmental Science
100	1.99 The Author's Debates on Social Science
101	1.100 The Author's Debates on Humanities

List of Figures

1.1	An illustration of the timescales over which universes with different FRW geometries evolve	23
1.2	A FRW timeline diagram. The subscript ‘eq’ represents the epoch of radiation–matter equality. The subscript ‘ Λ ’ represents the epoch of matter–cosmological constant equality.	25
1.3	A sketch illustrating the changing potential during a first order phase transition.	33
1.4	An illustration, not to scale, of the shape of the potential required for slow roll inflation.	34
1.5	Illustration of the timeline with inflation; the subscript ‘reh’ denotes the reheating era.	36
1.6	An electron with momentum p Compton scatters off a photon with momentum k .	44
1.7	The shape of the Planck radiation curve, of energy density against frequency, for a blackbody of temperature of 3300K	45
1.8	The photon pressure from Thompson-Compton scattering in the coupled photon-baryon fluid resists gravitational compression. As the baryonic matter first drops into the well, at sound horizon exit, the fluid begins to compress and photon pressure affects the potential, causing it to begin to decay. However the highly compressed fluid re-expands, reaches a maximum and then recollapses, the initial compression driving the oscillations.	46
1.9	Diagram illustrating the way the size of a fluctuation imprints on the microwave background.	47

- 1.10 Plot of simulated CMB power spectra for varying hot dark matter content. The the power spectrum plotted in blue contains a 2% proportion of hot dark matter, cold dark matter density of 0.25 and baryon fraction 0.03. The power spectrum plotted in purple contains the highest proportion of hot dark matter, an unchanged CDM density of 0.25 and baryon fraction 0.01. The turquoise line was generated with no hot dark matter content and baryon fraction 0.05. All of the three simulations have a total density of 1. 49
- 1.11 Plot of simulated CMB power spectra for varying scalar spectral indices. The blue line has $n = 1$, the purple line has $n = 1.05$, and the turquoise line has $n = 0.95$. All three spectra have been normalized to match the COBE observations at angular multipole $l = 2$ 51
- 1.12 Plot of simulated CMB power spectra for varying cold dark matter content. The the power spectrum plotted in blue contains a 25% proportion of cold dark matter, with Ω_Λ equal to 0.7 and a baryon fraction of 0.05. The purple power spectrum contains the highest proportion of cold dark matter, 40%, with Ω_Λ equal to 0.56 and baryon fraction 0.04. The power spectrum plotted in turquoise has the lowest CDM fraction of 10%, $\Omega_\Lambda = 0.84$ and baryon fraction 0.06. So again, all three simulated power spectra have total density equal to 1. 51
- 1.13 Plot of simulated CMB power spectra for different values of spatial curvature. The purple line shows the power spectrum for an $\Omega = 1$ universe. The universe of the blue power spectrum has a total density of 0.8. The turquoise line has the lowest total density of 0.6. I reduced all of the quantities contributing to the total density proportionally, so this plot is somewhat altered by other physical effects, such as the results of reducing the baryon content of a universe. 52
- 1.14 This plot of the $\Omega_m - \Omega_\Lambda$ slice of likelihood space is taken from Tegmark *et al.* (2001). Here, data from COBE and various other CMB experiments have been combined with the IRAS Point Source Catalogue Redshift dataset, and also with the predictions from Big Bang Nucleosynthesis, the favoured model for the formation of matter. 52

2.1	(Solid line) The correlation function for peaks above a $+1\sigma$ threshold, in a mixed dark matter model with CDM, vacuum and baryon density parameters $\Omega_{CDM} = 0.8$, $\Omega_\nu = 0.15$ and $\Omega_B = 0.05$. Hubble constant is $H_0 = 60 \text{ km s}^{-1} \text{ Mpc}^{-1}$. For comparison, the flat-sky results of Heavens & Sheth (1999) are shown dotted. The results coincide to an accuracy of better than 0.004. . . .	60
2.2	As Fig. 2.1, but at larger angle separations between 3.3 and 16.7 degrees. . .	61
2.3	62
2.4	Discrete box imposed on CMB sky.	62
2.5	The triangles in this figure are equivalent for bispectrum evaluation, therefore $\langle \delta(\mathbf{k}_3)\delta(\mathbf{k}_2)\delta(\mathbf{k}_1) \rangle = \langle \delta(\mathbf{k}_{-1})\delta(\mathbf{k}_{-2})\delta(\mathbf{k}_{-3}) \rangle = \langle \delta(\mathbf{k}_1^*)\delta(\mathbf{k}_2^*)\delta(\mathbf{k}_3^*) \rangle$. Symmetry leaves only the real part of the bispectrum.	63
2.6	Equilateral triangle of wavevectors centred on origin.	64
2.7	Regions of independent information for the equilateral triangle case.	64
2.8	Zero-area triangle.	65
2.9	The equilateral bispectrum as estimated from map with string foreground and Gaussian temperature on last-scattering surface (solid), and cosmic r.m.s. (dotted).	65
2.10	The correlation function of peaks above 1σ calculated from the map of Fig. 2.3. Errors are Poisson, and hence underestimates. Superimposed is the correlation function from a Gaussian map with the same power spectrum. Note the excess of string peaks around 10–15 arcminutes.	66
2.11	The number of peaks in one of the string maps, along with the expected number from a Gaussian field with the same power spectrum.	67
2.12	Correlation function of peaks above the mean in a (non-Gaussian) χ^2 field. The power spectrum of the underlying Gaussian field is a mixed dark matter model.	68
2.13	The correlation function of peaks when the relative Gaussian emission is increased to become comparable to the foreground lensing effects.	69

3.1	Optimised MOPED weighting vectors for a fiducial model with $H_0 = 65 \text{ km s}^{-1}\text{Mpc}^{-1}$, $\Omega_{CDM} = 0.254$ and $\Omega_\Lambda = 0.7$. The parameter ordering (see text) is Ω_Λ , H_0 and Ω_{CDM} . The MOPED vectors will depend on the choice of order for a particular noise realisation. The effect this has on the contours of the likelihood plot is only pronounced for a small number of multipole values ~ 30 .	81
3.2	Simulated realisation of the CMB power used in the analysis.	82
3.3	The true model spectrum (solid), with $H_0 = 65 \text{ kms}^{-1}\text{Mpc}^{-1}$, $\Omega_\Lambda = 0.7$ and $\Omega_{CDM} = 0.254$, with Gaussian noise and smoothed in ℓ with a Gaussian of width $\Delta\ell = 5$. Also shown (dotted) is the fiducial model used in the data compression for Fig.3.6: $H_0 = 60.8 \text{ kms}^{-1}\text{Mpc}^{-1}$, $\Omega_\Lambda = 0.732$ and $\Omega_{CDM} = 0.254$, both smoothed with a Gaussian of width $\Delta\ell = 5$. The boxes show the data points used for the likelihood calculations.	83
3.4	Likelihood surface for Ω_Λ and H_0 obtained from the the full dataset. This dataset consists of 150 power spectrum estimates from $\ell = 2, \dots, 1500$ in steps of 10, smoothed over a scale of $\Delta\ell = 5$. The true model is labelled with a square	84
3.5	Likelihood surface for Ω_Λ and H_0 obtained from the the 3 MOPED components. The fiducial model used for the data compression coincides with the true model in this case, and both are marked by a square. The likelihood contours are too small to see individually for this experiment; the outer contour contains 99.99% of the probability, assuming uniform priors.	84
3.6	Likelihood surface for Ω_Λ and H_0 obtained from the the 3 MOPED components. The fiducial model used for the data compression no longer coincides with the true model, and is marked by a triangle. Note that the method still recovers the correct model (square).	85
3.7	Likelihood from the full power spectrum, as in Fig. 3.4, but restricted to $\ell \leq 300$ in steps of 10, to illustrate the size of the error bars. The contours represent confidence limits of 99.99%, 99%, 95.4%, 90%, and 68%. The true model is labelled with a square.	85
3.8	As Fig. 3.7, but showing the likelihood from MOPED components. Note that the error bars are comparable.	86
3.9	Showing the likelihood, as Fig. 3.7, but with a different fiducial model and MOPED components from Fig. 3.8.	86

List of Tables

Introduction	66
2.1	66
1.1 A Review of FRW Cosmology	
1.1.1	
1.1.2	
1.1.3	
1.1.4	
1.1.5	
1.1.6	
1.1.7	
1.1.8	
1.1.9	
1.1.10	
1.1.11	
1.1.12	
1.1.13	
1.1.14	
1.1.15	
1.1.16	
1.1.17	
1.1.18	
1.1.19	
1.1.20	
1.1.21	
1.1.22	
1.1.23	
1.1.24	
1.1.25	
1.1.26	
1.1.27	
1.1.28	
1.1.29	
1.1.30	
1.1.31	
1.1.32	
1.1.33	
1.1.34	
1.1.35	
1.1.36	
1.1.37	
1.1.38	
1.1.39	
1.1.40	
1.1.41	
1.1.42	
1.1.43	
1.1.44	
1.1.45	
1.1.46	
1.1.47	
1.1.48	
1.1.49	
1.1.50	
1.1.51	
1.1.52	
1.1.53	
1.1.54	
1.1.55	
1.1.56	
1.1.57	
1.1.58	
1.1.59	
1.1.60	
1.1.61	
1.1.62	
1.1.63	
1.1.64	
1.1.65	
1.1.66	
1.1.67	
1.1.68	
1.1.69	
1.1.70	
1.1.71	
1.1.72	
1.1.73	
1.1.74	
1.1.75	
1.1.76	
1.1.77	
1.1.78	
1.1.79	
1.1.80	
1.1.81	
1.1.82	
1.1.83	
1.1.84	
1.1.85	
1.1.86	
1.1.87	
1.1.88	
1.1.89	
1.1.90	
1.1.91	
1.1.92	
1.1.93	
1.1.94	
1.1.95	
1.1.96	
1.1.97	
1.1.98	
1.1.99	
1.1.100	

Chapter 1

Introduction

I will outline in this thesis three research projects consisting of tests, analysis methods and predictions of early Universe models using the cosmic microwave background radiation. In Chapter 1, I shall introduce the theoretical background to my work: standard cosmology, inflation, and the physics of the cosmic microwave background radiation. In Chapter 2, I introduce an all-sky test of the Gaussianity of the cosmic microwave background radiation. In Chapter 3, I introduce a data compression algorithm for cosmic microwave background data. I review the last of my research topics, the prediction of the level of non-Gaussianity for the warm inflation model of the early Universe, in Chapter 4. Chapter 5 will contain a synopsis and discussion of the three projects.

1.1 A Review of FRW Cosmology

The observed Universe is, to a high degree, isotropic on large scales, expanding and assumed to be homogeneous. Luminous matter in the sky, neglecting the galactic plane, is distributed largely isotropically, but of course light does not necessarily trace mass. Observations of radio galaxies and quasars are also isotropic on large scales suggesting isotropy of the younger, more distant Universe (Cress, 1999; Outram *et al.*, 2001; Colless & 2dF Galaxy Redshift Survey Team, 2000) The strongest evidence for the isotropy of the Universe at early times comes from the cosmic microwave background radiation, henceforth referred to as the CMB. Apart from the dipole anisotropy observed due to the motion of the Earth, the temperature difference between two antennae separated by angles ranging from 10° to 180° is smaller than 0.01% (Penzias & Wilson, 1965; Smoot *et al.*,

1991). This indicates that at the time of last scattering of photons in the CMB approximately 2×10^5 yrs after the big bang, the Universe was highly isotropic, and homogeneous in the region between us and the start off point of the CMB photons. Also the CMB suggests that the *expansion* of the Universe is isotropic, as any anisotropy of the expansion would lead to a corresponding temperature anisotropy in the CMB.

The Copernican Principle states, without observational evidence, that we are not at the centre of the Universe and that there is nothing special about our view of cosmological expansion. This assumption of translational symmetry when taken together with the rotational symmetry of the observed isotropy implies homogeneity. Homogeneity and isotropy together constitute the Cosmological Principle.

The expansion of the Universe is inferred primarily from the observed light from galaxies (Slipher, 1924; Hubble, 1927). Nearly all of the galaxy spectra measured in all directions are red-shifted. The redshift, z , of a galaxy is related to the expansion of the Universe by the power series (Kolb & Turner, 1990)

$$H_0 d_L = z + \frac{1}{2}(1 - q_0)z^2 + \dots, \quad (1.1)$$

where d_L is the luminosity distance of the galaxy

$$d_L = \left(\frac{\mathcal{L}}{4\pi F} \right)^{\frac{1}{2}}, \quad (1.2)$$

\mathcal{L} =luminosity F =measured flux

and H_0 is the present value of the Hubble parameter. $a(t)$ is the scale factor corresponding to the size of the Universe. The subscript '0' denotes the present value of a quantity.

$$H_0 \equiv \left. \frac{1}{a} \frac{da}{dt} \right|_{t_0}, \quad (1.3)$$

$$\begin{aligned} q_0 &= \text{deceleration parameter} \\ &= -\frac{\ddot{a}(t_0)}{a(t_0)} H_0^2. \end{aligned} \quad (1.4)$$

There is some variance between different estimates of the Hubble constant. This uncertainty (Freedman *et al.*, 2001) is represented by a factor of h

$$\begin{aligned} H_0 &= 100h \text{ km s}^{-1}\text{Mpc}^{-1} \\ 0.64 &\lesssim h \lesssim 0.80 \end{aligned} \quad (1.5)$$

The hot big bang model, henceforth referred to as the HBB model (also known as the FRW model), is the mainstay of modern cosmology. It is based on the Robertson-Walker metric, whose high degree of symmetry is suited to modelling a homogeneous and isotropic space, and on the Friedmann equations. The form of the line element, the shortest spacetime distance between two points, of the Robertson-Walker metric varies with the global curvature of the Universe (Peebles, 1993), Appendix B,

$$ds^2 = c^2 dt^2 - a(t)^2 [dr^2 + D^2 d\Omega], \quad (1.6)$$

where $d\Omega = d\theta^2 + \sin^2 \theta d\phi^2$, and c is the speed of light. The above quantity can be rewritten as

$$= a(\eta)^2 [c^2 d\eta^2 - dr^2 - D^2 d\Omega]. \quad (1.7)$$

This last line is the line element in *comoving* coordinates : $dt = a(\eta)d\eta$, and η is known as conformal time. r , θ , and ϕ are 3-d comoving coordinates on the hypersurface $\eta = \text{constant}$ and if this space is closed, with positive curvature, R , a measure of the curvature, is real and finite, and D , called the comoving angular diameter distance, is equal to $R \sin \frac{r}{R}$. If open, with negative curvature, $R^{-2} < 0$ and D is $|R| \sinh \frac{r}{|R|}$; for a flat Universe D is simply equal to r .

The Friedmann equations can be arrived at from the Einstein equations and using the energy-momentum tensor of the Universe, which defines the energetic behaviour of the Universe given its constituents (Appendix C).

$$\frac{1}{a(t)} \frac{d^2 a}{dt^2} = -\frac{4\pi G}{3} \left(\rho + \frac{3p}{c^2} \right) + \frac{\Lambda}{3} \quad (1.8)$$

$$\frac{1}{a(t)^2} \left(\frac{da}{dt} \right)^2 = \frac{8\pi G \rho}{3} + \frac{c^2}{R^2 a^2} + \frac{\Lambda}{3}, \quad (1.9)$$

where Λ is the cosmological constant.

There is another quantity that corresponds to spatial curvature in the case where there is no cosmological constant contribution,

$$\Omega = \frac{\rho}{\rho_c}, \quad (1.10)$$

where ρ is the density of the Universe and ρ_c is the critical density,

$$\rho_c = \frac{3H^2}{8\pi G}. \quad (1.11)$$

The Friedmann equation for the special case of flat space and zero cosmological constant could thus be written:

$$\frac{1}{R^2 H^2 a^2} = 1 - \Omega, \quad (1.12)$$

which shows the correspondence of

flat	to	$\Omega = 1$
closed		$\Omega > 1$
open		$\Omega < 1$.

The stress energy relation of the components making up the energy content of the Universe is given by their equation of state

$$p = \omega \rho c^2 \quad (1.13)$$

pressure = $\omega \times$ energy density \times speed of light squared.

If ω is constant the evolution of ρ is given by

$$\rho \propto a^{-3(1+\omega)}. \quad (1.14)$$

The radiation-dominated early Universe has equation of state

$$p = \frac{1}{3}\rho c^2, \quad (1.15)$$

and the density evolves as $\rho \propto a^{-4}$.

The matter dominated Universe has

$$p = 0, \quad (1.16)$$

so $\rho \propto a^{-3}$.

The Hot Big Bang model provides a framework for the Universe which is remarkably successful, but it has certain shortcomings, which I turn to next.

1.1.1 The Horizon Problem

The Universe on very large scales is very smooth. After subtraction of our motion, the CMB is uniform to better than 0.01% but the present Hubble volume contained about 10^5 causally disconnected regions at the time of last scattering of photons in the CMB (Kolb & Turner, 1990). So within the HBB model micro-physical processes could not have smoothed out any temperature fluctuations.

1.1.2 Unwanted Relics

There are a variety of massive stable particle species, for example the gravitino, that are hypothesized by various particle physics models to be produced in the high temperatures early in the Universe in an abundance which is not observed now. (Ellis *et al.* (1986), de Carlos *et al.* (1993), Banks *et al.* (1994)).

1.1.3 The Spatial Flatness Fine-Tuning Problem

The development with time of an FRW universe does not cause its curvature to change if it has a density $\Omega = \rho/\rho_c$ exactly equal to one. If, however, the curvature of an FRW universe is slightly positive or negative, this positive or negative curvature will increase with time. If the Universe now was found to be a certain amount open or closed, the initial conditions of the FRW model would have to be finely-tuned to have a precise small deviation from flatness near the HBB. If the Universe is measured to have exactly zero spatial curvature, the initial conditions of the FRW model would have to be finely tuned to exactly flat at the HBB. The HBB model does not predict a flat or close to flat Universe at present times with general initial conditions.

The spatial flatness of the Universe has been estimated from observations, finding a flat or very close-to-flat Universe. The recent results from balloon measurements of the cosmic microwave background estimated Ω to be between 0.7 and 1.25 (Balbi *et al.*, 2001a,b; Stompor *et al.*, 2001; de Bernardis *et al.*, 2001).

When the Universe is radiation dominated, the relation between the energy density and the scale factor is

$$\rho \propto a^{-4}. \quad (1.17)$$

Including other forms of relativistic matter, the energy density is given in terms

of the temperature of the Universe by

$$\rho_r = \alpha \left(\frac{\pi^2}{15} \right) T_\gamma^4. \quad (1.18)$$

(α multiplies the energy density of the photons, expanding the excess of non-photon relativistic matter, and according to the standard model of particle physics $\alpha = 1.68$ (Peacock, 1999).) So

$$a(t) \propto T^{-1}. \quad (1.19)$$

The Friedmann equation (1.9) without cosmological constant has the form

$$\frac{1}{a(t)^2} \left(\frac{da}{dt} \right)^2 = \frac{8\pi G\rho}{3} + \frac{c^2}{R^2 a^2}. \quad (1.20)$$

The characteristic timescale from these equations is the Planck time,

$$t_{\text{pl}} \simeq \left(\frac{\hbar G}{c^5} \right)^{\frac{1}{2}} \simeq 10^{-43} \text{ s}, \quad (1.21)$$

where \hbar is Planck's constant, and G is the universal gravitational constant. In a closed radiation dominated universe the expected time of maximum expansion from the hot big bang is of the order of the Planck time, followed by a rapid collapse (Coles & Lucchin, 1995).

For an open universe the curvature term of the Friedmann equation, $(Ra)^{-2}$, dominates over the gravitation term, $\frac{1}{3}(8\pi G\rho)$, within a time of the order of the Planck time, if the two terms begin with comparable size.

The estimated age of the Universe is about $10^{10} \text{ yrs} \sim 10^{60} t_{\text{pl}}$. For the Universe to have survived this long Ω would have to be very close to 1, so that

$$\left(\frac{\dot{a}}{a} \right)^2 \simeq \frac{8\pi G\rho}{3}. \quad (1.22)$$

Estimated values of Ω , at this present time, range from 0.7 and 1.25. From equation (1.20),

$$a^2 \rho (\Omega^{-1} - 1) = \frac{3}{8\pi G R^2} = \text{constant}. \quad (1.23)$$

During radiation domination, equation (1.17),

$$|\Omega^{-1} - 1| \propto a^3. \quad (1.24)$$

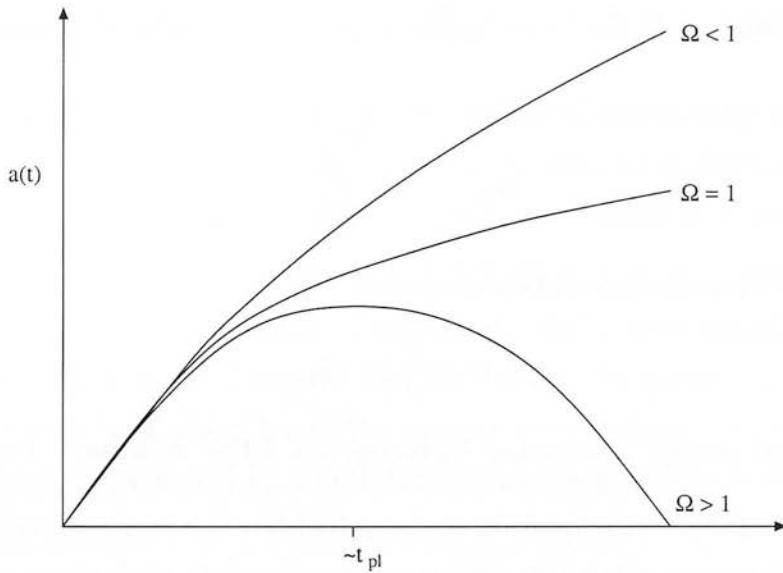


Figure 1.1: An illustration of the timescales over which universes with different FRW geometries evolve

This relation shows that if Ω was to begin at any amount either greater than or less than one, the Universe would become progressively less flat with time. So for the FRW model to work the very early value of Ω would need to be fine-tuned to almost exactly one. This analysis assumes no cosmological constant contribution. The observational measurements of the flatness of the Universe, from the first *acoustic peak* of the cosmic microwave background anisotropy power spectrum, is also influenced by the proportion of the vacuum energy in the Universe. The effects on the power spectrum of this degeneracy are outlined in Section 1.3.

1.1.4 The Cosmological Constant Problem

A more general, relativistically covariant, form of Einstein's equations includes a *cosmological constant* Λ (Appendix C). If the energy density of the Universe were made up solely of this cosmological constant, a *de Sitter* universe, the scale factor of the Universe would increase exponentially. Present measurements of the Universe do suggest that there is a significant cosmological constant constituent to our Universe. But the Friedmann equations show that any Λ term will quickly dominate over other forms of energy density. In fact it is highly likely, given general initial conditions, that the Universe would have begun to accelerate exponentially a long time ago and appear nothing like it does now.

The cosmological term is equivalent to an additional form of stress energy, for

reasons expanded on in Section 1.2,

$$\begin{aligned}\rho_{\text{vac}} &= \frac{\Lambda}{8\pi G}, \\ p_{\text{vac}} &= -\frac{\Lambda}{8\pi G}.\end{aligned}\tag{1.25}$$

So the vacuum energy has equation of state

$$\omega = \frac{p}{\rho} = -1,\tag{1.26}$$

and a vacuum energy *dominated* Universe has FRW solutions, from equation (1.14),

$$\rho_{\text{vac}} = \text{constant}\tag{1.27}$$

$$H = \left(\frac{8\pi G\rho_{\text{vac}}}{3}\right)^{\frac{1}{2}} = \text{constant}\tag{1.28}$$

$$a(t) \propto \exp(Ht),\tag{1.29}$$

so the expansion accelerates with time.

Again, looking at the Friedmann equation (1.9),

$$\left(\frac{\dot{a}}{a}\right)^2 = \frac{8\pi G\rho}{3} + \frac{c^2}{R^2 a^2} + \frac{\Lambda}{3},$$

the density term evolves as a^{-4} during radiation domination and a^{-3} during matter domination. The curvature term evolves as a^{-2} , whereas the vacuum energy term remains constant. Therefore, according to the HBB model, even a small cosmological constant constituent in the early Universe will quickly come to dominate the energy density.

The Supernova Cosmology project measuring an extinction of the light of distant supernovae (Perlmutter *et al.*, 1999) discovered together with CMB and large scale structure measurements that the Universe appears to just now be beginning to accelerate. The components of the Universe would correspondingly be in a ratio of approximately 30% matter to 70% cosmological constant. That the initial makeup of the Universe must be exactly such that the Universe should begin to accelerate at this time is a second fine tuning problem.

1.1.5 Small Scale Inhomogeneity

The HBB model models a smooth Universe. The Universe may be smooth on very large scales, but visible matter in the sky on smaller scales is clumped into galaxies, galaxy clusters and even superclusters, with voids in between them.

The Cosmic Background Explorer satellite (COBE) in 1992 discovered fluctuations in the microwave background (Davis *et al.*, 1992), corresponding to fluctuations in the density of the Universe, age 3×10^5 yrs. As gravity is the only universally attractive long range force, the present cosmological structure observed in the sky must be preceded by small density inhomogeneities in the early Universe. These grew where the stabilizing effect of the pressure of the homogeneous and isotropic *mean* fluid of the Universe was much smaller than the tendency of density perturbations to collapse due to self-gravity. Observations of the CMB also show fluctuations propagating over scales larger than the physical horizon at that time, similar to the horizon question of Section (1.1.1).

The FRW model contains no information about how these primeval fluctuations in the energy density of the Universe originated.

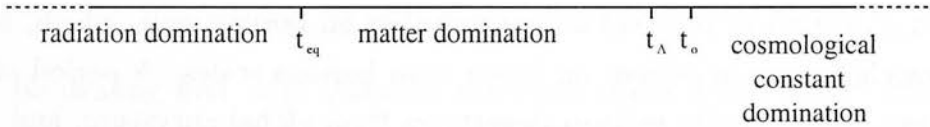


Figure 1.2: A FRW timeline diagram. The subscript ‘eq’ represents the epoch of radiation-matter equality. The subscript ‘A’ represents the epoch of matter-cosmological constant equality.

1.2 Inflation

Particle physics provides a possible solution to the above problems with a scenario in which early in the life of the FRW Universe there is a period of exponential expansion. *Inflation* hypothesizes that the present observable Universe is inside what was a causally connected and thermalized region of the Universe, which was inflated to greater than the size of the **particle** horizon.

The particle horizon is the proper distance that can be travelled by light since the initial singularity of the FRW model. It is the effective distance across which

causal processes can act,

$$R_H(t) = a(t) \int_0^t \frac{cdt'}{a(t')}. \quad (1.30)$$

The comoving **event** horizon is the following quantity,

$$R_{EH}(t_0) = \int_{t_0}^{\infty} \frac{cdt'}{a(t')}. \quad (1.31)$$

In an FRW universe without a cosmological constant constituent, even an FRW universe that has been interrupted by a period of exponential expansion, the comoving distance a particle can travel from now to $t = \infty$ is infinite. In an exponentially expanding universe where the expansion goes on forever, $R_{EH} = c/a_o H$ and is a finite event horizon. A similar measure

$$R_{\text{hor}} = \int_0^{t_e} \frac{cdt'}{a(t')}, \quad (1.32)$$

where t_e represents the time at the end of inflation, gives a measure of the comoving size of homogenized regions of space at the end of inflation.

When inflation occurs the quantum fluctuations present in the energy distribution lead to a spectrum of physical inhomogeneities on horizon exit, which, because of this mechanism, are present on larger than horizon scales. A period of exponential expansion greatly reduces departures from global curvature, and dilutes the concentration of the massive stable particle species overproduced in the early Universe.

I will begin my review of inflation by introducing the canonical quantum field theory formalism. Recall the operators of non-relativistic quantum mechanics (Rae, 1980; Landau & Lifshitz, 1977); the energy operator $\hat{E} \equiv i\hbar \frac{\partial}{\partial t}$ and the momentum operator $\hat{\mathbf{p}} \equiv -i\hbar \nabla$, which both act on a wavefunction $\phi(\mathbf{x}, t)$. The relation, for a non-relativistic particle $E = \frac{p^2}{2m}$ leads to the familiar Schrödinger equation,

$$i\hbar \frac{\partial \phi(\mathbf{x}, t)}{\partial t} = -\frac{\hbar^2 \nabla^2 \phi(\mathbf{x}, t)}{2m}. \quad (1.33)$$

Recall also the two postulates of Special Relativity

- All inertial frames are equivalent for the formulation of physical laws.
- Velocity of light takes the same value, c , with respect to all inertial frames.

The mathematical setup which corresponds to this is the representation of all physical quantities being invariant under *Lorentz transformations*. Lorentz transforms being defined to preserve the quantity:

$$ds^2 = c^2 dt^2 - dx^2 - dy^2 - dz^2, \quad (1.34)$$

where dx , dy , dz and dt represent displacements along three spatial axes and the time line of the frame.

ds is the *spacetime distance* from (ct, x, y, z) to $(ct + cdt, x + dx, y + dy, z + dz)$, otherwise known as the invariant interval.

The Lorentz transform will be represented from now on as Λ_{ν}^{μ} , a 4×4 tensor. The Greek indices μ, ν, ρ etc. run from 0 to 3, and Latin letters i, j, k etc. run from 1 to 3. If I represent the time coordinate, ct , as x^0 , and the spatial coordinates as $x^i = (x, y, z)$, the invariant interval can be represented by

$$ds^2 = g_{\mu\nu} dx^{\mu} dx^{\nu}. \quad (1.35)$$

The Einstein summation convention, meaning repeated indices are summed over, is used here. The tensor $g_{\mu\nu}$ is the metric, which incorporates a description of the geometry of spacetime. The geometry of a Friedmann-Robertson-Walker universe is described by the metric (1.6).

I shall be dealing first with distance and time scales which are of importance for trajectories and interactions of individual particles. On such scales, in the absence of a strong gravitational field, the effects of the expansion and possible curvature of the Universe are negligible, so the metric used for this section is the *Minkowski metric*:

$$g^{\mu\nu} = g_{\mu\nu} \equiv \begin{pmatrix} 1 & 0 & 0 & 0 \\ 0 & -1 & 0 & 0 \\ 0 & 0 & -1 & 0 \\ 0 & 0 & 0 & -1 \end{pmatrix}. \quad (1.36)$$

Also I will be representing tensors with raised and with lowered indices. The metric acts to raise and lower indices in this fashion

$$x_{\nu} = x^{\mu} g_{\mu\nu} = (ct, -x, -y, -z). \quad (1.37)$$

Also, following trivially from (1.36), is the following relation:

$$g^{\mu\nu} g_{\nu\eta} = \delta_{\eta}^{\mu}, \quad (1.38)$$

the Kronecker Delta.

Thus, returning to the point of all the formalism; x^μ , a vector, the spacetime position of a particle in one reference frame, becomes x'^μ when represented in terms of coordinates of another inertial frame, and

$$x^\mu \rightarrow x'^\mu = \Lambda^\mu_\nu x^\nu. \quad (1.39)$$

These are otherwise known as *contravariant vectors*. Scalars transform as

$$\phi(x') = \phi(x). \quad (1.40)$$

Covectors, otherwise known as *covariant vectors*, transform as

$$w_\alpha \rightarrow w'_\alpha = (\Lambda^{-1})^\beta_\alpha w_\beta(x). \quad (1.41)$$

Finally, and most importantly, defining the 4D *dot product*

$$x \cdot v \equiv x^\mu v_\mu = g_{\mu\nu} x^\mu v^\nu, \quad (1.42)$$

which transforms as a scalar.

How does energy transform in this construct? Considering the velocity 4-vector of a particle $u^\mu \equiv \frac{dx^\mu}{d\tau}$, where $d\tau$ is the *proper time* $d\tau = \frac{ds}{c}$, the time recorded by an observer at rest in this frame,

$$u^\mu = \left[\frac{1}{1 - \frac{\mathbf{v}^2}{c^2}} \right]^{\frac{1}{2}} (c, \mathbf{v}), \quad (1.43)$$

\mathbf{v} being the 3-velocity of the particle. In the rest frame of the particle, $\mathbf{v} = 0$. Thus in the rest frame of the particle $u \cdot u = c^2$. As the dot product of the 4-velocity is a scalar quantity, it follows that $u \cdot u = c^2$ in all frames.

Considering now the 4-momentum:

$$p^\mu = m u^\mu \quad (1.44)$$

$$p \cdot p = p_0^2 - \mathbf{p}^2 = m^2 c^2, \quad (1.45)$$

in all frames, where m is the rest mass. The physical interpretation for p_0 is that it is the total energy of the particle,

$$c p_0 = c(m^2 c^2 + \mathbf{p}^2)^{\frac{1}{2}}, \quad (1.46)$$

for a particle travelling at much less than the relativistic speeds, $\frac{p}{m} \ll c$,

$$= mc^2 + \frac{\mathbf{p}^2}{2m} + \dots \quad (1.47)$$

$$p^\mu = \left(\frac{E}{c}, \mathbf{v} \right). \quad (1.48)$$

At this point, before I foray into scalar field theory, I shall switch to *natural units*. Setting $c = \hbar = \mu_0 = \epsilon_0 = 1$, Appendix D. I shall use natural units for the rest of the thesis.

The Schrödinger equation (1.33) is not Lorentz invariant (it has a single derivative with respect to time on one side and a second order derivative with respect to time on the other). Therefore to find an equation applicable to relativistic quantum mechanics, it is appropriate to begin with the covariant formalism introduced above. From equation (1.48),

$$E^2 = \mathbf{p}^2 + m^2. \quad (1.49)$$

$$\hat{E} \rightarrow i \frac{\partial}{\partial t} \quad \hat{\mathbf{p}} \rightarrow -i \nabla \quad (1.50)$$

Thus, with the operators acting on the wave function $\phi(\mathbf{x}, t)$,

$$-\frac{\partial^2 \phi}{\partial t^2} = -\nabla^2 \phi + m^2 \phi \quad (1.51)$$

$$\left[\frac{\partial^2}{\partial t^2} - \nabla^2 + m^2 \right] \phi(\mathbf{x}, t) = 0. \quad (1.52)$$

This is the Klein-Gordon equation, and is also represented by

$$[\square + m^2] \phi = 0. \quad (1.53)$$

The aptly named *box* or *wave operator* is

$$\begin{aligned} \square &= \frac{\partial^2}{\partial t^2} - \nabla^2 \\ &= g^{\mu\nu} \partial_\mu \partial_\nu \\ &= \partial^\mu \partial_\mu = \partial_\mu \partial^\mu. \end{aligned} \quad (1.54)$$

If we choose $\phi(x)$ to be a scalar then equation (1.53) is manifestly relativistically invariant.

The classical equation behaviour of a system is the lowest energy limit of infinite possible quantum paths, also known as the minimal-action. This is similar to a light beam taking the lowest energy route through any medium.

It might be asked, how does a non-sentient photon know to travel this lowest energy pathway? The answer is, light is emitted, not in a straight line, but in waves. Destructive interference acts far from the extremised path, while constructive interference acts in the small wavepacket around the extremised path.

Quantum fields are also not sentient beings, but statistical distributions of probability. The classical (minimal action) behaviour is also the result of summing over phases. A quantum field represents a system of particles in bulk. The equation of motion is similar to that of a simple harmonic oscillator. A particle, in this formalism, is analogous to a mode of oscillation.

The action has this form

$$S = \int d^4x \mathcal{L}, \quad (1.55)$$

where $\mathcal{L}(\phi, \partial_\mu\phi, x^\mu)$ is the Lagrangian density, which displays the invariance of the theory. $\delta S = 0$ gives the Euler–Lagrange equations

$$\partial_\mu \left(\frac{\partial \mathcal{L}}{\partial(\partial_\mu\phi)} \right) - \frac{\partial \mathcal{L}}{\partial\phi} = 0. \quad (1.56)$$

The Lagrangian density of a free scalar field has the form,

$$\mathcal{L} = \frac{1}{2} \partial_\mu\phi \partial^\mu\phi - \frac{1}{2} m^2\phi^2. \quad (1.57)$$

Therefore the minimal–action equation of motion for the scalar field is

$$\partial_\mu\phi \partial^\mu\phi + m^2\phi = 0. \quad (1.58)$$

We have recovered the Klein–Gordon equation. Further, for a spatially homogeneous scalar field, the spatial gradient terms are all zero,

$$\ddot{\phi} + m^2\phi = 0. \quad (1.59)$$

Now, defining another quantity, the scalar field momentum, Π ,

$$\Pi = \frac{\partial \mathcal{L}}{\partial \dot{\phi}} = \dot{\phi}. \quad (1.60)$$

The Hamiltonian of the system can be deduced from ϕ, Π and the Lagrangian density,

$$\begin{aligned} H &= \int d^3x \left(\Pi \dot{\phi} - \mathcal{L} \right) \\ &= \int d^3x \left(\dot{\phi}^2 - \frac{1}{2} \dot{\phi}^2 + \frac{1}{2} m^2 \phi^2 \right) \\ &= \frac{1}{2} \int d^3x \left(\dot{\phi}^2 + m^2 \phi^2 \right). \end{aligned} \quad (1.61)$$

All of the working above has been assuming a free, non-interacting particle, i.e. where there is no potential contributing to the energy. If I generalize the form of the Klein-Gordon equation to include any potential, it becomes

$$[\square + V(\phi)]\phi = 0. \quad (1.62)$$

If I generalize the formalism still further, to no longer confine the equations of motion to laboratory scales, but to include the scale factor of the Universe, I must use the metric

$$g_{\mu\nu} = \begin{pmatrix} 1 & 0 \\ 0 & -a^2(t)\delta_{ij} \end{pmatrix}. \quad (1.63)$$

This is for flat FRW spacetime.

The Lagrangian density of a scalar field is now

$$\begin{aligned} \mathcal{L}_\phi &= \frac{1}{2} \partial_\mu \phi \partial^\mu \phi - V(\phi) \\ &= \frac{1}{2} \dot{\phi}^2 - \left\{ \frac{1}{2a^2} (\nabla \phi)^2 \right\} - V(\phi). \end{aligned} \quad (1.64)$$

Neglecting any interactions ϕ has with other fluids and assuming spatial homogeneity, the stress energy of ϕ takes the form of a perfect fluid:

$$T_\phi^{\mu\nu} = (\rho_\phi + p_\phi) u^\mu u^\nu - p_\phi g^{\mu\nu}, \quad (1.65)$$

where p_ϕ is the scalar field energy pressure, and ρ_ϕ is the energy density of the field.

Noether's theorem gives (Peacock, 1996)

$$\frac{d}{dx^\mu} \left[\frac{\partial \mathcal{L}}{\partial(\partial_\mu \phi)} \frac{\partial \phi}{\partial x^\nu} - \mathcal{L} g^{\mu\nu} \right] = 0, \quad (1.66)$$

therefore

$$\frac{d}{dx^\mu} [\partial^\mu \phi \partial^\nu \phi - \mathcal{L} g^{\mu\nu}] = 0. \quad (1.67)$$

The quantity in square brackets is the energy momentum of the field,

$$T_\phi^{\mu\nu} = \partial^\mu \phi \partial^\nu \phi - \mathcal{L} g^{\mu\nu}. \quad (1.68)$$

ρ_ϕ is the effective energy density of the field ϕ and p_ϕ is the effective pressure. The energy density is also, of course, represented by the Hamiltonian of the field, equation (1.61),

$$\begin{aligned} \rho_\phi &= \dot{\phi}^2 - \mathcal{L} \\ &= \frac{1}{2} \dot{\phi}^2 + \left\{ \frac{1}{2a^2} (\nabla \phi)^2 \right\} + V(\phi). \end{aligned} \quad (1.69)$$

Equating equation(1.65) $\times g_{\mu\nu}$ to equation (1.68) $\times g_{\mu\nu}$ gives

$$p_\phi = \frac{1}{2} \dot{\phi}^2 - \left\{ \frac{1}{6a^2} (\nabla \phi)^2 \right\} - V(\phi). \quad (1.70)$$

If the scalar field is spatially homogeneous, which is our assumption, fitting in as a stage inside the normal development of an FRW cosmology, then the terms in curly brackets are all zero. The switch from a Minkowski metric to a FRW metric also has an effect on the action for the scalar field. The integral over coordinates is multiplied by what is commonly know as the *spacetime volume element*. This is $\sqrt{-\det[g_{\mu\nu}]}$, a Jacobian indicating the change of coordinate system. For a Minkowski metric the spacetime volume element is equal to one. For the metric of equation (1.63),

$$\det g_{\mu\nu} = \begin{vmatrix} 1 & 0 \\ 0 & -a^2(t)\delta_{ij} \end{vmatrix} = -a^6. \quad (1.71)$$

Extremising this new action

$$S_\phi = \int d^4x a^3 \mathcal{L} \quad (1.72)$$

gives a classical equation of motion (Appendix E)

$$\ddot{\phi} + 3H\dot{\phi} + V'(\phi) = 0, \quad (1.73)$$

which is just the classical equation of motion for an object rolling down a slope with friction $3H$. This is the starting point of the *new inflation* model proposed by Linde (1982) and Albrecht & Steinhardt (1982) shortly after the first hypothesis of inflation (Guth, 1981). At some point in the radiation dominated era of the early Universe there is a phase transition – similar to a ferromagnet being cooled below its critical temperature. For the magnet, at the instant of passing through T_c different symmetry directions for the magnetic moment are chosen in different regions. These *domains* then expand. The analogous *symmetry breaking* for the Linde and Albrecht & Steinhardt papers is $SU(3) \times SU(2) \times U(1)$, the gauge group combining weak, electromagnetic and strong interactions, symmetry breaking of Coleman–Weinberg $SU(5)$ theory, the so-called grand unified gauge group which has 24 vector bosons. The symmetry breaks due to the appearance of the classical field:

$$\phi = \sqrt{\frac{2}{15}} \phi_0 (1, 1, 1, -\frac{3}{2}, -\frac{3}{2}). \quad (1.74)$$

The transition of the order parameter ϕ , the expectation value of the scalar field, from $\phi = 0$ to a symmetry breaking minimum ϕ_0 proceeds via the creation and expansion of bubbles containing non-vanishing scalar fields.

First order phase transitions occur when $T \simeq T_c$ when the order parameter appears and disappears rapidly.

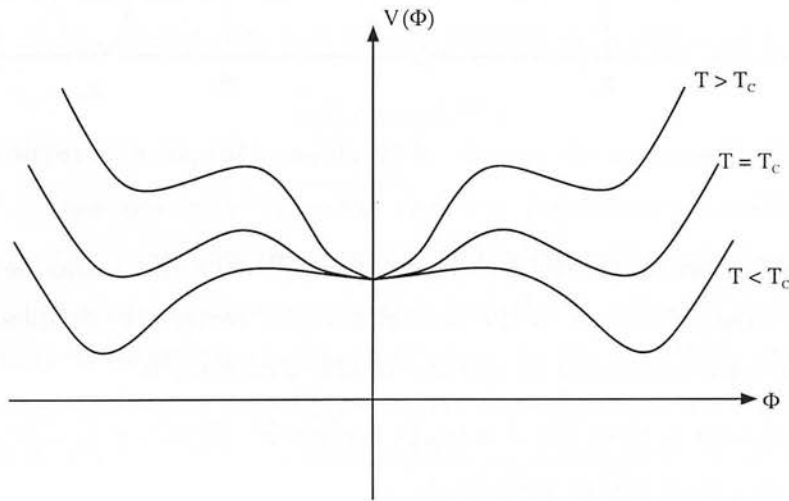


Figure 1.3: A sketch illustrating the changing potential during a first order phase transition.

When $T \gg T_c$ the potential has absolute minimum at $\phi = 0$. As T gets close to T_c two new minima develop at $\phi = \pm\phi_0$, with the three minima of the potential degenerate (Figure 1.2).

It is assumed that at $T \ll T_c$ a first order phase transition chooses the minimum at $\phi = \phi_0$, and that $V(\phi, T = 0) = 0$.

The shape of the resulting potential is essential to the model. The potential of these basic *new inflation* models consisted of a long, virtually flat slope between the origin of ϕ and the symmetry broken minima, in this stage of a FRW universe where all of the energy has been converted to this scalar potential.

At a temperature below T_c the boundary between $V_0(\phi = 0)$ and $V_0(\phi_0)$ may be traversed by quantum or thermal tunneling with the nucleation of bubbles, where $V_0(\phi)$ is the effective, $T = 0$, scalar potential (Kolb & Turner, 1990).

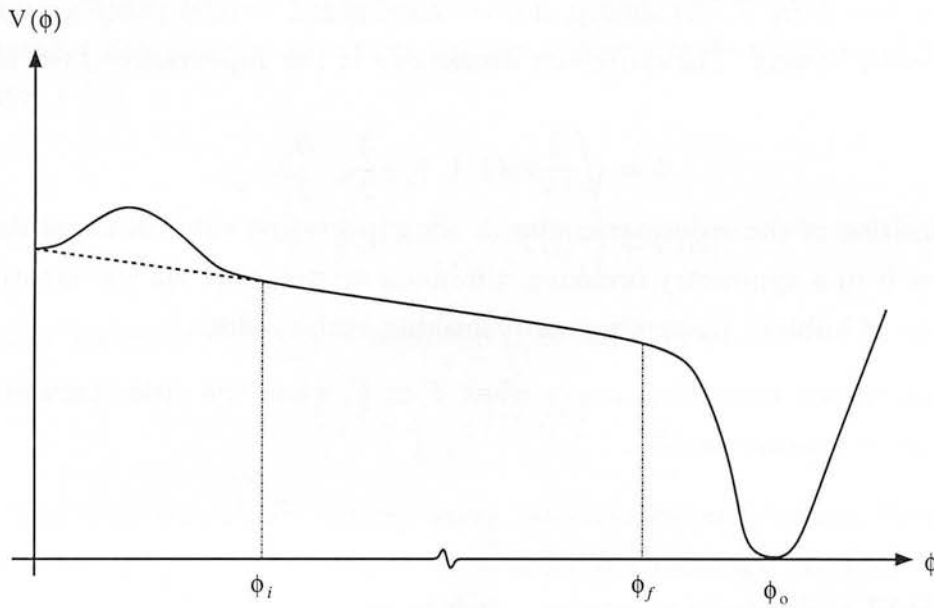


Figure 1.4: An illustration, not to scale, of the shape of the potential required for slow roll inflation.

After bubble formation there is a rollover period while the scalar field inside the bubble ‘rolls’ down the slope of the potential and if certain conditions are satisfied this period is long compared to the age of the Universe, H^{-1} .

The first condition is that the $\ddot{\phi}$ term is negligible. Between ϕ_i and ϕ_f (the field at the beginning and end of inflation),

$$|\ddot{\phi}| \ll |3H\dot{\phi}|, \quad (1.75)$$

and the slope is sufficiently flat, so that the term analogous to kinetic energy is much less than the potential energy term:

$$\frac{\dot{\phi}^2}{2} \ll V(\phi). \quad (1.76)$$

In this case the equation of motion (1.73) takes the form:

$$-3H\dot{\phi} \simeq V'(\phi). \quad (1.77)$$

These two conditions are more often represented in the literature (Liddle & Lyth (1993), Kolb & Turner (1990)) as

$$\left| \frac{V''}{V} \right| \ll \frac{24\pi}{m_{\text{pl}}^2} \quad \text{and} \quad \left| \frac{V'}{V} m_{\text{pl}} \right| \ll (48\pi)^{\frac{1}{2}}. \quad (1.78)$$

The steps in between are straightforward, following from the constraints, the slow-roll equation, and the fact that during inflation H remains close to constant, but I include working in Appendix E for completeness. Recalling the form of the density and pressure in equations (1.69) and (1.70), the relation (1.76) implies

$$\rho_{\phi} \simeq V(\phi) \quad (1.79)$$

$$p_{\phi} \simeq -V(\phi), \quad (1.80)$$

therefore

$$\rho_{\phi} = -p_{\phi}. \quad (1.81)$$

This equation of state is familiar, from the cosmological constant problem (Section 1.1.4), equation (1.26), showing that the scalar potential, or vacuum energy, during the rollover period $\simeq V(\phi = 0)$ behaves as a cosmological constant. When this vacuum energy dominates, our bubble evolves as in equation (1.29),

$$a(t) \propto \exp(Ht). \quad (1.82)$$

As ϕ nears ϕ_0 the potential steepens and the inflationary conditions are not satisfied, and $a(t)$ ceases to increase exponentially. Here the damping term related to the expansion of the Universe is smaller, and the equation of motion takes the form of a damped harmonic oscillator (Dolgov & Linde (1982), Albrecht *et al.* (1982)). ϕ overshoots ϕ_0 and oscillates about the minimum, with frequency $\omega^2 - V''(\phi_0)$ (Kolb & Turner, 1990). These oscillations correspond to zero-momentum ϕ particles. The damping of these oscillations corresponds to the decay of these ϕ particles to other particle species which couple to ϕ .

Due to this another term appears in the equation of motion: $\Gamma_{\phi}\dot{\phi}$, where Γ_{ϕ} is the decay width of the scalar particles. The complete equation of motion is

$$\ddot{\phi} + 3H\dot{\phi} + \Gamma_{\phi}\dot{\phi} + V'(\phi) = 0. \quad (1.83)$$

Light, relativistic particle species which couple to ϕ are radiated during the rapid oscillations over a small number of periods. $\phi(t)$ convergently oscillates about ϕ_0 according approximately to (Dolgov & Linde, 1982),

$$\phi(t) \simeq \phi_0[1 - \exp(\gamma t) \cos M_\phi t]. \quad (1.84)$$

Here M_ϕ is the mass of the Higgs boson as ϕ tends to ϕ_0 and $\frac{3}{2}H$ is the contribution to γ , the damping from the $3H\dot{\phi}$ friction term but for the case of rapid oscillations the main contribution to γ arises from particle production. Thermalizing interactions among these particles such as 2-body scatterings and decays populate the other particle species. The larger part of the vacuum energy in the ϕ field must be converted to radiation this quickly as the radiation is red-shifted away as soon as it is converted. The process of the decay products thermalizing is called *reheating*.

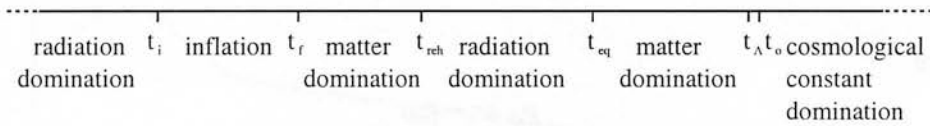


Figure 1.5: Illustration of the timeline with inflation; the subscript ‘reh’ denotes the reheating era.

The next question is, what observable consequences would this period of exponential expansion have? Between ϕ_i and ϕ_f there are N e-folds of growth in the scale factor,

$$N(\phi_i \rightarrow \phi_f) = \ln \left(\frac{a(t_f)}{a(t_i)} \right). \quad (1.85)$$

From the slow-roll equation of motion (1.77),

$$H \simeq -\frac{8\pi}{m_{\text{pl}}^2} \frac{V(\phi)}{V'(\phi)} \frac{d\phi}{dt}, \quad (1.86)$$

therefore

$$N(\phi_i \rightarrow \phi_f) = \int_{t_i}^{t_f} H dt = -\frac{8\pi}{m_{\text{pl}}^2} \int_{\phi_i}^{\phi_f} \frac{V(\phi)}{V'(\phi)} d\phi. \quad (1.87)$$

The size of the part of the Universe which can be observed now is roughly the Hubble volume H_0^{-3} . For all of the observable Universe to be inflated to outside the horizon, the exponential expansion period would need to have lasted approximately 60 Hubble times, $\Delta t > 60H^{-1}$ (Appendix F).

I now turn to the properties of the Fourier components of the field. The Fourier components of the scalar field, $\phi(\mathbf{k})$, do not have definite values. The real and imaginary parts of $\phi(\mathbf{k})$ have a probability distribution which is the modulus of the wavefunction of a simple harmonic oscillator and, except for reality conditions, the phases of $\phi(\mathbf{k})$ are random. These quantum fluctuations are not measurable.

During inflation the quantum fluctuations of the scalar field exit the horizon and become a classical, measurable quantity (Kiefer, 2000). As each fluctuation mode, $\phi(\mathbf{k})$, crosses the horizon, it has the same physical size, $\sim H^{-1}$. The scalar field is assumed to be in its vacuum state, thus the phase of each mode is random and independent from the others. The *central limit theorem* states that the distribution of a sum of independent, random variables, with distributions which need not be Gaussian, tends to a Gaussian as the number of variables tends to infinity (see e.g. Kendall & Stuart, 1969). The scalar field fluctuation, when written as a Fourier transform, is effectively a sum over an infinite number of functions of random variables. Thus the assumption that the inflaton field is in the vacuum state implies that the fluctuations resulting from inflation are Gaussian. Inflation thus generates a Gaussian perturbation, its solution to the problem of seeding the large-scale structure.

But inflation itself has problems. The reheating mechanism of new inflation does not take into account the quantum dynamics of the fields when the oscillations have a large amplitude, or *broad parametric resonance*. This typically leads to the inflaton particle decaying explosively into other massive bosons, which decay into other particles. This significantly changes, and complicates, many features of reheating, particularly the value of the temperature of the Universe after reheating, and leads to problems such as the overproduction of relic particles from the high temperature phase of the Universe (Kofman *et al.*, 1994; Lyth, 2000).

There are other early Universe models which to varying degrees offer solutions for the holes in the HBB model. For example, cosmic defect models tackle solely the problem of small-scale structure formation (Section 1.1.5), possibly in conjunction with inflation. There are also a variety of early Universe models originating from higher-dimensional supersymmetric theories. However, their observational consequences have not been calculated to the same extent as the predictions of the observations for inflation.

An alternative early Universe model, which I shall be looking at in detail in

Chapter 4, is warm inflation (Berera, 1995, 1996). Warm inflation is motivated by the idea of an artificiality in the separation of inflation into two stages; a stage where all of the energy in the Universe is held in a scalar field vacuum potential, and a following stage where, after a rapid conversion, the Universe is filled with only radiation; this being hypothesised less likely than the scenario of radiation being present during inflation and interacting with the scalar field. An important prediction of this warm inflation theory is a smooth transition from inflation to radiation domination, without any of the problems associated with the reheating process of standard inflation.

1.3 The Cosmic Microwave Background Anisotropies

Before the epoch of what is variously called *decoupling*, *recombination* and *last scattering*, which occurs during the matter dominated era in the life of the Universe, baryonic matter was tightly coupled to photons through Thomson scattering of photons by free electrons. After this time most protons and electrons came together into uncharged atoms which hardly interact with photons, although there is some small residual ionisation. The radiation was no longer bound by the continuing scattering with charged matter and streamed freely through the Universe straight to us, unless possibly reionisation due to very early structure re-scattered the photons.

Discounting any reionisation, this cosmic microwave background radiation preserves its close to black body spectrum from the epoch of decoupling (see e.g. Peebles, 1993).

The CMB temperature has been measured to be (see e.g. Partridge, 1995),

$$2.735 \pm 0.015 K. \quad (1.88)$$

The fluctuations in the temperature field of the CMB radiation are a fossil record of the primordial fluctuations, present at a time when the Universe was an almost uniform mixture of this coupled photon-baryon fluid and a dark matter component, before the complicating effects of non-linear gravitational evolution. Theories of structure formation must entail a complete prescription for the form of the initial conditions.

The Planck Surveyor satellite, planned for launch in 2007, will have noise per pixel of about $2 \times 10^{-6} K$, and an angular resolution which varies between 5 and

30 arcminutes, dependent on frequency. Compare this to the last all-sky CMB anisotropy experiment from which we have data, the Cosmic Background Explorer (COBE) Differential Microwave Radiometer (DMR) satellite instrument, launched in 1988, which had an angular resolution of 7° and a signal-to-noise per pixel of approximately one.

The upcoming MAP and Planck satellite experiments will produce CMB observations of unprecedented accuracy and completeness. My research has entailed developing tests of Early Universe theories for the new high quality data.

1.3.1 Properties of Gaussian Fluctuations

Inflation predicts a spectrum of density perturbations in the matter distribution of the primordial Universe, to be reflected in the CMB, which forms an almost perfect Gaussian random field.

When looking at a Gaussian spectrum of initial density fluctuations, its statistical properties are completely specified by its power spectrum, or, equivalently, by the autocorrelation function. Another useful statistical quantity of the density field, to distinguish between Gaussian and non-Gaussian fields, is its bispectrum.

Defining the density contrast for use in all the calculations

$$\delta(\mathbf{x}) \equiv \frac{\delta\rho(\mathbf{x})}{\bar{\rho}} = \frac{\rho(\mathbf{x}) - \bar{\rho}}{\bar{\rho}}, \quad (1.89)$$

where $\rho(\mathbf{x})$ is the energy density, and $\bar{\rho}$ is the mean energy density.

Expressing the density contrast in a Fourier expansion of wavenumber \mathbf{k} ,

$$\delta(\mathbf{x}) = \frac{1}{(2\pi)^3} \int \exp(-i\mathbf{k} \cdot \mathbf{x}) \delta(\mathbf{k}) d^3k \quad (1.90)$$

and

$$\delta(\mathbf{k}) = \int \exp(i\mathbf{k} \cdot \mathbf{x}) \delta(\mathbf{x}) d^3x. \quad (1.91)$$

The density contrast $\delta(\mathbf{x})$ is a real quantity, thus from equation (1.90), $\delta(\mathbf{k}) = [\delta(-\mathbf{k})]^*$.

Throughout the following calculations I assume that the Gaussian density fields are homogeneous and isotropic.

Autocorrelation Function

The autocorrelation function of the density field is defined to be

$$\xi(\mathbf{r}) = \langle \delta(\mathbf{x} + \mathbf{r})\delta(\mathbf{x}) \rangle_{\text{all skies}}, \quad (1.92)$$

where the angle brackets represent an *ensemble* average, an average taken over all possible Universes.

Another property of Gaussian random density fields is that in their context the *Ergodic Theorem* applies. If $P(k)$ is continuous then averages taken over a large spatial volume, L^3 , are equivalent to averages over all skies (Adler, 1981). This results from the assumption that the set of all possible Universes forms a Gaussian distribution. This cannot possibly be proven, but the Gaussian field is a more likely candidate to model nature than any other. The ergodic theorem swaps one Gaussian distribution, which we cannot measure, for another, which we have access to. So the average above can be calculated using ergodicity to be

$$\xi(\mathbf{r}) = \frac{1}{L^3(2\pi)^3} \int |\delta_k|^2 \exp(-i\mathbf{k} \cdot \mathbf{r}) d^3k. \quad (1.93)$$

This writes the notional average over infinity in equations (1.90) and (1.91) now as over physical length L , taken to be larger than any scale of cosmological interest.

Returning henceforth to the notional average over infinity.

Power Spectrum

For an isotropic and homogeneous density field the power spectrum is defined to be

$$\langle \delta(\mathbf{k}_1)\delta(\mathbf{k}_2) \rangle = (2\pi)^3 P(k) \delta_D^3(\mathbf{k}_1 + \mathbf{k}_2), \quad (1.94)$$

where the angle brackets again represent an ensemble average. δ_D^3 is the Dirac delta function. The relation above depends completely on the isotropy and homogeneity of the field. The isotropy of the field implies that the power spectrum is isotropic, and depends only on $k = |\mathbf{k}|$.

$$P(k) = \langle |\delta_k|^2 \rangle \quad (1.95)$$

The Dirac delta function, in the definition of the power spectrum, also arises from an assumption of isotropy and homogeneity. The power spectrum is the Fourier

transform of the autocorrelation function, from equation (1.93),

$$P(k) = (2\pi)^3 \int \xi(\mathbf{r}) \exp(i\mathbf{k} \cdot \mathbf{r}) d^3r. \quad (1.96)$$

This relation was shown in Section (1.3.1) above using ergodicity. If I derive this relation more explicitly, using the ensemble average, beginning from equation (1.92),

$$\begin{aligned} \xi(\mathbf{r}) &= \langle \delta(\mathbf{x} + \mathbf{r}) \delta(\mathbf{x}) \rangle \\ &= \frac{1}{(2\pi)^6} \int d^3k d^3k' \langle \delta(\mathbf{k}) \delta(\mathbf{k}') \rangle \exp(-i\mathbf{k} \cdot \mathbf{r}) \exp[-i(\mathbf{k} + \mathbf{k}') \cdot \mathbf{x}], \end{aligned}$$

and compare the left and right sides, it is clear that the right hand side cannot contain any explicit dependence on \mathbf{x} . Isotropy and homogeneity demands that the correlation between two points can only depend on the distance of one from other. Therefore the definition of the power spectrum, equation (1.94), must contain a Dirac delta function of the form $\delta_D^3(\mathbf{k}_1 + \mathbf{k}_2)$.

Bispectrum

On its own the power spectrum (or autocorrelation function) cannot distinguish between Gaussian and non-Gaussian fields.

Isotropy of a real field also implies the isotropy and homogeneity of its Fourier components (Adler, 1981). For an isotropic and homogeneous field we have the form of the power spectrum, equation (1.94),

$$\langle \delta(\mathbf{k}_1) \delta(\mathbf{k}_2) \rangle = (2\pi)^3 P(k) \delta_D^3(\mathbf{k}_1 + \mathbf{k}_2). \quad (1.97)$$

This definition incorporates the symmetries of the field. The power spectrum can depend only on $k = |\mathbf{k}_1|$ because of isotropy. There cannot be an inherent dependence on a particular wavevector \mathbf{k} . Once more, to preserve isotropy and homogeneity, the only part of the variables \mathbf{k}_1 and \mathbf{k}_2 that can survive on the right hand side is their relation to each other, so the delta function is a statement of translational invariance.

Similarly the Bispectrum is defined to be

$$\langle \delta(\mathbf{k}_1) \delta(\mathbf{k}_2) \delta(\mathbf{k}_3) \rangle = (2\pi)^3 B(\mathbf{k}_1, \mathbf{k}_2, \mathbf{k}_3) \delta_D^3(\mathbf{k}_1 + \mathbf{k}_2 + \mathbf{k}_3), \quad (1.98)$$

with exactly the same symmetry conditions holding, i.e. those arising from the homogeneity of the 3-point function in real space. For a Gaussian field $B(\mathbf{k}_1, \mathbf{k}_2, \mathbf{k}_3)$ is zero (Appendix G), but in general B is non-zero (Luo, 1994a).

1.3.2 The Angular Power Spectrum of the CMB

The temperature fluctuations in the cosmic microwave background are always expanded in terms of spherical functions, such as spherical harmonics or associated Legendre functions, as the CMB is distributed over the sphere of the sky. There is a dipole anisotropy due to our peculiar velocity with respect to the cosmic rest frame. Expanding the CMB temperature into separate components in the notation of Liddle and Lyth in *The Cold Dark Matter Density Perturbation*, 1993, as a function of angular direction in the sky,

$$\begin{aligned} T(\theta, \phi) &= T(\mathbf{e}) \\ &= \text{mean temperature} + \text{dipole component} + \text{other components} \quad (1.99) \\ &= \bar{T} + \mathbf{v} \cdot \mathbf{e} + \Delta T(\mathbf{e}), \end{aligned}$$

where \mathbf{v} is our peculiar velocity, our velocity without cosmic expansion, and \mathbf{e} is a unit direction vector.

The $\mathbf{v} \cdot \mathbf{e}$ term is the approximate form of the dipole component, neglecting the small quadrupole component from relativistic effects from our velocity,

$$\mathbf{e} = \begin{pmatrix} \sin \theta \cos \phi \\ \sin \theta \sin \phi \\ \cos \theta \end{pmatrix}. \quad (1.100)$$

Because anisotropies on different angular scales across the sky are caused by different effects, the $\Delta T(\theta, \phi)$ term can be expanded in spherical harmonics, Y_{lm} , which form a complete set of orthogonal functions on the surface of the unit sphere.

$$\frac{\Delta T(\mathbf{e})}{T} = \sum_{l=2}^{\infty} \sum_{m=-l}^{m=+l} a_{lm} Y_{lm}(\mathbf{e}), \quad (1.101)$$

where

$$\int d\Omega [Y_{lm}]^* Y_{l'm'} = \delta_{ll'}^K \delta_{mm'}^K, \quad (1.102)$$

and δ^K is the Kronecker Delta.

The sum in l excludes the monopole fluctuation, which cannot be measured, and the dipole component, which is dominated by the Earth's motion with respect to the expansion of the Universe. The a_{lm} s are our stochastic variables. They are coefficients of the spherical harmonic expansion of a field distributed on a sphere. According to the present best estimates from CMB experiments, the CMB anisotropies form a Gaussian field with zero mean. Therefore, given that any linear combination of Gaussian fields is also Gaussian, the resulting a_{lm} s are expected to be Gaussian with zero mean,

$$\langle a_{lm} \rangle = 0. \quad (1.103)$$

CMB experiments and theories most often produce plots of the angular power spectrum C_l against multipole coefficients l ,

$$\langle a_{lm} a_{l'm'}^* \rangle = \delta_{ll'}^K \delta_{mm'}^K C_l. \quad (1.104)$$

This is the starting point for most CMB analysis for the purposes of testing early Universe models. The angular power spectrum bins the fluctuations on the sky into a representation of power on different angular scales. Particular physical effects in the Universe leave a signature on particular scales.

Early Universe theories yield a three-dimensional distribution of primordial gravitational perturbations. $\Phi(\mathbf{k})$ labels a Fourier mode of perturbation, so that we can more easily distinguish between gravitational oscillations on different scales. The gravitational perturbation leads to the field of fluctuations on the CMB sky via (Wang & Kamionkowski, 2000)

$$a_{lm} = (4\pi)(-i)^l \int d^3k \Phi(\mathbf{k}) \Delta_l(\mathbf{k}) Y_{lm}(\mathbf{e}), \quad (1.105)$$

where $\Delta_l(\mathbf{k})$ is the photon transfer function which relates the photon temperature to the gravitational field, encompassing a variety of physical processes. I shall review some of the various physical effects which determine the usually complicated form of the transfer function in the next section.

1.3.3 The Imprint of Cosmological Parameters on the CMB Power Spectrum

As the temperature of the Universe decreased with time, it passed through the epoch of matter–radiation equality. During the initial phase of matter domination, when the temperature of the radiation in the Universe is above the ionization

temperature of hydrogen, the electrons present in the matter, which are electromagnetically coupled to the baryons, continue to Thomson–Compton scatter off the photons.

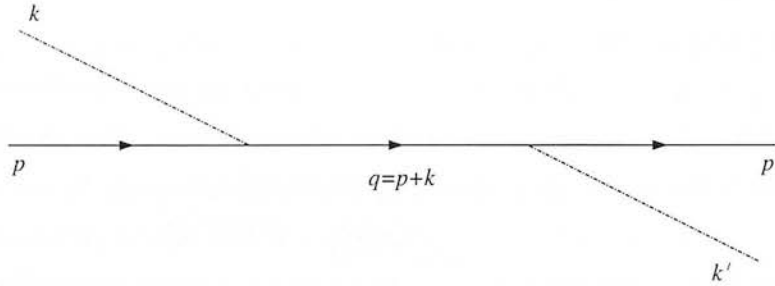


Figure 1.6: An electron with momentum p Compton scatters off a photon with momentum k .

This *photon pressure* opposes the gravitational attraction on the baryons of the primordial overdensities which are present in the dark matter distribution which interacts only gravitationally. For most models of inflation the spectrum of these perturbations has the form

$$\delta \propto k^n, \quad (1.106)$$

where n is mostly close to 1.

When the temperature of the Universe drops below the ionization temperature of hydrogen, a proportion of the electrons and protons come together to form hydrogen. For historical reasons this process is called *recombination*. As the temperature continues to drop, the proportion of uncombined baryons to neutral atoms falls, as it would in the laboratory. When the baryonic matter forms neutral atoms, the photons no longer interact with it, and they stream through the Universe in a straight line (neglecting possible cosmological reionisation, and a small proportion of charged matter present in the large scale structure of the Universe) to us. Therefore the point at which the CMB photons were released at recombination, approximately 300 000 years after what in the FRW Universe would be the initial singularity, is termed *the last scattering surface*.

The difference in time between the first combination of some neutrons and protons into atoms and the matter having all combined is referred to in the literature as *the thickness of the last scattering surface*. The temperature at which last scattering occurs, in natural units, is 0.3eV. The binding energy of hydrogen, B , is

$$B = m_p + m_e - m_H = 13\text{eV}, \quad (1.107)$$

where m_p , m_e and m_H are the masses of the proton, the electron and of the hydrogen atom respectively. After recombination, the mean free path of the photons is greater than the Hubble radius, but before recombination the Universe is in thermal equilibrium, and the process



where p , e , H and γ represent a proton, an electron, a hydrogen atom and a photon, is governed by equilibrium thermodynamics. The temperature distribution of the radiation before recombination is represented by the Planck blackbody function, as plotted in Figure 1.7.

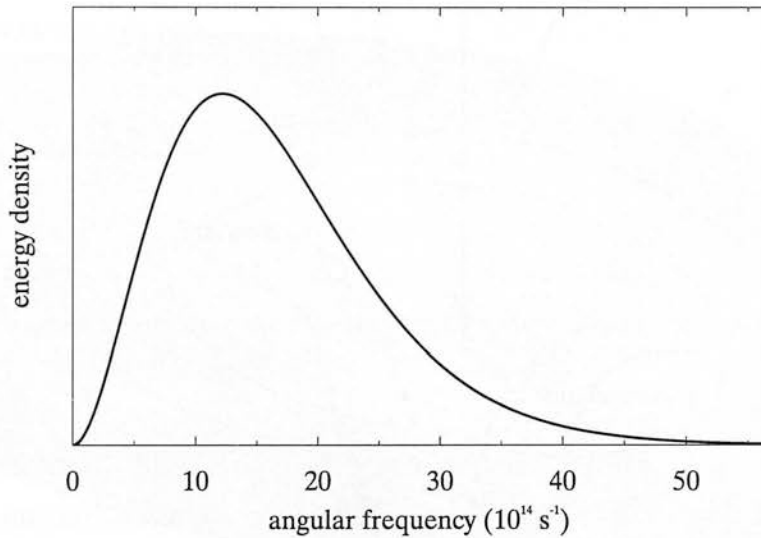


Figure 1.7: The shape of the Planck radiation curve, of energy density against frequency, for a blackbody of temperature of 3300K .

There are still enough high energy photons present until last scattering to keep a large proportion of the matter ionised. Recombination is generally set at the point when 90% of the electrons have combined with protons.

If X_{eq} is the equilibrium ionisation fraction, the proportion of the protons which are ionised while the Universe is in thermal equilibrium, then its temperature evolution is governed by the Saha equation (see e.g. Kolb & Turner, 1990)

$$\frac{1 - X_{\text{eq}}}{(X_{\text{eq}})^2} = \frac{4\sqrt{2}\zeta(3)}{\sqrt{\pi}} \eta \left(\frac{T}{m_e}\right)^{\frac{3}{2}} \exp\left(\frac{B}{T}\right). \quad (1.109)$$

$\zeta(3)$ is the Riemann zeta function of 3, and η is the baryon-to-photon ratio. It is η and $(T/m_e)^{3/2}$ being small numbers that requires the temperature, T , to drop to 0.3eV before 90% of the electrons have combined. The thermal nature of the radiation is preserved after it is released at recombination, Appendix H.

Before recombination the expanding and cooling Universe contains a dark matter component with a distribution of over and under-densities. Consider an overdensity in the dark matter distribution. It can be considered as a potential well with the lip at the point where the density is the average dark matter density. When the edges of the potential well pass through the sound horizon, a (comoving) standing wave oscillation in the photon-baryon fluid begins, the lips of the well being the nodes. The phase of an oscillation effects its imprint on the power

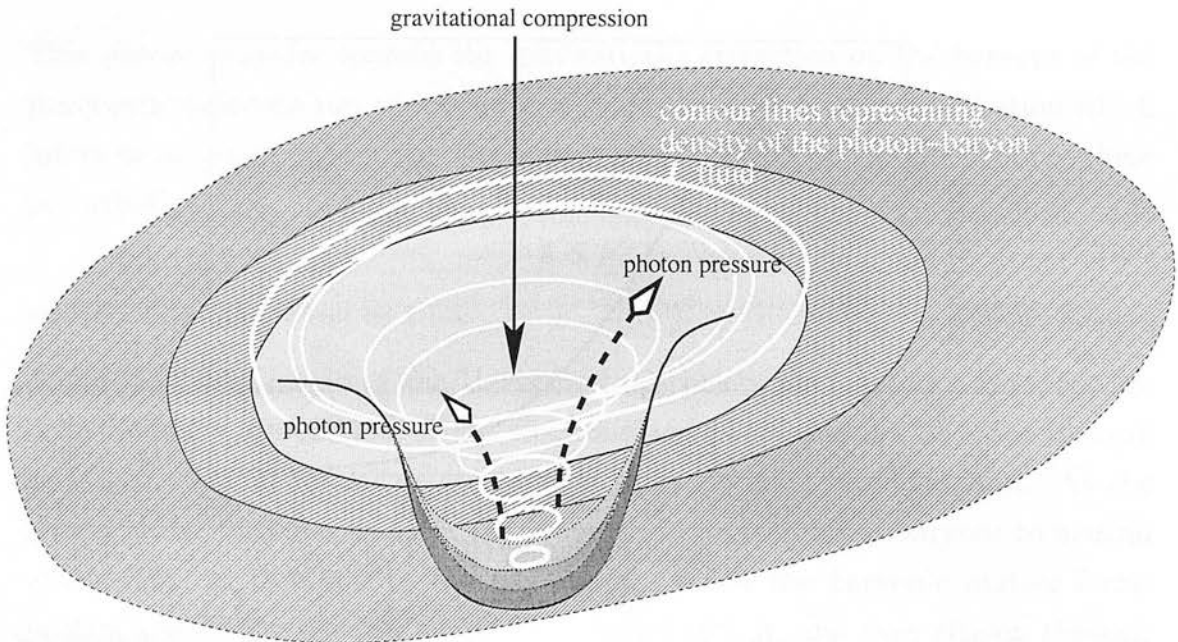


Figure 1.8: The photon pressure from Thompson-Compton scattering in the coupled photon-baryon fluid resists gravitational compression. As the baryonic matter first drops into the well, at sound horizon exit, the fluid begins to compress and photon pressure affects the potential, causing it to begin to decay. However the highly compressed fluid re-expands, reaches a maximum and then recollapses, the initial compression driving the oscillations.

spectrum of the CMB, leading to *acoustic peaks* in the power spectrum (Hu & Sugiyama, 1996).

The oscillation can be modelled as a simple harmonic oscillator with effective dimensionless mass $m_{\text{eff}} = 1 + R$ where

$$R = \frac{\rho_b + p_b}{\rho_r + p_r}. \quad (1.110)$$

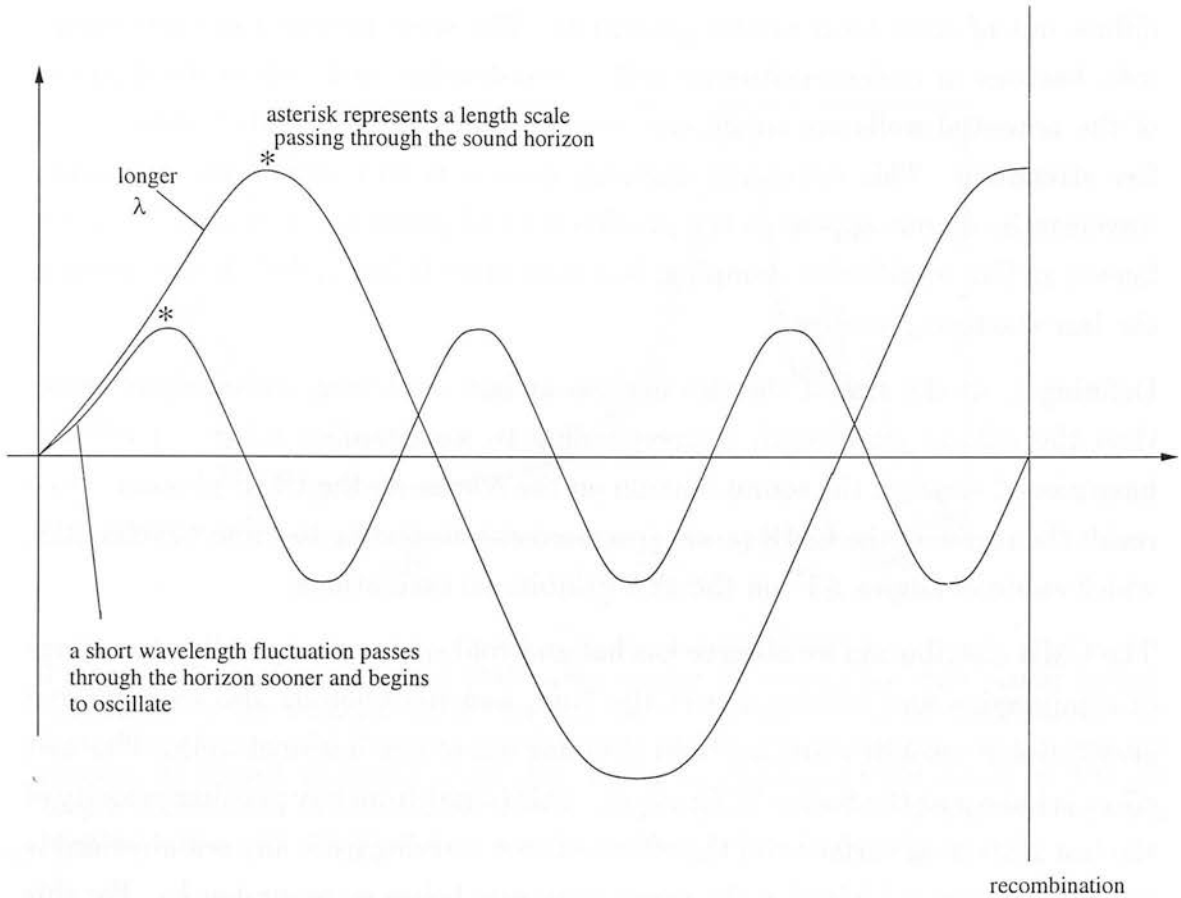


Figure 1.9: Diagram illustrating the way the size of a fluctuation imprints on the microwave background.

The above relation is the baryon-momentum density ratio. The baryon density has an effect on the oscillation of the fluid and therefore the heights of the acoustic peaks.

The cosmic microwave background is received by us as a distribution over the sky. The appearance of the fluctuations will be affected by the path the photons have taken to us, which depends on the geometry of the Universe, and of course the imprint of various oscillations at recombination depends on the rate of expansion of the Universe.

Toward the smallest wavelength end of the power spectrum the peaks are damped by the effect of the finite time it takes for the hydrogen atoms to form. Until all the matter becomes neutral, the presence of ionized matter causes photons to have a short enough mean free path that the effect of oscillations from the smaller sized potential wells is averaged out. During decoupling, in the time between the strong photon-baryon coupling and photon free-streaming, the photons begin to

diffuse out of their local matter potentials. The same photon can then impact with baryons in underdensities as well as overdensities and, where the diameter of the potential wells are small, can move in and out of several of them before free streaming. This collisional damping process is why oscillations at smaller wavelengths do not appear in the predicted CMB power spectrum, and it is also known as Silk or diffusion damping, but sometimes is just called the thickness of the last scattering surface.

Defining s_* as the size of the size horizon at last scattering, wavelengths longer than the critical wavelength (corresponding to wavenumber $k_A = \frac{\pi}{s_*}$) will not have passed through the sound horizon on the release of the CMB photons. As a result the region of the CMB power spectrum corresponding to these wavelengths, which subtend angles $\lesssim 1^\circ$ on the sky, exhibits no oscillations.

The CMB distribution we observe has hot and cold spots corresponding to regions of compression and rarefaction of the fluid, and the photons also experience a gravitational redshift resulting from climbing out of gravitational wells. This last effect is known as the Sachs–Wolfe effect. This (apart from any peculiar velocity of the last scattering surface and the effects of re-scattering from any reionisation) is the only physics exhibited in the power spectrum below wavenumber k_A . For this region of the power spectrum, for the particular case of a spatially flat Universe and an adiabatic spectrum of perturbations, the transfer function of equation (1.105) has the simple form (Wang & Kamionkowski, 2000):

$$\Delta_l^{\text{Sachs–Wolfe}} = \frac{1}{3} j_l(kr^*), \quad (1.111)$$

where j_l is a spherical Bessel function, and r^* is the distance the photon has travelled from the last scattering surface.

The *integrated Sachs–Wolfe effect* is the effect of the combined gravitational redshifts the photon experiences along the line-of-sight from recombination.

Predictions of the CMB power spectrum (Seljak & Zaldarriaga (1996), Turner (1998)) are calculated for parameter estimation given values for the Hubble constant, the cosmological constant contribution to the density of the Universe, the curvature of the Universe and the baryon content and cold dark matter density. There are further contributions from up to seven other *cosmological parameters*, such as that of *hot* dark matter content, such as massive neutrinos which damp out density fluctuations due to their thermal motion, which can alter the power spectrum, Figure 1.10.

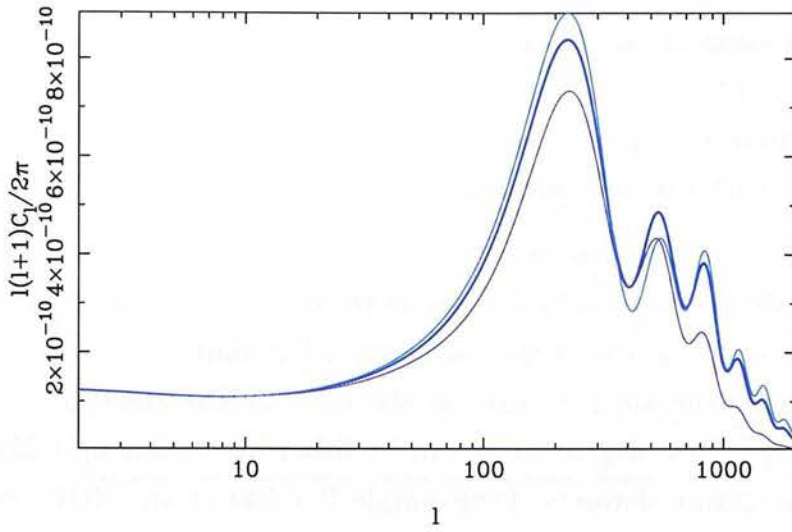


Figure 1.10: Plot of simulated CMB power spectra for varying hot dark matter content. The the power spectrum plotted in blue contains a 2% proportion of hot dark matter, cold dark matter density of 0.25 and baryon fraction 0.03. The power spectrum plotted in purple contains the highest proportion of hot dark matter, an unchanged CDM density of 0.25 and baryon fraction 0.01. The turquoise line was generated with no hot dark matter content and baryon fraction 0.05. All of the three simulations have a total density of 1.

The fluctuations on large angular scales do not display acoustic peaks as, at recombination, fluctuations on these scales have not entered the sound horizon. The shape of the power spectrum in this region reflects the spectral index of the underlying cosmological model, Figure 1.11.

The power spectrum on smaller angular scales features acoustic oscillations which, through the mechanism just described, are sensitive to the geometry, size and constituents of the Universe.

Increasing the baryon density, $\Omega_b h^2$ at last scattering increases the inertia so reducing the sound speed of the photon-baryon fluid, so the acoustic peaks move. Plus this increase in baryons increases the pressure on infall into the cold dark matter potentials, therefore increasing the amplitude of the acoustic oscillations. Increasing the total matter density, $\Omega_0 h^2$, would move matter-radiation equality to an earlier time. Increasing cold dark matter density would, with total density fixed, decrease the baryon fraction, so having the opposite effect, Figure 1.12, (Jungman *et al.*, 1996).

The first acoustic peak represents the extreme of the fluctuation at the exact size of the sound horizon at the surface of last scattering. The angular scale subtended

by a fixed physical scale on the sky is given by the angular diameter distance of Section 1.1, equations (1.6) and (1.7). Thus the position of the first acoustic peak is a measure of the total density of the Universe, through its curvature, Ω equation (1.12), Figure 1.13. Therefore the CMB can be a useful way to estimate cosmological parameters accurately. However some degeneracies still exist. Models with the same angular diameter distance are difficult to distinguish.

If the curvature of the Universe is changed, the value of the Hubble constant will also be affected. Similarly, increasing the cosmological constant contribution does not change the shape of the oscillations, but shifts the conversion from the physical scale to the angular scale on the sky. This is analogous to *decreasing* the curvature. These degeneracies can be lifted by combining CMB data with large-scale-structure datasets, for example Percival *et al.* (2001), or supernova data, for example Perlmutter *et al.* (1999), Figure 1.14.

The CMBFAST code of Seljak and Zaldarriaga creates simulated cosmic microwave background power spectra using an integrated line-of-sight method. This code was used to create the plots in figures (1.10) to (1.13), and I have used the code to simulate Planck data for the developed tests of the microwave background.

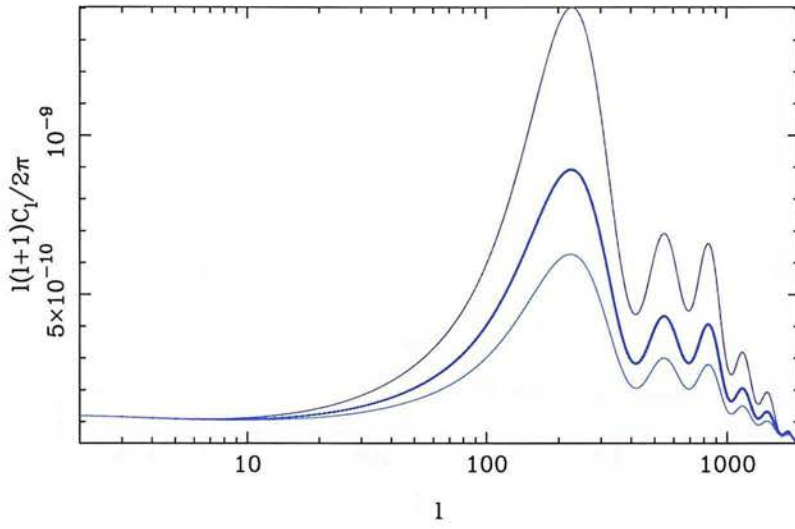


Figure 1.11: Plot of simulated CMB power spectra for varying scalar spectral indices. The blue line has $n = 1$, the purple line has $n = 1.05$, and the turquoise line has $n = 0.95$. All three spectra have been normalized to match the COBE observations at angular multipole $l = 2$.

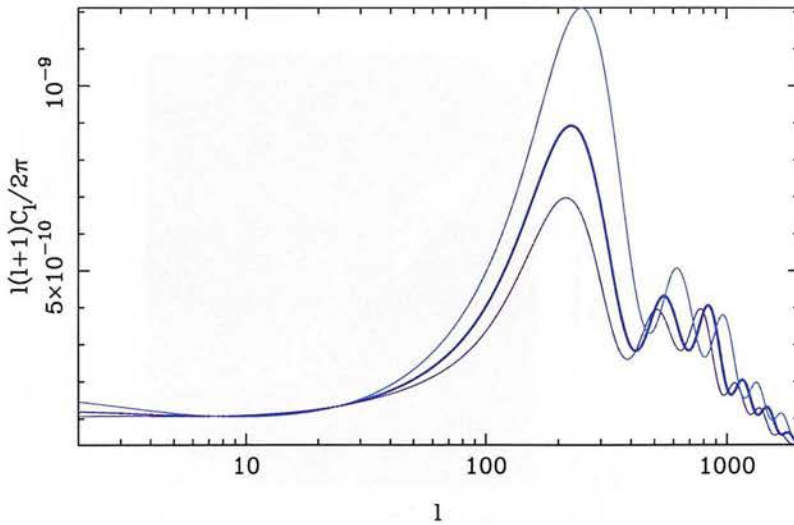


Figure 1.12: Plot of simulated CMB power spectra for varying cold dark matter content. The the power spectrum plotted in blue contains a 25% proportion of cold dark matter, with Ω_Λ equal to 0.7 and a baryon fraction of 0.05. The purple power spectrum contains the highest proportion of cold dark matter, 40%, with Ω_Λ equal to 0.56 and baryon fraction 0.04. The power spectrum plotted in turquoise has the lowest CDM fraction of 10%, $\Omega_\Lambda = 0.84$ and baryon fraction 0.06. So again, all three simulated power spectra have total density equal to 1.



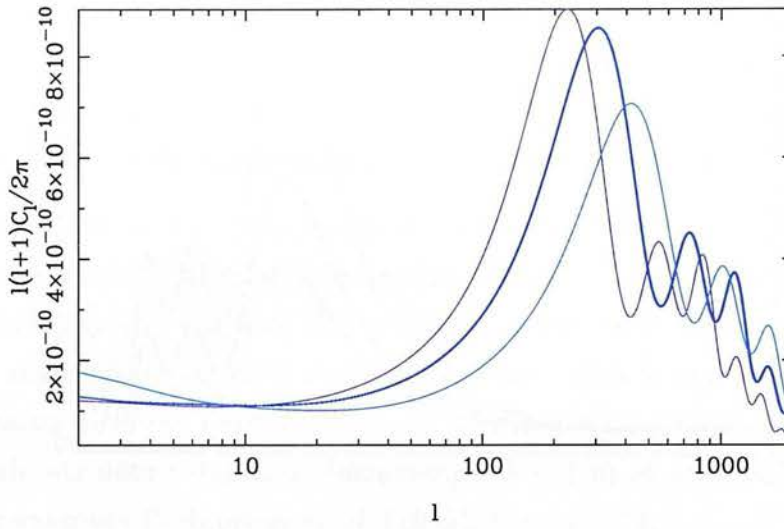


Figure 1.13: Plot of simulated CMB power spectra for different values of spatial curvature. The purple line shows the power spectrum for an $\Omega = 1$ universe. The universe of the blue power spectrum has a total density of 0.8. The turquoise line has the lowest total density of 0.6. I reduced all of the quantities contributing to the total density proportionally, so this plot is somewhat altered by other physical effects, such as the results of reducing the baryon content of a universe.

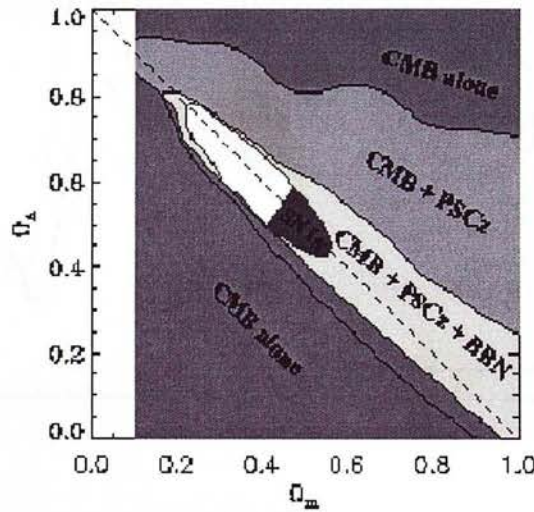


Figure 1.14: This plot of the $\Omega_m - \Omega_\Lambda$ slice of likelihood space is taken from Tegmark *et al.* (2001). Here, data from COBE and various other CMB experiments have been combined with the IRAS Point Source Catalogue Redshift dataset, and also with the predictions from Big Bang Nucleosynthesis, the favoured model for the formation of matter.

Chapter 2

The Correlation Function of Peaks

Now is a time of rapid development in the status of the experimental CMB data. The MAP and Planck Surveyor satellite experiments will produce CMB observations of unprecedented accuracy and completeness, offering the possibility of accurate determination of cosmological parameters, provided that the theoretical modelling around which it is based is proven applicable.

The first of my research projects, working with Alan Heavens, is a model-independent test of the Gaussianity of the anisotropies in the CMB (Heavens & Gupta 2001). A Gaussian spectrum of perturbations would be a key signature of a single field inflation model, and the limiting case for large numbers of fields in multiple field inflation models.

We have carried out the definitive calculation of the correlation function of peaks in the microwave background for Gaussian perturbations, for arbitrary peak separations on the sky. The resulting expression, for a given power spectrum, has no other parameter dependence, and applies for all sky separations, so it is complete.

The work in this chapter is divided into two parts. The first part I shall describe is the computation of the two-point correlation function of local maxima (or minima) in the temperature of the microwave background, in the case where it is a random Gaussian field. For a given power spectrum and peak threshold there are no adjustable parameters, and since this analysis does not make the small-angle approximation of Heavens & Sheth (1999), it is complete. We will see oscillatory features which are absent in the full temperature autocorrelation function, and

it will also be found that the small-angle approximation to the peak–peak correlation function is accurate to better than 0.01 on all scales. These high-precision predictions can form the basis of a sensitive test of the Gaussian hypothesis with upcoming all-sky microwave background experiments MAP and Planck, affording a thorough test of the inflationary theory of the early Universe. We also show how peak statistics can be a valuable tool in assessing and statistically removing contamination of the map by foreground point sources.

The second part of this project is a comparison of the performance of two tests of Gaussianity. To illustrate the effectiveness of the peak–correlation function technique, we apply it to simulated maps of the microwave sky arising from the cosmic string model of structure formation, and compare with the bispectrum as a non-Gaussian discriminant. We find that, for this non-Gaussian model, the peak–peak correlation function is a significantly better discriminant than the bispectrum, and even a $12.5^\circ \times 12.5^\circ$ patch of CMB sky can distinguish string induced perturbations from a Gaussian field.

2.1 Introduction

The cosmic microwave background radiation (CMB) presents an ideal opportunity to test theories of the early Universe. At the time of last scattering, the Universe was a relatively straightforward, almost uniform, mixture of photons, baryons, electrons and dark matter. The physics is well-understood, and free from the effects which complicate the interpretation of the present-day matter distribution. The microwave background thus offers the possibility of accurately testing models of structure formation. A generic test can readily be made between two classes of structure-formation model, based on inflation and cosmic defects respectively. There are several ways to do this; the power spectrum itself is a useful discriminant of specific models. We concentrate here on a generic test: most inflationary models predict that the microwave background temperature map will be very close to a random Gaussian field, whereas generically defect models predict a non-Gaussian temperature map. It turns out that testing the Gaussian nature of the initial fluctuations is easier through analysis of CMB fluctuations than large-scale structure (Verde *et al.*, 2000), although tests based on number densities of high-redshift objects may also be useful (Robinson *et al.*, 2000; Matarrese *et al.*, 2000).

Current evidence from Boomerang (de Bernardis *et al.*, 2001) and MAXIMA (Balbi *et al.*, 2001a,b; Stompor *et al.*, 2001) favours inflation models, since the power spectrum is acceptable for certain combinations of cosmological parameters. Indeed, the major scientific goal of these and future experiments such as the MAP and Planck Surveyor satellites is to derive cosmological parameters from the power spectrum. To make this interpretation requires that the temperature map is created by inflation or some similar process, not by defects, and that the map is not seriously contaminated by foregrounds. In both of these areas, the statistics of peaks can be a valuable tool. The process is quite straightforward: given a power spectrum, the statistical properties of peaks of a Gaussian field are fully determined — there are no free parameters. If the peaks are not consistent with the predictions, then either the CMB temperature map is not Gaussian, or it is significantly contaminated by foregrounds, or both. In either of these cases, the derived cosmological parameters from the power spectrum will be suspect. In this chapter, we compute the predictions for the correlation function of local maxima (and minima) for a Gaussian field. The analysis generalises the work of Heavens & Sheth (1999) by dropping the small-angle approximation: the results of this chapter can be used for all valid separations on the sky. There are several ways to test the Gaussian hypothesis, such as the three-point function (e.g. Hinshaw *et al.*, 1994; Falk *et al.*, 1993; Luo & Schramm, 1993; Gangui *et al.*, 1994), the genus and Euler-Poincaré statistic (Coles, 1988; Gott *et al.*, 1990; Luo, 1994b; Smoot *et al.*, 1994), the bispectrum (Luo, 1994a; Heavens, 1998; Ferreira *et al.*, 1998), studies of tensor modes in the CMB (Coulson *et al.*, 1994), excursion set properties (Barreiro *et al.*, 1998, 2001), peak statistics (Bond & Efstathiou, 1987; Kogut *et al.*, 1995, 1996; Barreiro *et al.*, 1997) and wavelet analyses (e.g. Mukherjee *et al.*, 2000; Aghanim & Forni, 1999; Forni & Aghanim, 1999). One advantage which the method presented here has above others is the possibility of assessing and removing contamination by foreground point sources. We return to this in the discussion. Non-Gaussian signals have been reported for the COBE map by Ferreira *et al.* (1998) (see also Pando *et al.*, 1998; Kamionkowski & Jaffe, 1998; Bromley & Tegmark, 1999; Mukherjee *et al.*, 2000; Magueijo, 2000). If this non-Gaussian signal is really present in the microwave background map, and not the result of some artefact (Banday *et al.*, 2000), then it would be a severe challenge to inflation models, as it is many orders of magnitude larger than expected (e.g. Verde *et al.*, 2000, and references therein).

2.2 Method

In this section, we compute the two-point correlation function of local maxima in 2D Gaussian random fields on the surface of a sphere. The method essentially follows that of Heavens & Sheth (1999), who used a Fourier analysis which assumed a flat sky. That analysis should be accurate for small separations; the analysis we present in this chapter is general.

2.2.1 Peaks on the surface of a sphere

We define the temperature fluctuation by $\delta(\theta, \phi) \equiv T(\theta, \phi)/\bar{T} - 1$, where \bar{T} is the mean temperature, and its spherical harmonic transform by

$$a_{\ell m} \equiv \int d^2\Omega \delta(\theta, \phi) Y_{\ell}^{m*}(\theta, \phi) \quad (2.1)$$

where $\Omega = (\theta, \phi)$. The inverse is

$$\delta(\theta, \phi) = \sum_{m=-\ell, \ell; \ell=0, \infty} a_{\ell m} Y_{\ell}^m(\theta, \phi) \quad (2.2)$$

If the temperature map is a random Gaussian field, the statistical properties of the fluctuations are specified entirely by the power spectrum, C_{ℓ} , defined by

$$\langle a_{\ell m} a_{\ell' m'}^* \rangle = C_{\ell} \delta_{\ell\ell'}^K \delta_{mm'}^K \quad (2.3)$$

where angle brackets indicate ensemble averages, and δ^K is a Kronecker delta function. The autocorrelation function of the temperature for points at (θ, ϕ) , (θ', ϕ') , separated by an angle ψ is

$$F(x) = \langle \delta(\theta, \phi) \delta(\theta', \phi') \rangle = \sum_{\ell} C_{\ell} \left(\frac{2\ell + 1}{4\pi} \right) P_{\ell}(x) \quad (2.4)$$

where $x = \cos \psi$ and P_{ℓ} is a Legendre polynomial. The remainder of the calculation of the peak–peak correlation function follows the method outlined in Heavens & Sheth (1999). We compute the 12×12 covariance matrix $M_{ij} = \langle v_i v_j \rangle$, where $v_i = (\mathbf{v}_1, \mathbf{v}_2)$ and the vectors \mathbf{v} specify the field and its derivatives at the two points: $\mathbf{v} = (\delta, \delta_{\phi}, \delta_{\theta}, \delta_{\phi\phi}, \delta_{\phi\theta}, \delta_{\theta\theta})$. Note that $\delta_{\phi} \equiv \partial\delta/\partial\phi$ etc. We show how to compute the components of the covariance matrix by an example, from which the other components can be readily generalised. Consider the correlation of

derivatives in the ϕ direction at two points (1) and (2):

$$\langle \delta_\phi^{(1)} \delta_\phi^{(2)*} \rangle = \sum_{\ell, m} \sum_{\ell', m'} \langle a_{\ell m} a_{\ell' m'}^* \rangle \frac{\partial}{\partial \phi_1} Y_\ell^m(\theta_1, \phi_1) \frac{\partial}{\partial \phi_2} Y_{\ell'}^{m'*}(\theta_2, \phi_2) \quad (2.5)$$

We take the derivatives outside the summation, use the orthogonality of the $a_{\ell m}$ (2.3), and use the addition theorem for spherical harmonics:

$$\sum_m Y_\ell^m(\theta_1, \phi_1) Y_\ell^{m*}(\theta_2, \phi_2) = \frac{2\ell + 1}{4\pi} P_\ell(x). \quad (2.6)$$

This yields

$$\langle \delta_\phi^{(1)} \delta_\phi^{(2)*} \rangle = \frac{\partial^2}{\partial \phi_1 \partial \phi_2} \sum_\ell \frac{2\ell + 1}{4\pi} C_\ell P_\ell(x). \quad (2.7)$$

Writing $x = \cos \theta_1 \cos \theta_2 + \sin \theta_1 \sin \theta_2 \cos(\phi_1 - \phi_2)$ we can differentiate to compute the covariance matrix element. This is aided by noting that these functions are independent of the absolute positions or orientations of the two points on the sphere, depending only on their separation. We can therefore simplify the algebra by taking $\theta_1 = \theta_2 = \pi/2$, $\phi_1 = 0$, and $\phi_2 = \phi$. This element simplifies to

$$\langle \delta_\phi^{(1)} \delta_\phi^{(2)*} \rangle = \sum_\ell \frac{2\ell + 1}{4\pi} C_\ell \left[\frac{dP_\ell(x)}{dx} \cos \phi - \frac{d^2 P_\ell(x)}{dx^2} \sin^2 \phi \right]. \quad (2.8)$$

Other elements are readily obtained by similar methods using Mathematica.

The two-point correlation function of peaks over heights ν_1 and ν_2 is the excess probability of finding two of the peaks separated by a distance r relative to the probability if there were no clustering. We invert M to get the joint probability distribution for the 12 variables,

$$p(\mathbf{v}_1, \mathbf{v}_2) = \frac{1}{(2\pi)^6 ||M||^{1/2}} \exp\left(-\frac{1}{2} v_i M_{ij}^{-1} v_j\right). \quad (2.9)$$

and integrate subject to constraints that the two points are maxima:

$$\begin{aligned} 1 + \xi(r|\nu_1, \nu_2) &= \frac{p(r|\nu_1, \nu_2)}{n_{pk}(\nu_1) n_{pk}(\nu_2)} \\ &= \frac{1}{4\theta_*^4 n_{pk}(\nu_1) n_{pk}(\nu_2)} \int_{X_1=0}^{\infty} \int_{X_2=0}^{\infty} \int_{Y_1=-X_1}^{X_1} \int_{Y_2=-X_2}^{X_2} \int_{Z_1=-\sqrt{X_1^2-Y_1^2}}^{\sqrt{X_1^2-Y_1^2}} \\ &\quad \int_{Z_2=-\sqrt{X_2^2-Y_2^2}}^{\sqrt{X_2^2-Y_2^2}} dX_1 dX_2 dY_1 dY_2 dZ_1 dZ_2 (X_1^2 - Y_1^2 - Z_1^2) \quad (2.10) \\ &\times (X_2^2 - Y_2^2 - Z_2^2) p(\nu_1, X_1, Y_1, Z_1, \eta_{\phi, \theta}^{(1)} = 0, \nu_2, X_2, Y_2, Z_2, \eta_{\phi, \theta}^{(2)} = 0). \end{aligned}$$

where $n_{pk}(\nu)d\nu$ is the number density of peaks between height ν and $\nu + d\nu$, given by A1.9 of Bond & Efstathiou (1987). By symmetry, (2.10) is also the correlation function of minima at $-\nu_1, -\nu_2$. We have defined the symbols

$$\begin{aligned}\nu &\equiv \frac{\delta}{\sigma_0} \\ \eta_\phi &\equiv \frac{\delta_\phi}{\sigma_1} \\ \eta_\theta &\equiv \frac{\delta_\theta}{\sigma_1} \\ X &\equiv -\frac{(\delta_{\phi\phi} + \delta_{\theta\theta})}{\sigma_2} \\ Y &\equiv \frac{(\delta_{\phi\phi} - \delta_{\theta\theta})}{\sigma_2} \\ Z &\equiv \frac{2\delta_{\phi\theta}}{\sigma_2}\end{aligned}\quad (2.11)$$

and the moments of the power spectrum are defined by

$$\begin{aligned}\sigma_0^2 &\equiv F(1) \\ \sigma_1^2 &\equiv 2F'(1) \\ \sigma_2^2 &\equiv 4[F'(1) + 2F''(1)]\end{aligned}\quad (2.12)$$

where $F'(1) = dF(x)/dx|_{x=1}$ etc. We also define the spectral parameters

$$\gamma \equiv \sigma_1^2/(\sigma_0\sigma_2) \quad \theta_* \equiv \sqrt{2}\frac{\sigma_1}{\sigma_2}.\quad (2.13)$$

These allow simplification of the covariance matrix, with variables in the order $(\nu_1, \eta_{\phi 1}, X_1, Y_1, \nu_2, \eta_{\phi 2}, X_2, Y_2, \eta_{\theta 1}, Z_1, \eta_{\theta 2}, Z_2)$, to the block form

$$M_{ij} = \begin{pmatrix} A & B & 0 \\ B^T & A & 0 \\ 0 & 0 & C \end{pmatrix}\quad (2.14)$$

where

$$A = \begin{pmatrix} 1 & \gamma & 0 & 0 \\ \gamma & 1 & 0 & 0 \\ 0 & 0 & \frac{1}{2} & 0 \\ 0 & 0 & 0 & (1 - \theta_*^2)/2 \end{pmatrix}.\quad (2.15)$$

Defining $h(x) \equiv F(x)/\sigma_0^2$, $S \equiv \sin \phi$ and $C \equiv \cos \phi$, $B =$

$$\begin{pmatrix}
h & \frac{\theta_*^2 (2C h' - S^2 h'')}{2\gamma} & -\frac{S \theta_* h'}{\sqrt{2}\gamma} \\
B_{21} & \frac{\theta_*^4 [4C h' + (8C^2 - 6S^2) h'' - 8C S^2 h^{(3)} + S^4 h^{(4)}]}{4\gamma^2} & \frac{S \theta_*^3 (-2 h' - 4C h'' + S^2 h^{(3)})}{2\sqrt{2}\gamma^2} \\
-B_{13} & -B_{23} & \frac{\theta_*^2 (C h' - S^2 h'')}{2\gamma^2} \\
B_{14} & B_{24} & -B_{34} \\
& & \frac{S^2 \theta_*^2 h''}{2\gamma} \\
& & \frac{\theta_*^4 (6S^2 h'' + 6C S^2 h^{(3)} - S^4 h^{(4)})}{4\gamma^2} \\
& & \frac{S \theta_*^3 (-2C h'' + S^2 h^{(3)})}{2\sqrt{2}\gamma^2} \\
& & \frac{\theta_*^4 [2(1+C^2) h'' - 4C S^2 h^{(3)} + S^4 h^{(4)}]}{4\gamma^2}
\end{pmatrix}, \quad (2.16)$$

where $h^{(3)}(x) \equiv h'''(x)$ etc, and we write the lower triangle in terms of the upper triangular matrix for conciseness. Finally,

$$C = \begin{pmatrix}
\frac{1}{2} & \frac{\theta_*^2 h'}{2\gamma^2} & 0 & -\frac{S \theta_*^3 h''}{\sqrt{2}\gamma^2} \\
\frac{\theta_*^2 h'}{2\gamma^2} & \frac{1}{2} & \frac{S \theta_*^3 h''}{\sqrt{2}\gamma^2} & 0 \\
0 & \frac{S \theta_*^3 h''}{\sqrt{2}\gamma^2} & \frac{1 - \theta_*^2}{2} & \frac{\theta_*^4 (C h'' - S^2 h^{(3)})}{\gamma^2} \\
-\frac{S \theta_*^3 h''}{\sqrt{2}\gamma^2} & 0 & \frac{\theta_*^4 (C h'' - S^2 h^{(3)})}{\gamma^2} & \frac{1 - \theta_*^2}{2}
\end{pmatrix}. \quad (2.17)$$

The correlation function for peaks above a certain threshold ν is obtained by performing two further integrations over ν_1 and ν_2 , and replacing the differential number densities $n_{pk}(\nu)$ in the denominator of (2.10) by numerically-evaluated integrals $n_{pk}(> \nu)$. For peaks above a threshold, the 8D integration can be reduced to 6, as the integrals over ν_2 and z_2 can be done analytically. Very accurate integrations can then be done on a desktop workstation in about 50 seconds.

2.3 Results

We run CMBFAST (Seljak & Zaldarriaga, 1996) to generate the power spectrum C_ℓ , and model the beam with a Gaussian of FWHM b by multiplying the power spectrum by a Gaussian $\exp[-\sigma^2 \ell(\ell + 1)]$, with $\sigma = b/\sqrt{8 \ln 2}$. We have not included the effects of gravitational lensing on the temperature field. As shown by Takada *et al.* (2000), the effect is small except for separations up to the first peak, where the anticorrelation is reduced in magnitude. Figs. 2.1 and 2.2 show the correlation function of peaks above a 1σ threshold for a mixed dark matter model,

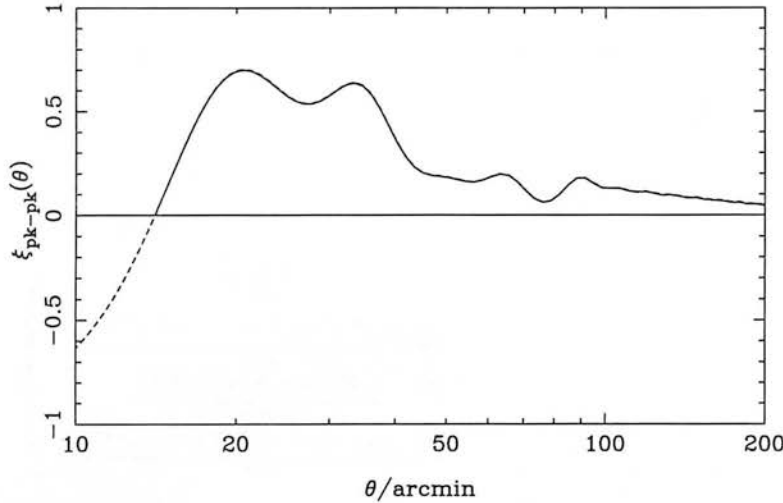


Figure 2.1: (Solid line) The correlation function for peaks above a $+1\sigma$ threshold, in a mixed dark matter model with CDM, vacuum and baryon density parameters $\Omega_{CDM} = 0.8$, $\Omega_\nu = 0.15$ and $\Omega_B = 0.05$. Hubble constant is $H_0 = 60 \text{ km s}^{-1} \text{ Mpc}^{-1}$. For comparison, the flat-sky results of Heavens & Sheth (1999) are shown dotted. The results coincide to an accuracy of better than 0.004.

along with the results of the flat-sky calculation of Heavens & Sheth (1999). The differences above 200 arcminutes separation are at the level of ~ 0.005 , and appear to be an offset between the two functions. The cosmic variance error on a correlation measurement creates symmetric uncertainty, equally likely to over or underpredict the magnitude of the correlation function. The plot in Figure 2.2 shows a calculation of the two correlation functions carried out using numerical integration. The accuracy of the numerical integration was tested, showing a level of error converging to 0.0003, which, comparing to the difference between the full and flat sky codes, ~ 0.005 , shows that these differences in the predictions of the two point correlation function of peaks, made using the full and flat sky assumption, are real.

2.4 Correlation function vs bispectrum for string maps

The statistics of non-Gaussian fields, with a very few exceptions, such as the chi-squared field, are very difficult to calculate. In most cases the only test of the statistics for a specific non-Gaussian distribution would call for involved simulations of physical processes, and generation of a large number of realisations from

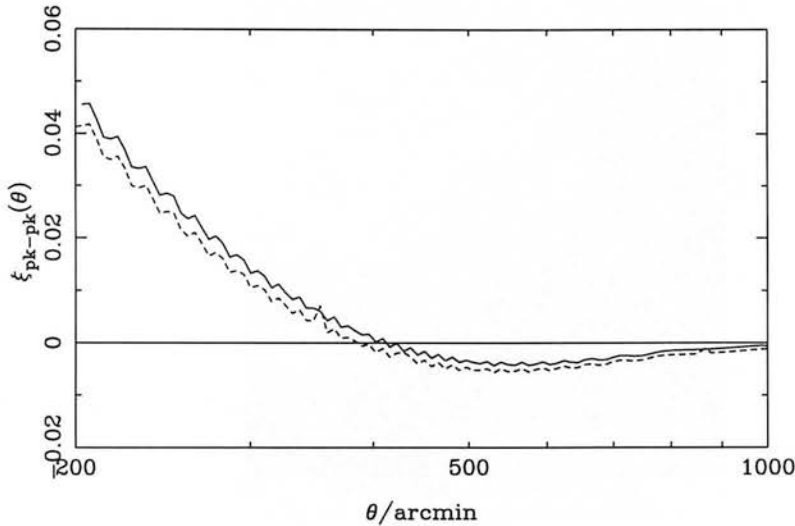


Figure 2.2: As Fig. 2.1, but at larger angle separations between 3.3 and 16.7 degrees.

the simulation of the model for statistical averaging. Therefore, in order to test for non-Gaussianity, many tests of Gaussianity have been developed. The methods will fare differently depending on the exact properties of the non-Gaussian field considered. Here we focus on one particular non-Gaussian field, produced by a network of cosmic strings. Fig. 2.3 shows a realisation of the temperature map expected from cosmic strings, one of two very kindly provided for us by Francois Bouchet. The lensing effect of the moving strings is added to a Gaussian background map, approximately as expected from the string model (Pen *et al.*, 1997) (see also Simatos & Perivolaropoulos, 2000; Avelino & Martins, 2000). We consider two diagnostics: the peak-peak correlation function, and the bispectrum (e.g. Heavens, 1998; Ferreira *et al.*, 1998; Gangui & Martin, 2000). The string maps we have are 12.5° by 12.5° , and we would expect the bispectrum to have difficulty in distinguishing these maps from Gaussian maps with the same power spectrum (Luo, 1994a). The interesting question is whether the peak correlation function can do better. Since the string simulations are performed on a small, close-to-flat patch on the sphere of the sky, we use a Fourier transform to compute the flat-sky bispectrum from the Fourier coefficients $\delta(\mathbf{k}) \equiv \int d^2\mathbf{x} \delta(\mathbf{x}) \exp(i\mathbf{k} \cdot \mathbf{x})$. The values of the bispectrum and power spectrum, as introduced in Section 1.3, equations (1.98) and (1.94), are thus projected onto a 2D surface.

$$\langle \delta(\mathbf{k}_1) \delta(\mathbf{k}_2) \delta(\mathbf{k}_3) \rangle = (2\pi)^2 B(k_1, k_2, k_3) \delta_D^2(\mathbf{k}_1 + \mathbf{k}_2 + \mathbf{k}_3) \quad (2.18)$$

$$\langle \delta(\mathbf{k}_1) \delta(\mathbf{k}_2) \rangle = (2\pi)^2 P(k_1) \delta_D^2(\mathbf{k}_1 + \mathbf{k}_2) \quad (2.19)$$

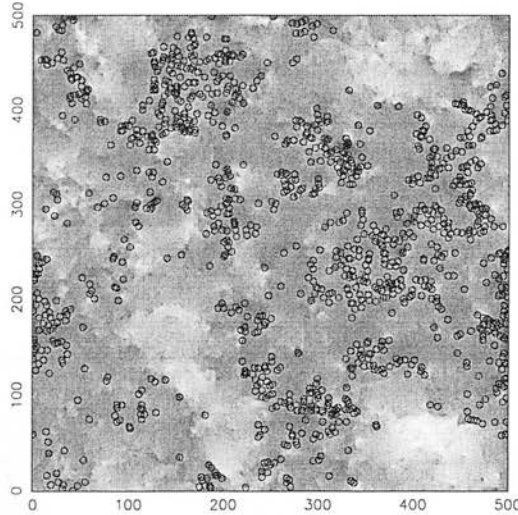


Figure 2.3: Simulated sky map for cosmic strings, consisting of a Gaussian background, with the lensing effect of a string network superimposed. Peaks above 1σ are circled.

These are the continuous forms. The temperature variation in the sky is of course continuous, but working with data on a computer usually means using discrete values of position and the data is in a finite square (Figure 2.4). The data are two 500 by 500 arrays of discrete values of $\delta T/T$ in units of 2×10^{-6} . The Fourier transforms we use for the analysis of simulated sky maps are thus discrete transforms. Therefore the $\delta(\mathbf{k})$ is a discrete transform in a finite box, not over all space.

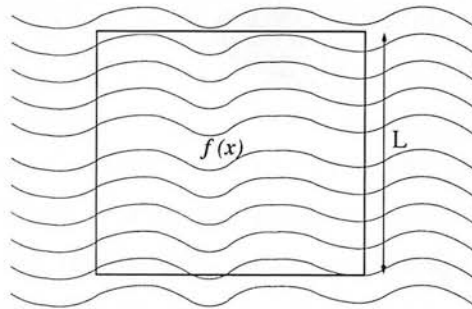


Figure 2.4: Discrete box imposed on CMB sky.

As a result of this, the delta function

$$\delta_D^2(\mathbf{k}_1 + \mathbf{k}_2) \rightarrow \left(\frac{L}{2\pi}\right)^2 \delta_{\mathbf{k}_1, -\mathbf{k}_2}^K, \quad (2.20)$$

where δ^K is the Kronecker Delta.

$$\delta(\mathbf{x}) \rightarrow \sum_{n_x, n_y=0}^{500} \exp(-i\mathbf{k} \cdot \mathbf{x}) \delta(\mathbf{k}). \quad (2.21)$$

$$\mathbf{k} = \frac{2\pi}{L} \begin{pmatrix} n_x \\ n_y \end{pmatrix}, \quad (2.22)$$

n_x and n_y are integers.

In practice, the quantity used in the analysis of the maps is the bispectrum estimator,

$$D_\alpha = \frac{\text{Re}(\delta(\mathbf{k}_1)\delta(\mathbf{k}_2)\delta(\mathbf{k}_3))}{L^2} \quad (2.23)$$

$$\langle D_\alpha \rangle = \langle B(k_1, k_2, k_3) \rangle. \quad (2.24)$$

This quantity is equivalent to the bispectrum, as the bispectrum triangles in Figure 2.5 are equivalent to each other.

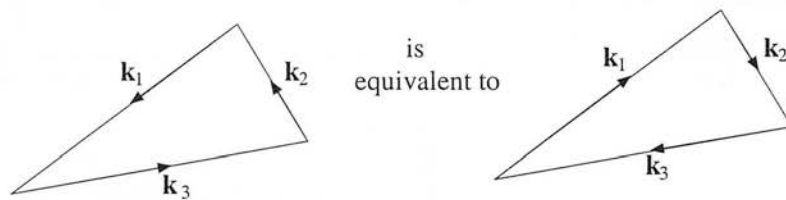


Figure 2.5: The triangles in this figure are equivalent for bispectrum evaluation, therefore $\langle \delta(\mathbf{k}_3)\delta(\mathbf{k}_2)\delta(\mathbf{k}_1) \rangle = \langle \delta(\mathbf{k}_{-1})\delta(\mathbf{k}_{-2})\delta(\mathbf{k}_{-3}) \rangle = \langle \delta(\mathbf{k}_1^*)\delta(\mathbf{k}_2^*)\delta(\mathbf{k}_3^*) \rangle$. Symmetry leaves only the real part of the bispectrum.

This bispectrum estimator is evaluated for \mathbf{k}_1 , \mathbf{k}_2 and \mathbf{k}_3 forming a closed triangle: $\mathbf{k}_1 + \mathbf{k}_2 + \mathbf{k}_3 = 0$. We test for two specific cases, equilateral triangles and triangles of zero area, following the work of Matarrese *et al.* (1997) and Verde *et al.* (1998) which apply to large-scale structure.

Considering first the equilateral triangles (Figure 2.6). The data in the resulting Fourier transformed box are not all independent, from the relation $\delta(\mathbf{k}) = [\delta(-\mathbf{k})]^*$, arising from the reality of $\delta T/T$. There are also symmetry constraints from the choice of triangle. The symmetry of equilateral triangles means that if \mathbf{k}_1 , the position vector of one of the vertices, is chosen first all along one axis, and then chosen along the length of a line rotated through every angle from the axis up to but not including 120° , all possible equilateral triangles in the space have been covered (Figure 2.7).

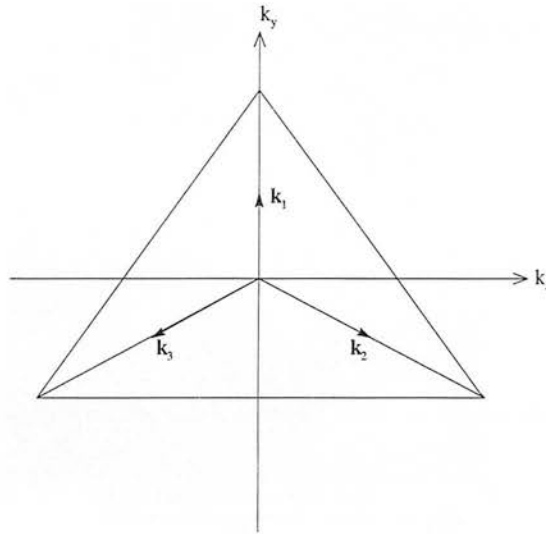


Figure 2.6: Equilateral triangle of wavevectors centred on origin.

However, the constraint that $\delta(\mathbf{k}) = [\delta(-\mathbf{k})]^*$ means the triangle resulting from the reflection of a triangle through the origin is not independent from the first, and all the required data is recovered from rotating \mathbf{k}_1 through every value up to but not including 60° .

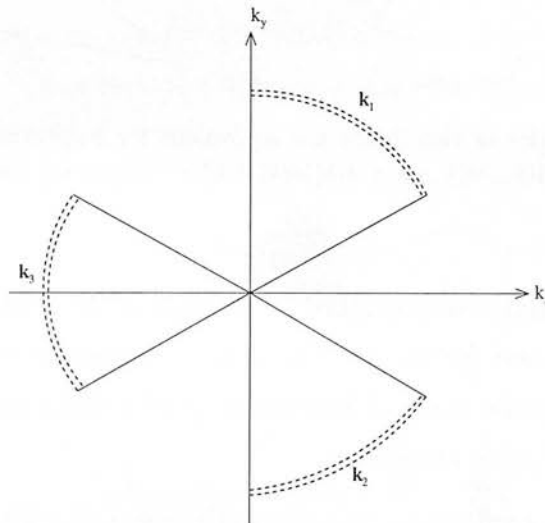


Figure 2.7: Regions of independent information for the equilateral triangle case.

D_α is averaged over thin shells of k . The triangles will still not be precisely equilateral, due to the data being in discrete pixels.

The other type of triangle we used is composed of one vector in direction \mathbf{q} of length k , and two identical unit vectors of length $1/2 k$ in direction $-\mathbf{q}$.

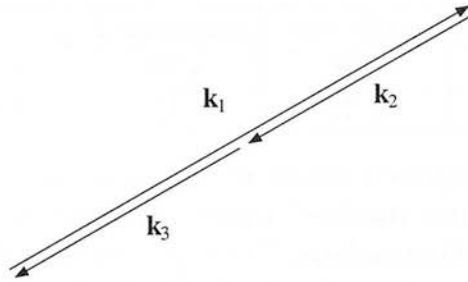


Figure 2.8: Zero-area triangle.

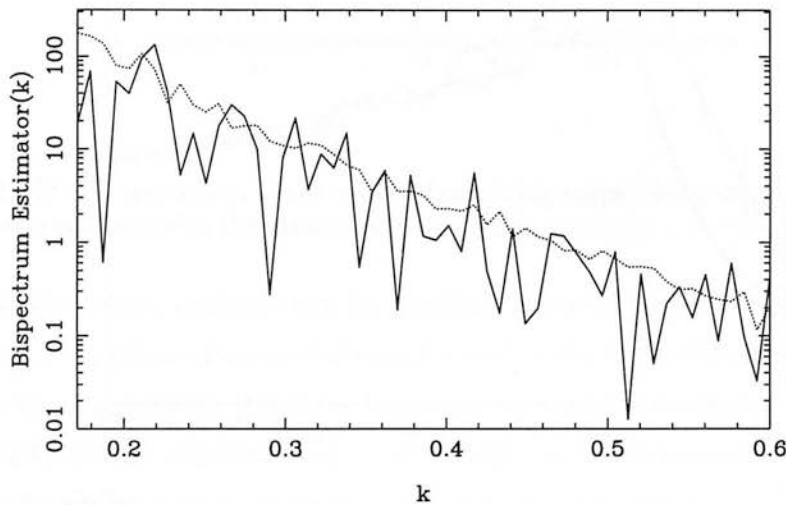


Figure 2.9: The equilateral bispectrum as estimated from map with string foreground and Gaussian temperature on last-scattering surface (solid), and cosmic r.m.s. (dotted).

These zero-area triangles (2.8) have only the $\delta(\mathbf{k}) = [\delta(-\mathbf{k})]^*$ constraint and therefore all triangles with \mathbf{k}_1 anywhere in the $k_x \geq 0$ half of the box were used in the analysis.

We calculate values for $\log D_\alpha$ in 100 bins of k ,

$$\text{BIN} = \left[\frac{N_{\text{BINS}} - 1}{k_{\text{max}} - k_{\text{min}}} \times (k - k_{\text{min}}) \right] + 1 \quad (2.25)$$

and average over each. We also calculate the power spectrum averaged over each bin, and use these values to calculate the errors for D_α (Appendix J).

Fig. 2.9 displays the equilateral estimated bispectrum for the string map shown in Fig. 2.3. Also shown is the cosmic r.m.s. for a Gaussian field of the same power spectrum, $\langle |\delta_{\mathbf{k}}|^2 \rangle^{3/2}$. We show in Table 2.1 reduced χ^2 values for both equilateral triangles and zero-area triangles for the two simulated maps. With 55 bins, the variance in the reduced χ^2 for a Gaussian field is shown in the final

	equilateral	zero-area	$\sqrt{2/(n-1)}$
Map 1	1.06	0.96	0.19
Map 2	1.29	1.42	0.19

Table 2.1: Reduced χ -squared values of the deviation of the bispectra from a Gaussian model of the two modified maps, consisting of intrinsic Gaussian and cosmic string generated fluctuations. The r.m.s. of the reduced χ^2 for a Gaussian model with $n = 55$ data is shown in the final column.

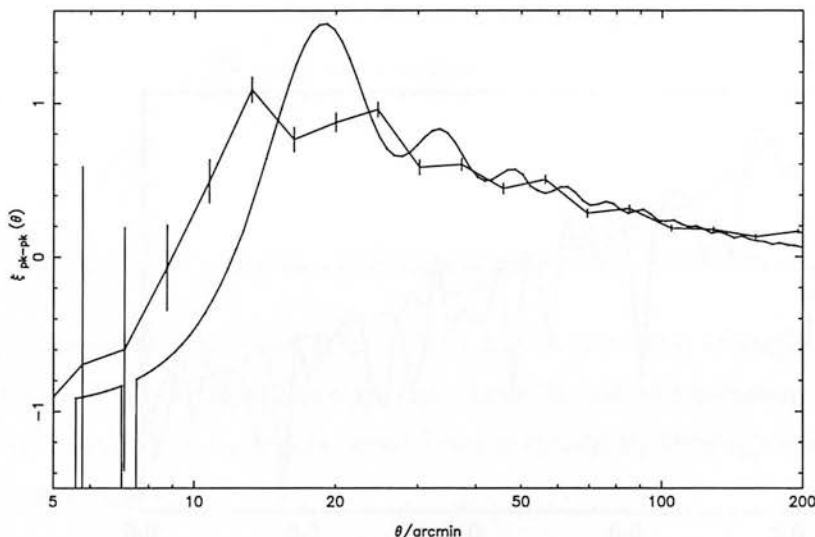


Figure 2.10: The correlation function of peaks above 1σ calculated from the map of Fig. 2.3. Errors are Poisson, and hence underestimates. Superimposed is the correlation function from a Gaussian map with the same power spectrum. Note the excess of string peaks around 10–15 arcminutes.

column. We find no significant departure from Gaussianity with this test.

Fig. 2.10 shows the correlation function of peaks above 1σ (where σ^2 is the map variance) for the map shown in Fig. 2.3. The map is smoothed with a Gaussian beam of FWHM $5.5'$ to model the Planck beam. The errors for the peak–peak correlation function are Poisson errors, which will be underestimates. However, it is clear that the peak correlation function of the string map is significantly different from that of a Gaussian map with the same power spectrum. The most striking difference is the presence of peaks in the string map which are separated by 10 – 20 arcminutes. These appear in greater numbers than in the Gaussian map, and this could be the most obvious manifestation of strings. We note that the number density of peaks in the smoothed maps is not as powerful a discriminant, as seen in Fig. 2.11. There appear to be no significant deviations from the Gaussian curve, although one should bear in mind that no calculation exists for the probability distribution of the heights, only for its mean. Finally, we

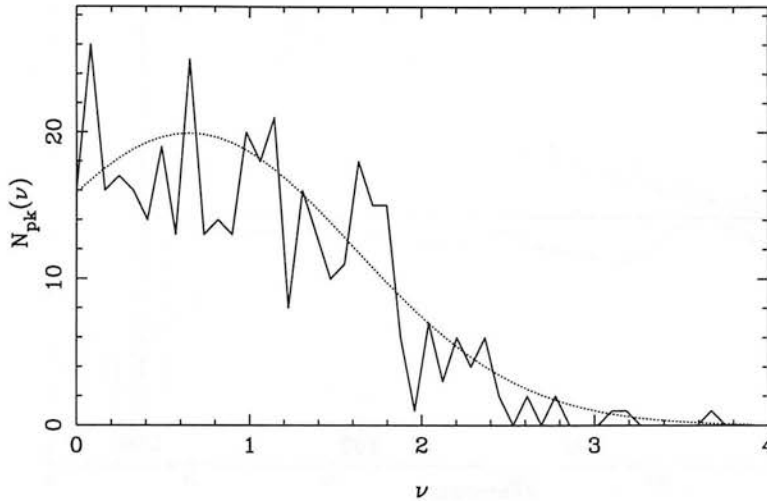


Figure 2.11: The number of peaks in one of the string maps, along with the expected number from a Gaussian field with the same power spectrum.

note that the peaks analysis can be applied to certain non-Gaussian fields, where the field is a function of an underlying Gaussian field. For illustration, in Fig. 2.12 we show the correlation function for peaks in a χ^2 field, where $\delta \equiv g^2 - \sigma_0^2$, with g being a Gaussian random field. This is equivalent to the correlation function of the set containing peaks above $\nu = 1$ and minima below $\nu = -1$ in the Gaussian field. It can be computed by extension of the methods here, integrating equation (2.10) over 4 separate regions for $\nu_{1,2} > \nu$ and $\nu_{1,2} < -\nu$. Note the low level of correlation, as minima populate the large-scale underdensities in the Gaussian field. This is readily understood (Heavens *et al.*, 1998).

2.5 On Further Testing The Test

We have compared two methods of detecting non-Gaussianity, the bispectrum and the correlation function of peaks, with the predictions from a specific early Universe model, cosmic strings. The fluctuation distribution is caused by two separate mechanisms. First, the cosmic string network causes a spectrum of perturbations at the surface of last scattering which is very close to Gaussian. The mechanism and the spectrum of these perturbations were predicted in Pen *et al.* (1997). Using this predicted power spectrum we generated realisations of Gaussian noise to model this first generation of cosmic string CMB inhomogeneities. The second generation of CMB fluctuations caused by cosmic strings is due to

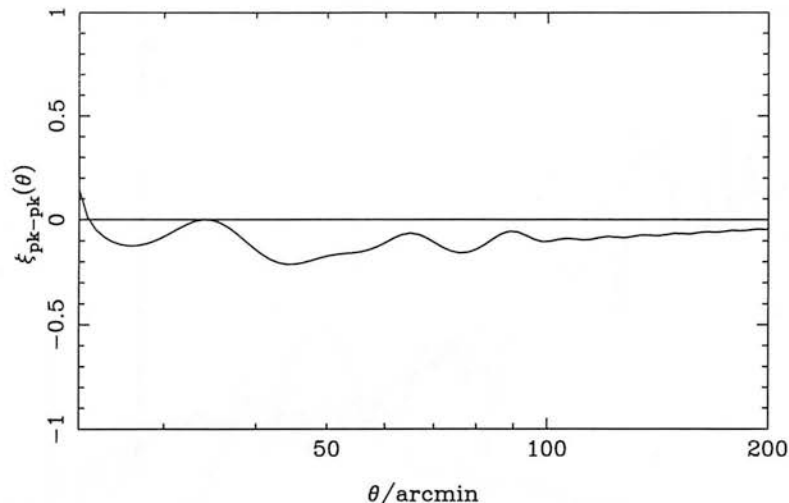


Figure 2.12: Correlation function of peaks above the mean in a (non-Gaussian) χ^2 field. The power spectrum of the underlying Gaussian field is a mixed dark matter model.

gravitational lensing from the moving strings, and the map provided by Francois Bouchet simulated these. By combining these sets of fluctuations we tested a realization of the fluctuations from the structure formation model.

We did not test our ability to detect non-Gaussianity in the CMB temperature field due to foreground sources, although the detection of clustering on small scales should be a strength of this test.

We test the test now for higher levels of Gaussian emission, to see where the test fails to pick out the strings. The ratio of the root mean squared fluctuation from the gravitational lensing effect to that of the Gaussian background, as predicted by simulations of the strings models, is : Lensing r.m.s./Gaussian r.m.s = 3.734. We now adjust the amplitude of the essentially non-Gaussian lensing-generated fluctuations and the simulated Gaussian string-network background fluctuations to make the ratio of their root mean squares equal to one. This is not a prediction of the theory, but an artificial construction to test the distinguishing ability of the peak-correlation function. The result is plotted in Figure 2.13, which shows that at such a level of Gaussian background the test is not successful.

2.6 Conclusions

We have presented calculations of the exact correlation function of peaks in a random Gaussian field defined on the surface of a sphere. No small-angle ap-

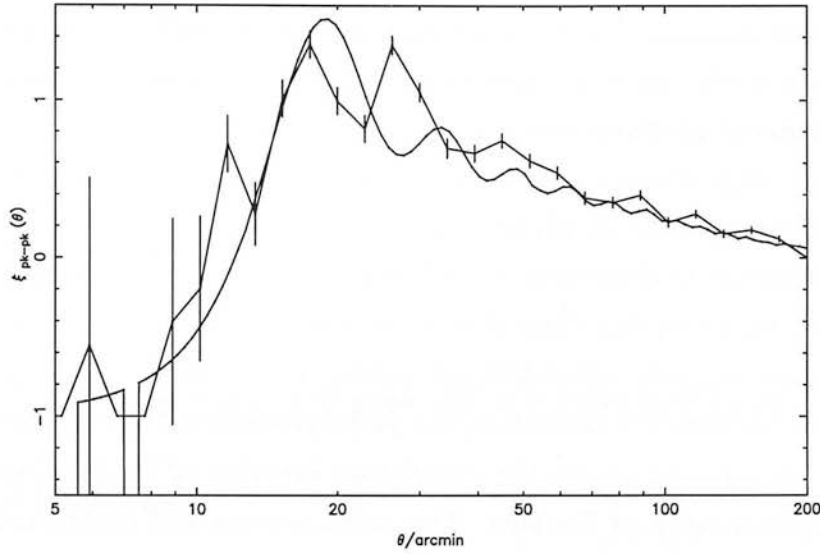


Figure 2.13: The correlation function of peaks when the relative Gaussian emission is increased to become comparable to the foreground lensing effects.

proximation is made, so the method is an advance on the flat-sky computations of Heavens & Sheth (1999) and now effectively complete. The formalism allows very accurate theoretical predictions of the peak-peak correlation function for temperature fluctuations in the microwave background, which is the application considered here. This test can be applied just as effectively to the distribution of either maxima or minima in the case where the data consists of only CMB photons. However, in the case of incomplete removal of foreground sources, they will effect the distribution of maxima. We envisage the main use of this method being as a sensitive test of the Gaussian hypothesis. Since inflationary models generically predict a temperature field which is very close to Gaussian, this is a consistency test for inflation. Other structure formation models, based for example on strings, predict non-Gaussian temperature maps. Although the visual appearance of string maps is evidently non-Gaussian, it is not necessarily easy to find statistics which will unambiguously distinguish them from Gaussian fields. To illustrate this point, we have analysed 12.5-degree square simulated maps of string models, using the bispectrum and the peak-peak correlation function as distinguishing statistics. We find that, while cosmic variance in the bispectrum makes it difficult to use on a small patch of sky, the peak-peak correlation function clearly rules out a Gaussian map.

In practice, maps of the microwave background will be contaminated at some level by point sources, amongst other things. Peak statistics may be useful in

assessing this contribution. The most straightforward example is that an uncontaminated map has the same average number density of maxima and minima; a significant excess of maxima would be indicative of contamination. Unfortunately the theory of peaks is not currently able to tell us the *distribution* of the number of maxima or minima within a finite sky (only its mean), but it is a straightforward matter to determine the distribution by monte carlo realisations. One can attempt to go further than this, by removing statistically the contribution from the point sources, provided one knows from other observations what their correlation function is. Assuming the point sources are uncorrelated with the microwave background peaks, the correlation function of the combined map is simply a weighted mean of the two. The point sources will contribute to the power spectrum; one can vary the assumed contribution from point sources and modify the power spectrum and the derived microwave background peak correlation function accordingly. If consistency can be achieved, one will be confident both of the Gaussian nature of the microwave background, and the level of point source contamination.

Chapter 3

Fast Parameter Estimation using MOPED

The statistical properties of a map of the primary fluctuations in the cosmic microwave background (CMB) may be specified to high accuracy by a few thousand power spectra measurements, provided the fluctuations are Gaussian, yet the number of parameters relevant for the CMB is probably no more than about 10 – 20. There is consequently a large degree of redundancy in the power spectrum data. Alan Heavens and I have carried out an analysis to show that the MOPED¹ data compression technique (Heavens *et al.*, 2000) can reduce the CMB power spectrum measurements to about 10-20 numbers (one for each parameter), from which the cosmological parameters can be estimated virtually as accurately as from the complete power spectrum. This offers opportunities for very fast parameter estimation from real and simulated CMB skies, with accurate likelihood calculations at Planck resolution being speeded up by a factor of around five hundred million.

3.1 Introduction

Previous measurements of the CMB power spectrum, using balloon experiments, have produced estimates of cosmological parameters such as Ω_0 , H_0 and Ω_Λ (Balbi *et al.*, 2001a,b; Stompor *et al.*, 2001; de Bernardis *et al.*, 2001; Bond & Efstathiou, 1987; Kamionkowski *et al.*, 1994; Jungman *et al.*, 1996). There is a review of the way various cosmological parameters effect the CMB in Section (1.3). The CMB

¹MOPED stands for *Multiple Optimised Parameter Estimation and Data Compression*

is not the sole dataset useful for the estimation of these parameters. Cosmological parameter estimation has been carried out also with large-scale structure surveys, see for example Percival *et al.* (2001). However, the CMB photons were released at a time when the overdensities in the matter distribution of the Universe were developing linearly under the influence of gravity. Thus the physics of the CMB is much more straightforward than the complicated gravitational processes which effect the large-scale structure of the Universe.

The limitations remaining in current technology for measuring the cosmic microwave background are in the estimation of two quantities: the contribution of foreground sources emitting in microwave frequencies, and instrumental noise effects. The most recent CMB datasets which have produced cosmological parameter estimates are the Boomerang (de Bernardis *et al.*, 2001) and MAXIMA (Balbi *et al.*, 2001a,b; Stompor *et al.*, 2001) balloon experiments. They have demonstrated that the above limitations do not hinder accurate parameter estimation.

As experiments become more ambitious, the data processing requirements become more demanding, and the current datasets have sufficiently many pixels ($\sim 10^4 - 10^5$) that the data processing is already quite challenging. Even the first measurement of the CMB fluctuations, produced by the Cosmic Background Explorer (COBE) satellite (Smoot *et al.*, 1992) produced a dataset with enough pixels (~ 4000) for data compression techniques to be valuable (Gorski, 1994; Gorski K. *et al.*, 1994; Bond, 1995; Bunn & Sugiyama, 1995). For the satellite experiments MAP (the Microwave Anisotropy Probe) and Planck (the Planck Surveyor Satellite), data compression will be vital. Each will provide very large datasets, with close to all-sky coverage with a resolution of up to 5 arcminutes, and $\sim 10^6 - 10^7$ pixels. The standard radical compression method is to reduce the map to a set of power spectrum estimates (see e.g. Bond *et al.*, 1998). In principle this compression can be lossless, if the map is a Gaussian random field, as closely predicted by inflation (see e.g. Gangui *et al.*, 1994; Verde *et al.*, 2000; Wang & Kamionkowski, 2000), as all the statistical properties of the map are calculable from the power spectrum. The power spectrum data, typically a few thousand numbers for a high-resolution experiment, can then be used to estimate cosmological parameters to an accuracy of a few percent. The steps in the distillation of the raw data to the cosmological parameters are, however, not necessarily computationally straightforward (see e.g. Wright, 1996; Muciaccia *et al.*, 1997;

Tegmark, 1997a,b; Bond *et al.*, 1999; Olive *et al.*, 1999; Borrill, 1999; Szapudi *et al.*, 2001; Natoli *et al.*, 2001).

We address one aspect of this problem: parameter estimation from the power spectrum. In this chapter I shall review our introduction of the implementation of an eigenvector-based method for data compression for a CMB dataset.

MOPED is an approach to data compression which was introduced by Heavens, Jimenez and Lahav in 2000, reducing the surplus data in a galaxy spectrum where one, two or three quantities needed to be estimated.

We propose that the application of MOPED to the problem of parameter estimation from the upcoming Planck data would result in very accurate and extremely fast parameter estimation, and show that our algorithm for this process produced a speed-up over the brute-force maximum likelihood method, which is the primary approach to parameter estimation, on simulated Planck data of between 10^7 and 10^9 .

Heavens *et al.* (2000), henceforth HJL, show that datasets with certain noise properties offered possibilities for very radical linear compression of the data without any loss of information about the parameters which determine the data. The requirement is for a dataset whose mean depends on the parameters, but the covariance of the noise does not. In these circumstances, it is possible to find a set of linear combinations of the data which are *locally sufficient statistics* for the parameters - i.e. the compressed data contain as much information about the parameters as the full dataset, and in this sense the compression is lossless (strictly, the Fisher matrix is unchanged, so the likelihood surface is known to be unchanged only locally near the peak). The compressed dataset can be extremely small - it consists of a single number for each parameter. Thus for highly redundant datasets, the degree of compression can be very large.

It is important to recognise that the data compression can still be done even if the assumptions for lossless compression do not apply. In HJL, for example, the data compression algorithm was applied to the case of galaxy spectra, where the noise includes a photon counting noise term which is dependent on the mean number of photons in the spectral channel, and hence does depend on the parameters of the galaxy. The compressed data can still be used for parameter estimation, but the error bars on the derived parameters are fractionally larger than by using the full spectrum. The same situation arises in the CMB: under general assumptions,

the cosmic variance on a power measurement is proportional to the square of the power itself, and therefore is dependent on the underlying parameters. The data compression, although not lossless, is still highly efficient: the expected increase in parameter error can be as little as 0.1%. The time required for a brute-force likelihood evaluation is broadly comparable to the time it takes to compute theoretically the power spectrum of a model, using CMBFAST (Seljak & Zaldarriaga, 1996). However, recent developments (Tegmark *et al.*, 2001) have speeded up the step involving simulated CMB power spectra generation for the required range of models with different values of cosmological parameters. The improvement in time, for this primary step in the likelihood analysis, is a factor of 10^3 , so a brute-force parameter search would be dominated by the time it takes to carry out the second step: evaluating the likelihood. The relative timings for these two steps can determine the analysis strategy, since if the computation of the theoretical power spectrum is small in comparison with the likelihood evaluation, one can calculate the power spectrum ‘on the fly’ as one searches through parameter space. A useful goal is therefore to make the likelihood evaluation much quicker than CMBFAST. One can already speed up this process by using variants of the Newton-Raphson method (see, e.g. Bond *et al.*, 1999).

3.2 Massive Lossless Data Compression

We show that MOPED does successfully recover cosmological parameters from simulated datasets, many orders of magnitude more quickly than brute-force likelihood methods, therefore the analysis of CMB data does not need to be dominated by likelihood evaluations. We also show that the parameter errors are similar to the full maximum likelihood solution.

In this section I shall first review maximum likelihood parameter estimation, before detailing the method of massive lossless data compression.

3.2.1 The Brute-Force Maximum Likelihood Method of Parameter Estimation From the CMB Power Spectrum

The brute force maximum likelihood method of parameter estimation from a dataset was introduced by Fisher (1935). I shall explain this method, the notation

for our analysis and state the theorems on which the error estimation is based. Detailed derivations of the results stated here can be found in statistics textbooks, such as Kendall & Stuart (1969).

The data is an estimate of the power spectrum measured from the CMB map of the sky. \hat{C}_ℓ represents the data vector. The measured quantity will contain two components: a signal, C_ℓ , which is the true power spectrum, and noise, n_ℓ , which represents the uncertainty on the measurement of the power spectrum. Both the components are functions of the cosmological parameters, $\{\theta_\alpha\}$.

$$\hat{C}_\ell = C_\ell(\theta_\alpha) + n_\ell(\theta_\alpha) \quad (3.1)$$

In our analysis the noise we take into account for the data is the noise on the Planck dataset. Instrumental and foreground noise effects for Planck will be minimal, therefore the uncertainty on the observed power spectrum will be dominated by cosmic variance. The cosmic variance on a multipole, ℓ , of the power spectrum, is

$$\frac{2C_\ell^2}{(2\ell + 1)}, \quad (3.2)$$

and the cosmic noise is a Gaussian distribution with mean zero.

The sky map from which \hat{C}_ℓ is estimated may not be complete. When the power spectrum is measured, the ensemble average over all possible skies is replaced by a spatial average over the sky. This substitution is possible due to the assumption of ergodicity, Section (1.3.1) (Adler, 1981), which is the assumption that one Gaussian distribution can be substituted for another. It is assumed, for the purposes of error analysis, that the perturbations distributed over the CMB sky form a Gaussian distribution. However, if the map of the sky is not complete, then the average over which the power spectrum is taken will contain discontinuities, and not be a complete Gaussian set. Therefore the error on \hat{C}_ℓ becomes correlated.

The Planck dataset will be a complete dataset, as it is increasingly possible, with new foreground subtraction methods Stolyarov *et al.* (2001) to remove the galactic foreground. However, we keep our approach as general as possible by including the effects of partial sky coverage in our modelling of the noise. We approximate this correlation by smearing with a Gaussian window function. As a result the noise we model is solely made up of Gaussian quantities.

$$\langle \hat{C}_\ell \rangle = 0 \quad (3.3)$$

The angle brackets now represent an average over the sky.

Turning briefly to Bayesian statistics, the probability of measuring a power spectrum, \hat{C}_ℓ , given true parameters $\{\theta_\alpha\}$, is

$$P(\theta_\alpha|\hat{C}_\ell) = \frac{P(\theta_\alpha, \hat{C}_\ell)}{P(\hat{C}_\ell)} \quad (3.4)$$

$$= \frac{P(\hat{C}_\ell|\theta_\alpha)P(\theta_\alpha)}{P(\hat{C}_\ell)}, \quad (3.5)$$

where commas inside the brackets of probability mean the probability of one *and* the other. The quantities $P(\theta_\alpha)$ are the *priors*, where any other information we may have about the values of the parameters can be included. However, the only quantity we need is the probability of the true cosmological parameters being $\{\theta_\alpha\}$ given a measured power spectrum \hat{C}_ℓ ,

$$P(\hat{C}_\ell|\theta_\alpha) \equiv \mathcal{L}(\hat{C}_\ell, \theta_\alpha). \quad (3.6)$$

$\mathcal{L}(\hat{C}_\ell, \theta_\alpha)$ is termed the *likelihood* and has no relation to the Lagrangian symbol of Section (1.2).

We wish to have the best unbiased estimator of the N true cosmological parameters. If the N parameters have true values $\{\theta_\beta^{\text{true}}\}$,

$$\langle \{\theta_\mu\}, \{\theta_\nu\}, \{\theta_\gamma\} \dots \rangle = \{\theta_\beta^{\text{true}}\}. \quad (3.7)$$

The average value on the left hand side is over all possible noise realisations.

Although the likelihood function, $\mathcal{L}(\hat{C}_\ell, \theta_\alpha)$, is nominally a function of the measure power spectrum, the power spectrum itself is a function of the parameters. The function \mathcal{L} is a function of the set of random variables $\{\theta_\alpha\}$.

The best unbiased estimator of the variables will have the smallest error on the variables. We wish to minimise

$$\Delta\theta_\alpha = (\langle \theta_\alpha^2 \rangle - \langle \theta_\alpha \rangle^2)^{\frac{1}{2}}. \quad (3.8)$$

The quantity most useful for finding the best unbiased estimates of $\{\theta_\alpha\}$ is the *Fisher information matrix*,

$$F_{\alpha\beta} \equiv - \left\langle \frac{\partial^2 \ln \mathcal{L}}{\partial \theta_\alpha \partial \theta_\beta} \right\rangle. \quad (3.9)$$

The error on a parameter, θ_α , if all other parameters are kept fixed, is related to the Fisher matrix as

$$\Delta\theta_\alpha \geq \frac{1}{\sqrt{F_{\alpha\alpha}}}. \quad (3.10)$$

This is the Cramér–Rao inequality. This gives us the lower limit on the error bar on the parameter estimate given that all other cosmological parameters influencing the data are known. If all the parameters are estimated from the data,

$$\Delta\theta_\alpha \geq (\mathbf{F}^{-1})_{\alpha\alpha}^{\frac{1}{2}}, \quad (3.11)$$

which exceeds the previous estimate in equation (3.10). The angle brackets in equation (3.9) represent an average over all possible noise realisations, and the quantity inside is the Hessian matrix, \mathbf{H} . In point of fact the parameters, and errors, will be measured from data with one specific noise realisation, and not the average over all possible Universes. So our errors will be better described with the above relations with \mathbf{H} replacing \mathbf{F} .

The brute force maximum likelihood method, which uses all the power spectrum data points, is the method of estimation which for a large dataset will provide the smallest errors. The likelihood for the N parameters, with the noise as we have modelled it, is

$$\mathcal{L}(\theta_\alpha) = \frac{1}{(2\pi)^{\frac{N}{2}} \sqrt{|\mathcal{N}|}} \exp \left\{ -\frac{1}{2} \sum_{\ell\ell'} \left[\hat{C}_\ell - C_\ell(\theta_\alpha) \right] \mathcal{N}_{\ell\ell'}^{-1}(\theta_\alpha) \left[\hat{C}_{\ell'} - C_{\ell'}(\theta_\alpha) \right] \right\}, \quad (3.12)$$

where \mathcal{N} is the noise covariance matrix,

$$\mathcal{N}_{\ell\ell'} = \langle n_\ell n_{\ell'} \rangle. \quad (3.13)$$

The average slope of \mathcal{L} is zero at the point corresponding to the true parameters.

The difficulty is that at each point in parameter space one generally computes the determinant of, and inverts, an $N \times N$ matrix. Since this scales as N^3 , it becomes a significant computational expense, even with $N \simeq 2000$. In this context, significant means that it exceeds the time to generate the theoretical power spectrum estimates.

3.2.2 MOPED

As a high-resolution, all sky, CMB dataset may contain ~ 2000 pieces of information, and we wish to determine about 10 cosmological parameters, there is then an amount of redundancy in the data, if it remains in this form. We can speed up the likelihood evaluation by using the MOPED method (Heavens *et al.*, 2000) to compress the N data in the measured \hat{C}_ℓ to one datum for each of M unknown parameters. I will outline the method of data compression for the case of a Gaussian likelihood, as introduced in HJL. MOPED is a way of making linear combinations of the data, which in certain circumstances loses no information about the parameters. The likelihood evaluation is speeded up by compressing N data in the measured \hat{C}_ℓ to one datum for each of M unknown parameters. It produces a set of weighting vectors \mathbf{b}^α ($\alpha = 1 \dots M$), from which a set of MOPED components $y_\alpha \equiv \mathbf{b}_\ell^\alpha \hat{C}_\ell$ is constructed. \mathbf{b}_ℓ^α refers to the ℓ component of the vector labelled by α . The MOPED vectors are designed to make the Fisher information matrix of equation (3.12) the same whether we use the compressed data y_α or the full set of power spectrum estimates. In fact this is only possible if we ignore the dependence of cosmic variance on the parameters. But we show that this restriction makes virtually no difference for a CMB dataset.

The Fisher matrix for a likelihood of the form of equation (3.12), a standard result (Vogele & Szalay, 1996; Tegmark *et al.*, 1997), is

$$F_{\alpha\beta} = \frac{1}{2} \text{Tr} \left(\mathcal{N}^{-1} \mathcal{N}_{,\alpha} \mathcal{N}^{-1} \mathcal{N}_{,\beta} + \mathcal{N}^{-1} (\mathbf{C}_{,\alpha} \mathbf{C}_{,\beta}^t + \mathbf{C}_{,\beta} \mathbf{C}_{,\alpha}^t) \right), \quad (3.14)$$

where \mathbf{C} represents the ℓ -component vector made up of the $C_{\ell s}$, the comma denotes a partial derivative with respect to a parameter, and t denotes a transpose vector.

The next step in the data compression requires the assumption that the dependence of the covariance matrix on the parameters can be ignored for the purpose of maximum likelihood parameter estimation. Only the results of the analysis can show how reasonable this assumption is.

If the data, C_ℓ , is dotted with an arbitrary set of vectors, \mathbf{b}^A , where $A = 1, 2, \dots, M$, then the compressed data,

$$y_A = \sum_{\ell=1}^N b_{\ell}^A \hat{C}_{\ell}, \quad (3.15)$$

will have mean and variance:

$$\langle y_A \rangle = \sum_{\ell=1}^N b_{\ell}^A C_{\ell} \quad (3.16)$$

$$\langle y_A y_B \rangle - \langle y_A \rangle \langle y_B \rangle = \sum_{\ell, \ell'=1}^N b_{\ell}^A \mathcal{N}_{\ell \ell'} b_{\ell'}^B. \quad (3.17)$$

We start by finding the optimum vector so that y_1 contains as much information as possible about θ_1 . Initially, we do this by assuming all others are known, but in fact the final results are more powerful than this assumption suggests. We maximise the Fisher matrix components F_{11} , given y_1 as the datum.

The information about parameter, θ_{α} , in the compressed datum corresponding to a vector \mathbf{b}^1 , in the specific case that all other parameters are known, is given by the $\tilde{F}_{\alpha\alpha}$ element of the new Fisher matrix. The form of the element follows from equation (3.14),

$$\tilde{F}_{\alpha\alpha} = \frac{1}{2} \left(\frac{\mathbf{b}^{1t} \frac{\partial \mathcal{N}}{\partial \theta_{\alpha}} \mathbf{b}^1}{\mathbf{b}^{1t} \mathcal{N} \mathbf{b}^1} \right)^2 + \frac{\left(\mathbf{b}^{1t} \frac{\partial \mathcal{C}}{\partial \theta_{\alpha}} \right)^2}{\left(\mathbf{b}^{1t} \mathcal{N} \mathbf{b}^1 \right)}, \quad (3.18)$$

but we are tackling the case where $\frac{\partial \mathcal{N}}{\partial \theta_{\alpha}} = 0$ for all the parameters. So the first term disappears. The denominators of the above expression are numerical factors, which can be incorporated into \mathbf{b}^1 without changing the Fisher matrix, and therefore the information content. Therefore, it is possible to solve for \mathbf{b}^1 such that

$$\mathbf{b}^{1t} \mathcal{N} \mathbf{b}^1 = 1. \quad (3.19)$$

If we now make the direct connection that we require the vector \mathbf{b}^1 to weight the dataset so as to provide the greatest information about θ_1 , then we need to maximise the Fisher matrix to give

$$\sum_{\ell \ell'} \frac{\partial}{\partial b_{\ell}^1} \left(b_{\ell'}^1 \frac{\partial C_{\ell'}}{\partial \theta_1} b_{\ell''}^1 \frac{\partial C_{\ell''}}{\partial \theta_1} - \lambda b_{\ell'}^1 \mathcal{N}_{\ell' \ell''} b_{\ell''}^1 \right) = 0, \quad (3.20)$$

where λ is a Lagrange multiplier, which allows the constraint of equation (3.19) to be incorporated.

The solution for \mathbf{b}^1 is

$$\mathbf{b}^1 = \frac{\mathcal{N}^{-1} \frac{\partial \mathcal{C}}{\partial \theta_1}}{\sqrt{\frac{\partial \mathcal{C}^t}{\partial \theta_1} \mathcal{N}^{-1} \frac{\partial \mathcal{C}}{\partial \theta_1}}}. \quad (3.21)$$

The denominator is a numerical factor again. The numerator makes instinctive sense. There is the \mathcal{N}^{-1} , showing the compressed data to be weighted inversely proportionally to noise, and there is the factor proportional to the sensitivity to the parameter, $\frac{\partial \mathcal{C}_\ell}{\partial \theta_1}$.

For the case where more than one parameter is to be estimated from the data, the analysis proceeds by finding y_2 uncorrelated with y_1 (i.e. $\langle y_1 y_2 \rangle - \langle y_1 \rangle \langle y_2 \rangle = 0$), and which contains as much information as possible about θ_2 (i.e. we maximise F_{22} subject to these constraints). Each parameter to be evaluated will thus add another Lagrange multiplier. This leads to the form of the vector \mathbf{b}^α , which maximises information about parameter θ_α :

$$b_\ell^\alpha = \frac{\sum_{\ell'} \left[\mathcal{N}_{\ell\ell'}^{-1} \frac{\partial \mathcal{C}_{\ell'}}{\partial \theta_\alpha} - \sum_{\beta=1}^{\alpha-1} \frac{\partial \mathcal{C}_{\ell'}}{\partial \theta_\alpha} b_{\ell'}^\beta b_\ell^\beta \right]}{\sqrt{\sum_{\ell'\ell''} \left(\frac{\partial \mathcal{C}_{\ell'}}{\partial \theta_\alpha} \mathcal{N}_{\ell'\ell''}^{-1} \frac{\partial \mathcal{C}_{\ell''}}{\partial \theta_\alpha} \right) - \sum_{\beta=1}^{\alpha-1} \left(\sum_{\ell'} \frac{\partial \mathcal{C}_{\ell'}}{\partial \theta_\alpha} b_{\ell'}^\beta \right)^2}} \quad (3.22)$$

Note that the MOPED vectors depend on the order in which the parameters are listed: \mathbf{b}_1 contains as much information about parameter 1 as possible. This vector also constrains parameter 2 to some extent; \mathbf{b}_2 adds as much information as possible about parameter 2 (which is not already constrained in y_1), etc.

3.3 Testing the MOPED method

We generated a grid of CMBFAST theoretical power spectra by varying three quantities; Ω_Λ from 0.66 to 0.76, in steps of 0.002; H_0 varying from 60 to 70 $\text{kms}^{-1}\text{Mpc}^{-1}$ in steps of 0.2 $\text{kms}^{-1}\text{Mpc}^{-1}$; and Ω_{CDM} from 0.246 to 0.256, in steps of 0.002. All other quantities are fixed. The values are not particularly important, but are listed here: $\Omega_B = 0.05$; scalar spectral index $n = 1$; no tensor modes; no massive neutrinos; 3 massless neutrinos. These are our $\mathcal{C}_\ell(\{\theta_\alpha\})$. We also require a dataset from which to estimate the parameters. We take the

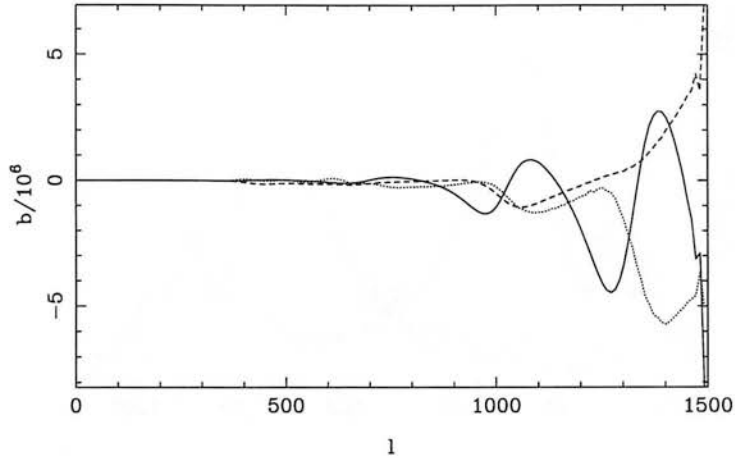


Figure 3.1: Optimised MOPED weighting vectors for a fiducial model with $H_0 = 65 \text{ km s}^{-1}\text{Mpc}^{-1}$, $\Omega_{\text{CDM}} = 0.254$ and $\Omega_\Lambda = 0.7$. The parameter ordering (see text) is Ω_Λ , H_0 and Ω_{CDM} . The MOPED vectors will depend on the choice of order for a particular noise realisation. The effect this has on the contours of the likelihood plot is only pronounced for a small number of multipole values ~ 30 .

simulated spectrum with parameter values $H_0 = 65 \text{ km s}^{-1}\text{Mpc}^{-1}$, $\Omega_\Lambda = 0.7$ and $\Omega_{\text{CDM}} = 0.254$, and add Gaussian noise at the level of cosmic variance, equation (3.2),

$$\frac{2C_\ell^2}{(2\ell + 1)},$$

as discussed in Section 3.2.1.

The power spectrum is convolved with a Gaussian of chosen width $\Delta\ell = 5$, to mimic approximately the correlations in power spectrum estimates introduced by partial sky coverage. The dataset consisted of the power spectrum sampled in even steps in ℓ . The unconvolved power spectrum is shown in Fig. 3.2, and the convolved spectrum in Fig. 3.3.

A set of 3 MOPED vectors is illustrated in Fig. 3.1, corresponding to vacuum energy density, Hubble constant and cold dark matter (CDM) density. These vectors would ensure, under certain assumptions, that the MOPED components y_α are uncorrelated, and of unit variance, so the likelihood with these as the data is simply

$$\mathcal{L}(\theta_\alpha) = \frac{1}{(2\pi)^{3/2}} \exp \left[-\frac{1}{2} \sum_{i=1}^3 (y_i - \langle y_i \rangle)^2 \right] \quad (3.23)$$

where the $\langle y_i \rangle$ are computed from the noise-free (but smoothed) theoretical power

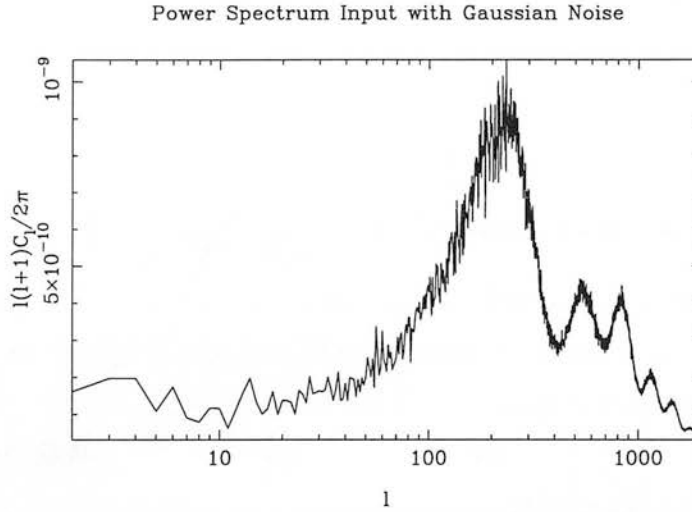


Figure 3.2: Simulated realisation of the CMB power used in the analysis.

spectra. Importantly, and remarkably, they ensure that the Fisher matrix for the compressed dataset $\{y_\alpha\}$ is the same as for the entire set of power spectrum estimates (see Heavens *et al.*, 2000, for proof). The marginal error on a single parameter is $[(F^{-1})_{\alpha\alpha}]^{\frac{1}{2}}$ and the error on the parameter estimated using any method cannot be smaller than this (see e.g. Kendall & Stuart, 1969; Tegmark *et al.*, 1997). Thus, by ensuring that the Fisher matrices coincide, the compression method can be described as locally lossless - the parameter errors, as estimated from the local curvature of the likelihood surface at the peak, are on average no larger for the compressed data than for the full set of power spectrum estimates.

In detail, the assumptions required for locally lossless compression do not hold for this analysis. In order to calculate the MOPED vectors, the data covariance matrix, and the derivatives of the power spectrum with respect to the parameters, need to be known. These are fixed by assuming a fiducial set of parameters. We show below that this fiducial set is not important, but one can iterate the process if desired, at minimal extra computational expense. Our results show that iteration is actually unnecessary. The second assumption is that the covariance matrix of the data is not dependent on the model parameters. This is not strictly true for the CMB power spectrum, as the noise includes a cosmic variance term which is dependent on the cosmology. However, this does not prevent us compressing the data, and, in fact the Fisher matrix is dominated by the sensitivity of the power spectrum itself to the parameters, rather than the sensitivity of the noise.

We calculate the full (equation 3.12) and compressed (equation 3.23) likelihoods,

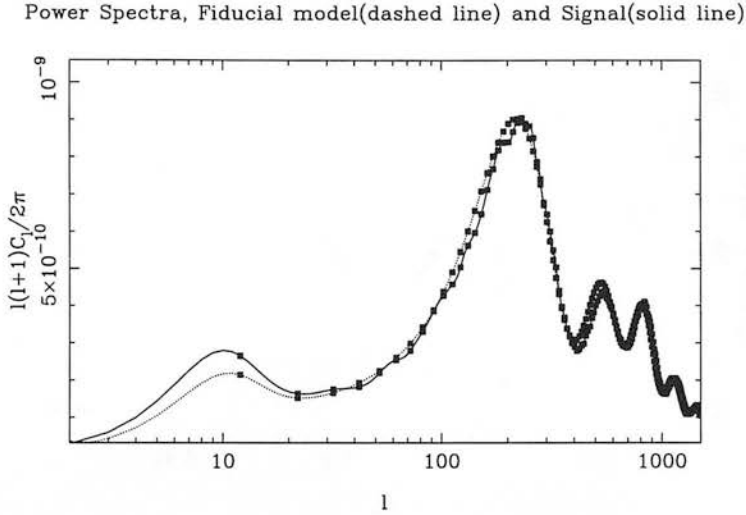


Figure 3.3: The true model spectrum (solid), with $H_0 = 65 \text{ kms}^{-1}\text{Mpc}^{-1}$, $\Omega_\Lambda = 0.7$ and $\Omega_{\text{CDM}} = 0.254$, with Gaussian noise and smoothed in ℓ with a Gaussian of width $\Delta\ell = 5$. Also shown (dotted) is the fiducial model used in the data compression for Fig.3.6: $H_0 = 60.8 \text{ kms}^{-1}\text{Mpc}^{-1}$, $\Omega_\Lambda = 0.732$ and $\Omega_{\text{CDM}} = 0.254$, both smoothed with a Gaussian of width $\Delta\ell = 5$. The boxes show the data points used for the likelihood calculations.

varying the calculation in the following ways:

- We mimic the effects of partial sky coverage by convolving the power spectrum with a Gaussian window function of various widths.
- The size of the dataset N is varied by changing the upper multipole limit of the available data, or by missing out some C_ℓ values.
- We explore different fiducial models, to see if the method is sensitive to an accurate initial guess of the parameters.

We fix most of the cosmological parameters. The parameters we allow to vary are the vacuum energy density parameter Ω_Λ , the CDM density parameter Ω_{CDM} and the Hubble constant H_0 , although, for display purposes we plot a fixed Ω_{CDM} slice, the $\Omega_\Lambda - H_0$ plane.

3.4 Results

Figure 3.4 shows the $H_0 - \Omega_\Lambda$ likelihood surface using the power spectrum of Figure 3.2 up to $\ell = 1500$ in steps of 10. The power estimates were smoothed with a Gaussian of width 5. The calculation of this grid of likelihoods took 9420

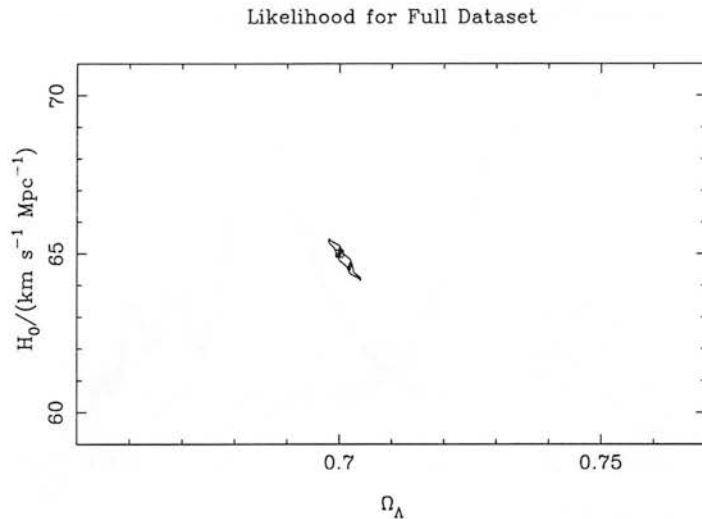


Figure 3.4: Likelihood surface for Ω_Λ and H_0 obtained from the the full dataset. This dataset consists of 150 power spectrum estimates from $\ell = 2, \dots, 1500$ in steps of 10, smoothed over a scale of $\Delta\ell = 5$. The true model is labelled with a square .

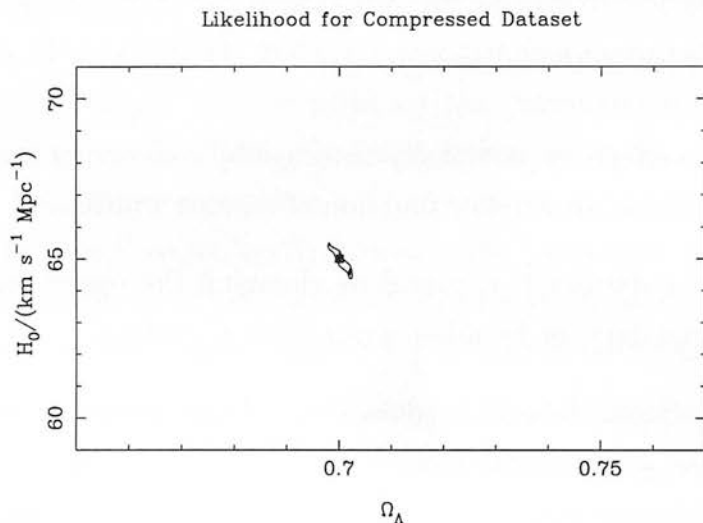


Figure 3.5: Likelihood surface for Ω_Λ and H_0 obtained from the the 3 MOPED components. The fiducial model used for the data compression coincides with the true model in this case, and both are marked by a square. The likelihood contours are too small to see individually for this experiment; the outer contour contains 99.99% of the probability, assuming uniform priors.

seconds of CPU on an alpha workstation. Figure 3.5 shows the likelihood using 3 MOPED components as compressed data. The fiducial model, used to calculate the weighting vectors, is the same as the true model in this case.

Fig. 3.6 shows the effect of choosing an incorrect fiducial model ($H_0 = 60.8$ $\text{kms}^{-1}\text{Mpc}^{-1}$, $\Omega_\Lambda = 0.732$, $\Omega_{\text{CDM}} = 0.254$). The true solution is still recovered accurately, but much faster: 0.00098 seconds, or an improvement of order 10^7 .

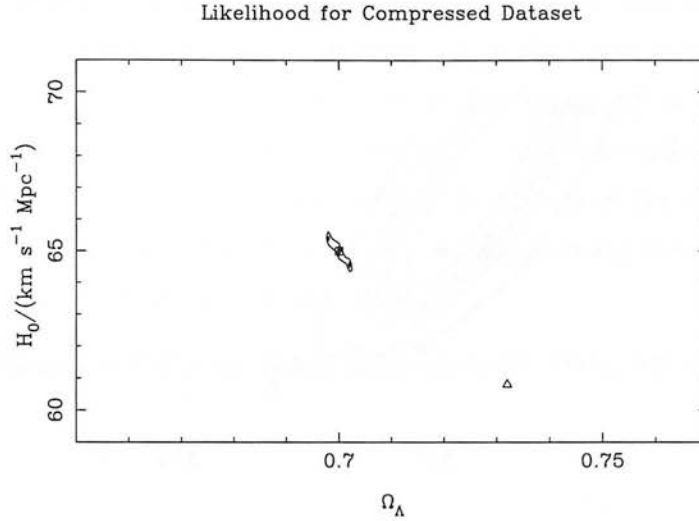


Figure 3.6: Likelihood surface for Ω_Λ and H_0 obtained from the the 3 MOPED components. The fiducial model used for the data compression no longer coincides with the true model, and is marked by a triangle. Note that the method still recovers the correct model (square).

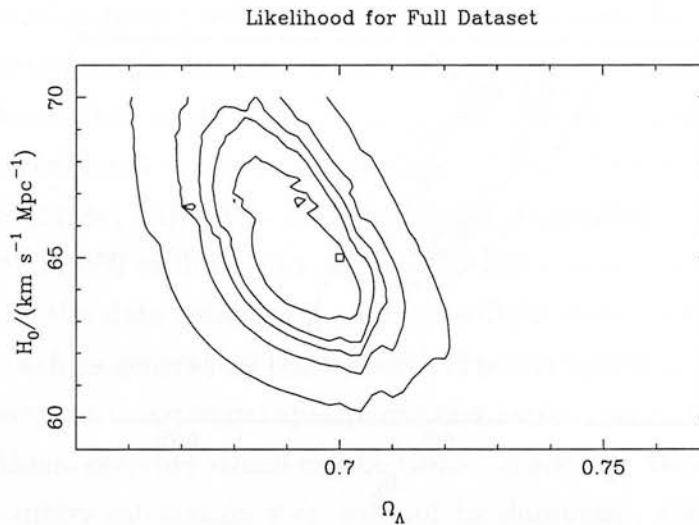


Figure 3.7: Likelihood from the full power spectrum, as in Fig. 3.4, but restricted to $\ell \leq 300$ in steps of 10, to illustrate the size of the error bars. The contours represent confidence limits of 99.99%, 99%, 95.4%, 90%, and 68%. The true model is labelled with a square.

Figures 3.4, 3.5 and 3.6 look a little odd, showing very small and indistinguishable contours in very large slices of parameter space. However they are making an important point. They show MOPEDs ability to sweep large areas of parameter space and locate the likelihood peak, a time- and CPU- saving process, so that the full dataset may be used within a reduced volume of parameter space to determine the parameters as accurately as possible using all the information available.

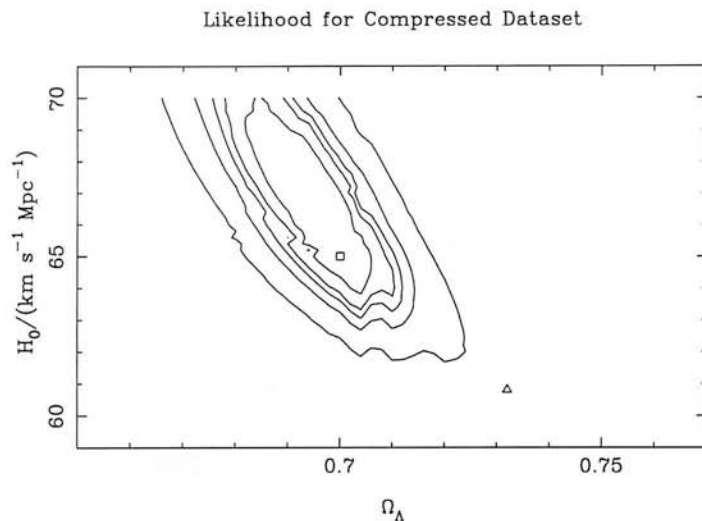


Figure 3.8: As Fig. 3.7, but showing the likelihood from MOPED components. Note that the error bars are comparable.

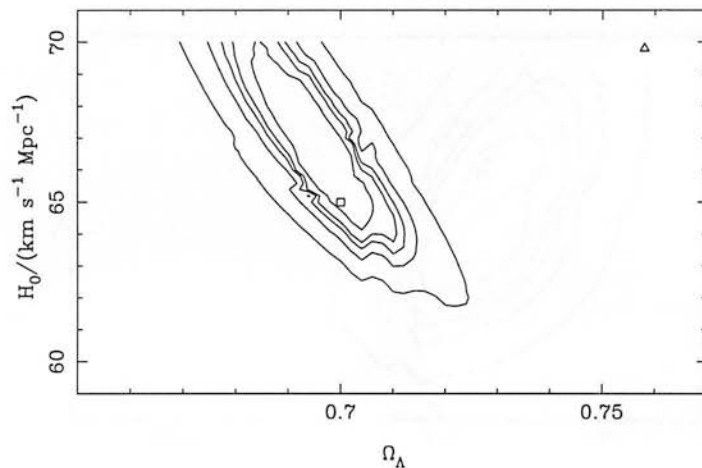


Figure 3.9: Showing the likelihood, as Fig. 3.7, but with a different fiducial model and MOPED components from Fig. 3.8.

For the MOPED data compression method to work to reduce the areas of parameter space over which the full dataset needs to be used the *spread* of the likelihood peak must be well estimated by the compressed dataset. Now, by decreasing the amount of data used in the analysis to only power spectrum values up to multipole 300, in steps of 10, we obtain more visible errorbars for the purpose of illustration. The method is designed to ensure that the error bars should be almost the same as the full likelihood on average, and we see that for this realisation the errors are comparable to an extent, (Fig. 3.7, 3.8 and 3.9), but there is a change

in the shape of the likelihood peak. This is likely to be due to the fact that the noise is not independent of the parameters, as in the ideal case for the success of this method, but dependent upon the power spectrum, $\sigma_\ell^2 = 2C_\ell^2/(2\ell + 1)$. The power spectrum up to 300ℓ contains only the first peak and most of the cosmic variance contribution, and these both effect the ability of the compressed dataset to reproduce the likelihood surface given the degeneracy between the effects of Ω_Λ and H_0 , as discussed in Section 1.3.

The full likelihood calculation takes 5960 seconds, while MOPED takes 0.00016 seconds.

3.5 Conclusions

We have shown that the MOPED data compression algorithm can speed up parameter estimation from CMB data by very large factors. For N correlated data points, a brute-force likelihood evaluation using all the data will scale as N^3 . MOPED reduces this to M approximately uncorrelated, unit variance components, whose likelihood evaluation scales with the number of parameters M . For a Planck-size dataset with $N = 2000$ and ~ 12 parameters, the speed-up factor should be around 500 million. In a sense MOPED is much more powerful than it needs to be, as the data processing element will be dominated by other steps in the pipeline, such as generating the theoretical power spectrum for a given parameter set. However, having very rapid parameter estimation is useful, especially in multi-dimensional searches which can be time-consuming. We can be certain now that the parameter estimation step will not be dominant, even if CMBFAST or variants are accelerated by orders of magnitude. For current experiments, data compression is not necessary, as there are relatively few band-power estimates available. For future experiments such as Planck, the fast likelihood evaluation makes it more attractive to build up libraries of theoretical power spectra (or MOPED components, if storage space is an issue, as the compression is a factor > 100).

There are two qualifications in this analysis. Bond *et al.* (1998) have argued that the correlated noise distribution resulting from an incomplete sky map would be closer to an offset lognormal. This has not been our approach, but the same noise modelling was used for the full and compressed datasets, and this chapter

concentrates on the compression of data. The second qualification is that it could be argued that the MOPED is not required for the satellite CMB datasets at all. This might be argued because the parameter estimation consists of two stages: firstly generating simulated spectra across parameter space, using Boltzmann codes such as CMBFAST, and secondly running the likelihood analysis. The time taken to generate the simulated power spectra using CMBFAST is the more time-consuming of the two stages in the process. There has been work done, however, to speed up this generation of theoretical spectra: Tegmark *et al.* (2001) have found a method of calculating $C_{\ell}s$, which improve on the speed of CMBFAST by a factor of 10^3 . The time taken to generate the theoretical spectra is unlikely to hinder the ultimate data analysis. In addition, the Planck Surveyor satellite is not due to be launched for five years, and the large scale generation and storage of these spectra, primarily to test early Universe model analysis methods, has already begun. The likelihood calculations cannot be done until we have the data in our hands, therefore the MOPED algorithm applied to CMB data will be of real benefit.

Chapter 4

The Warm Inflation Bispectrum

The analysis of the cosmic microwave background for cosmological parameter estimation has been largely confined to a single popular early Universe model. As a primary step in widening the early Universe models considered for data analysis, my third project has been an investigation of the CMB properties of the Warm Inflation model (Berera, 1995, 1996). Taking into account second order effects in the generation of scalar field fluctuations, small deviations from Gaussianity have been predicted for standard inflation (Gangui *et al.*, 1994; Barrow & Coles, 1990; Yi & Vishniac, 1993; Salopek & Bond, 1990; Kofman *et al.*, 1994). Arjun Berera, Alan Heavens, Sabino Matarrese and I have calculated the prediction of non-Gaussianity for the warm inflation model, to find if it is comparable, or rather, distinguishable, from the non-Gaussianity predicted for the standard ‘supercooled’ inflation scenario. The expanding opportunity to distinguish non-Gaussian signatures with new cosmic microwave background experiments warrants calculating comparative estimates of non-Gaussianity with alternative early Universe models.

The form of the CMB power spectrum for the warm inflation model in the case of strong dissipation has been predicted (Taylor & Berera, 2000). There has been no previous calculation of the non-Gaussianity which may be expected for warm inflation.

4.1 Predictions of Non-Gaussianity for Standard Inflation

The popular early Universe models, based on slow-roll inflation occurring in a pure vacuum energy epoch, and ending in reheating and thermalization, are termed henceforth ‘supercooled’ inflation. These models make the assumption either that there is no radiation present during inflation, or that whatever radiation may have been present is rapidly redshifted away and there is no radiation present during the expansion phase.

I shall begin with a review of the calculation of the supercooled inflaton bispectrum in the Astrophys. J. Gangui *et al.* paper of 1994, where the calculations were restricted to single-field models. In their paper a stochastic approach was applied, as introduced by Starobinsky in ‘Field Theory, Quantum Gravity, and Strings’ (1986). The stochastic equations modelling the dynamics of the inflaton separate the inflaton into a background field and the quantum fluctuation components. The background field is ‘coarse grained’, which means averaged over regions larger than scales of cosmological interest.

The first step in describing the dynamics of the inflaton field is the introduction of the time variable $\alpha \equiv \ln(a/a_*)$, where a_* represents the scale factor at the beginning of inflation. This bypasses an uncertainty in the local Hubble parameter translating into an uncertainty in the definition of the time variable.

The basic evolution equation of the background field of Gangui *et al.* is

$$3H\dot{\phi}_{\text{cl}} + V'(\phi_{\text{cl}}) = 0, \quad (4.1)$$

where the coarse-grained averaged field is represented by ϕ_{cl} and the time variable of equation (1.77) is replaced by α . $\alpha = 0$ corresponds the beginning of inflation. Noting that

$$\frac{d\alpha}{dt} = H, \quad (4.2)$$

it follows that

$$H \frac{d\phi_{\text{cl}}}{d\alpha} = -\frac{V'(\phi_{\text{cl}})}{3H}. \quad (4.3)$$

Recall also, from equation(1.79), $\rho = V$ during inflation. Using this to substitute H in equation (4.3)

$$\frac{d\phi_{\text{cl}}}{d\alpha} = -\frac{m_{\text{pl}}^2}{8\pi} \times \frac{V'(\phi_{\text{cl}})}{V(\phi_{\text{cl}})}. \quad (4.4)$$

In stochastic inflation, the quantum fluctuations are modelled in the equation of motion by adding a zero-mean Gaussian noise term, $\eta(\mathbf{x}, \alpha)$, with amplitude fixed at horizon crossing by normalization from the 1991 COBE CMB satellite data (Smoot *et al.*, 1991; Bunn *et al.*, 1996). Thus the treatment of fluctuations in Gangui *et al.* begins with the stochastic inflation evolution equation

$$\frac{\partial \phi(\mathbf{x}, \alpha)}{\partial \alpha} = -\frac{m_{\text{pl}}^2}{8\pi} \frac{V'(\phi)}{V(\phi)} + \frac{H(\phi)}{2\pi} \eta(\mathbf{x}, \alpha). \quad (4.5)$$

Here η has autocorrelation function (Gangui *et al.*, 1994; Mollerach *et al.*, 1991)

$$\langle \eta(\mathbf{x}, \alpha) \eta(\mathbf{x}', \alpha') \rangle = \hbar j_0[q_s |\mathbf{x} - \mathbf{x}'|] \delta(\alpha - \alpha'), \quad (4.6)$$

where j_0 is a spherical Bessel function and q_s is the comoving wavenumber which defines the coarse-grain size. It may be surprising that the correlation function is represented with a delta-function in time; if this were true it would mean that any part of the wave of fluctuation exiting the horizon is uncorrelated with the part of the wave which exits the horizon just before or just after it. Gangui *et al.* use this simplified form for a correlation function for the fluctuations, and we will later quote a similar form for the warm inflation perturbations, though as will become clear, our calculation differs from the Gangui *et al.* bispectrum calculation due to the different mechanism of freeze-out of thermal fluctuations. We do not include this correlation relation in the calculation of the bispectrum, which we carry out by writing the first-order scalar field fluctuations in terms of the thermal fluctuations, and represent the correlations in terms of the scalar field power spectrum at horizon exit.

The quantum-to-classical transition at horizon-crossing needs to be incorporated into the Fourier transform.

$$\delta\phi(\mathbf{x}, \alpha) = \phi(\mathbf{x}, \alpha) - \phi_{\text{cl}}(\alpha) \quad (4.7)$$

$$\delta\phi(\mathbf{x}, \alpha(q_s)) = \left(\frac{1}{2\pi}\right)^3 \int d^3k \delta\phi(\mathbf{k}) \Theta(q_s - k) e^{i\mathbf{k}\cdot\mathbf{x}}, \quad (4.8)$$

where Θ is the Heaviside function. Thus the Fourier transform of equation (4.8) needs to be $\delta\phi(\mathbf{k}, \alpha(q_s)) = \delta\phi(\mathbf{k}) \Theta(q_s - k)$. Observe, in the limit $k \rightarrow q_s^-$, which corresponds to horizon crossing, $\delta\phi(\mathbf{k}, \alpha(k))$ becomes $\delta\phi(\mathbf{k})$.

The relation between the scalar field fluctuation at horizon exit and the resulting peculiar (*peculiar* describing any quantity outwith a homogeneous background

value) gravitational potential, Φ , has the simple form (Bardeen *et al.*, 1983)

$$\Phi(\mathbf{k}) = -\frac{3}{5} \frac{H}{\dot{\phi}} \delta\phi(\mathbf{k}). \quad (4.9)$$

which can be explained as follows: the gravitational fluctuation is related to the density field fluctuation at horizon exit. The peculiar gravitational potential for the scales we are interested in will result from the density perturbation which exits the horizon during inflation as $\Phi \sim \delta\rho/(\rho+p)$. During inflation $\rho_\phi \simeq V$ and $\rho_\phi + p_\phi \simeq \dot{\phi}^2$ (derived in Section 1.2, equations (1.69) and (1.70)). So

$$\frac{\delta\rho}{(\rho+p)} \simeq \frac{V'(\phi)\delta\phi}{\dot{\phi}^2} \simeq \left(\frac{H}{\dot{\phi}}\right) \delta\phi, \quad (4.10)$$

where in the last relation the slow-roll equation of motion, equation (4.1), is used.

As discussed in Section 1.2, the frozen-in inflaton fluctuations are Gaussian to first order – thus with a bispectrum equal to zero. However when one expands the bispectrum to second order in the fluctuations it leads to non-Gaussian effects. Gangui *et al.* (1994) found this expression for the lowest order non-vanishing contribution to the gravitational potential

$$\begin{aligned} \langle \Phi(\mathbf{k}_1)\Phi(\mathbf{k}_2)\Phi(\mathbf{k}_3) \rangle &= \left(\frac{24\pi}{5m_{\text{pl}}}\right)^3 (2\pi)^3 \delta_D^3(\mathbf{k}_1 + \mathbf{k}_2 + \mathbf{k}_3) \frac{P(k_2)}{X^2(k_2)} \frac{P(k_3)}{X^2(k_3)} \\ &\times \left[\frac{X^2(k_2)\Theta(k_2 - k_3) + X^2(k_3)\Theta(k_3 - k_2)}{2m_{\text{pl}}} - \frac{2X'(k_1)X(k_2)X(k_3)}{X^2(k_1)} \right. \\ &\quad \left. + 2 \int_{k_*}^{k_1} \frac{dq'}{q'} B(q')X(q') \right] + (\mathbf{k}_1 \leftrightarrow \mathbf{k}_2) + (\mathbf{k}_1 \leftrightarrow \mathbf{k}_3), \quad (4.11) \end{aligned}$$

where

$$X[\alpha(k)] \equiv m_{\text{pl}} \frac{V'(\phi_{\text{cl}})}{V(\phi_{\text{cl}})}. \quad (4.12)$$

Gangui *et al.* used this result to calculate the value of the CMB *skewness*, C_3 , for various inflationary potentials,

$$C_3 = \int \frac{d\Omega_\gamma}{4\pi} \left[\frac{\Delta T(\gamma)}{T} \right]^3, \quad (4.13)$$

where the integral is over the sphere of the sky, and γ represents a direction vector specifying the positions of the temperature fluctuations on the sky. They calculate this quantity by first calculating $B(k, k, k)$, the gravitational bispectrum value for the case where the three wavevectors are equal. They found the values

for skewness for the bulk of their single field models to be considerably smaller in magnitude than that resulting from the cosmic variance corresponding to that model. However the skewness is not particularly sensitive as a statistic for testing for non-Gaussianity, having only a single degree of freedom.

Warm inflation differs from the standard, supercooled picture of inflationary cosmology in that the process of radiation production becomes an important constituent of the theory. In particular, during warm inflation, radiation production occurs concurrently with inflationary expansion and the production of density fluctuations is influenced by thermal effects. The production of radiation throughout inflation implies reheating becomes unnecessary. This avoids the complications specific to reheating, such as problems due to parametric amplification, in the supercooled inflation model, while still solving the cosmological problems of horizon, flatness and density perturbations, in the same way as supercooled inflation does.

One difference between warm inflation dynamics and supercooled inflation dynamics is that, in the former, everything is classical, both the background and the fluctuation, whereas in the latter the background is classical and the fluctuations are quantum. Therefore, in the warm inflation part of my analysis I cannot preserve the Gangui *et al.* notation of ϕ_{cl} representing the coarse-grained background field. ϕ_{cl} represents the background and fluctuations for warm inflation. So from now on I will label the the coarse-grain average inflaton value ϕ_0 .

4.2 The Statistics of a Warm Inflation Generated Perturbation Spectrum

In this section I shall present our predictions of the form of the fluctuations and quantify the non-Gaussianity, using the bispectrum as a measure, for the supercooled and warm inflation scenarios.

4.2.1 Warm Inflation Dynamics

The basic evolution equation for inflationary dynamics has the same general form as the inflation set-up discussed in Section 1.2,

$$\ddot{\phi} + 3H\dot{\phi} + \Gamma\dot{\phi} + V'(\phi) = 0, \quad (4.14)$$

where $H = \dot{a}/a$ is the Hubble parameter, and a is the cosmic expansion factor, with inflation taking place on a flat, or nearly flat non-zero potential. When the slow roll conditions are satisfied $\ddot{\phi}$ is negligible in comparison to the other terms. In the case of supercooled inflation $\Gamma\dot{\phi}$, the dissipation term, does not kick in until during reheating.

In contrast, for the warm inflation picture, the dissipation term is not zero during inflation. This implies that inflation occurs in the presence of a thermal component (Berera, 1995, 1996).

In this section I shall review warm inflation dynamics. If we look at the stress energy conservation equation for a Friedmann universe (obtained from the two independent relations in the Einstein equations, $G_{\mu\nu} = 8\pi GT_{\mu\nu}$) for the case where the Universe consists of a radiation and a vacuum energy component,

$$\dot{\rho}_r(t) = -4\rho_r(t)H - \dot{\rho}_v(t). \quad (4.15)$$

Were there no dissipation, i.e. no source term, the radiation component would be shifted rapidly away as $\rho_r \sim e^{-4Ht}$. However, there is ‘new’ radiation coming from the conversion of the potential energy of the scalar field. This dissipative process in turn reacts back on the inflaton by slowing its ‘roll’ down the potential.

Although other scenarios are possible, we are interested here in the limiting case of strong dissipation, $\Gamma \gg (\dot{a}/a)$ and $\Gamma|\dot{\phi}| \gg |\ddot{\phi}|$. The resulting equation averaged over a Hubble volume has a form similar to the familiar slow-roll equation of motion of supercooled inflation,

$$\frac{d\phi}{dt} = -\frac{1}{\Gamma} \frac{dV(\phi)}{d\phi}. \quad (4.16)$$

Except the vital difference, here, is that the so-called Hubble friction term has been replaced with a true friction term, the dissipation. The presence of the above dissipation term implies that $\dot{\rho}_v(t) \neq 0$ in equation (4.16). As such this causes a continuous production of radiation during inflation corresponding to vacuum energy decay and at the end of inflation the regime passes smoothly into radiation domination (Berera, 1997). During inflation the strong dissipation condition is further defined by the relations $\dot{\rho}_r \sim 0$, $4\rho_r H \sim \dot{\rho}_v$. When calculating quantitative predictions for the bispectrum we will need values for the dissipation. For a given scalar field potential, and restrictions placed on the fluctuation amplitude from

the COBE data, we will evaluate the necessary dissipation such that $\dot{\rho}_r \sim 0$ for the potential.

How does the presence of this constant radiation component affect the dynamics of the inflaton?

Above we have considered the equation of motion for the zero mode of the inflaton. Due to the presence of radiation during inflation its interaction with the inflaton will induce thermal fluctuations in this field.

As a phenomenological representation of these dynamics we can consider small deviations about the equilibrium state.

The simplest phenomenological model is in the regime of small fluctuations, in which case we can use the *fluctuation dissipation theorem* (see Reif, 1965, Chapter 15). Under these assumptions, the evolution equation for the inflaton field fluctuations $\delta\phi(\mathbf{x}, t)$ is obtained by taking the linearized deviation in equation (4.14) and adding a Gaussian noise term $\eta(\mathbf{x}, t)$ to the right hand side. Starting from an equation of motion

$$\frac{d^2\phi(\mathbf{x}, t)}{dt^2} - \nabla^2\phi(\mathbf{x}, t) + (3H + \Gamma)\frac{d\phi(\mathbf{x}, t)}{dt} + V'(\phi_0(t)) = \eta(\mathbf{x}, t), \quad (4.17)$$

where

$$\phi(\mathbf{x}, t) = \phi_0(t) + \delta\phi(\mathbf{x}, t). \quad (4.18)$$

The second term on the left hand side of equation (4.17) is re-introduced due to the small-scale inhomogeneity resulting from the thermal fluctuations. Due to our strong dissipative conditions we eliminate $\delta\ddot{\phi}$ and $3H$. This gives us

$$\frac{d\delta\phi(\mathbf{x}, t)}{dt} = \frac{1}{\Gamma} [\nabla^2\delta\phi(\mathbf{x}, t) - V''(\phi_0(t))\delta\phi(\mathbf{x}, t) + \eta(\mathbf{x}, t)]. \quad (4.19)$$

If the above equation is smoothed over a scale larger than the Hubble radius size, equation (4.16) is recovered. The Gaussian force function, $\eta(\mathbf{x}, t)$, which the equation of motion has gained represents the thermal fluctuations resulting from what is analogous to a heat bath in a system in thermal physics, so that

$$\langle\eta\rangle = 0, \quad (4.20)$$

$$\langle \eta(\mathbf{k}, t) \eta(\mathbf{k}', t') \rangle = 2\Gamma T (2\pi)^3 \delta^{(3)}(\mathbf{k} - \mathbf{k}') \delta(t - t') \quad (4.21)$$

The equation of motion, equation (4.14), includes a dissipation term which I introduced in Section 1.2. This is a *Langevin-type* equation, so called because it is exactly similar to the Langevin equation which models the Brownian motion of particles in a heat bath (Appendix K). Although we are using these equations phenomenologically, they have been obtained from first principles quantum field theoretic calculations for certain warm inflation models. There are a set possibilities for how the dissipation of scalar field energy can occur. In the first example Berera (1996) obtained equations like those above with a simple quantum mechanical toy model. In the quantum field theory case, these equations were arrived at in Berera *et al.* (1999, 1998); Yokoyama & Linde (1999); Berera (2000); Berera & Ramos (2001). In one particular model (Berera *et al.*, 1999; Berera & Kephart, 1999a,b; Berera, 2000), a Lagrangian is considered with a scalar inflaton field ϕ interacting with $N_M \times N_\chi$ scalar fields χ_{ik} and $N_M \times N_\Psi$ fermion fields Ψ_{ik} . The Lagrangian contains an inflaton self-interaction term of the form $\frac{\lambda}{4!} \phi^4$, and a similar series of self-interaction terms of the other scalar fields $\sum_i \frac{f_i}{4!} \chi_i^4$. Then there are interaction terms for the inflaton with other scalar fields of the form

$$\sum_{ik} \frac{g_{ik}^2}{2} (\phi - M_i)^2 \chi_{ik}^2 \quad (4.22)$$

and with the fermion fields of the form

$$\sum_{ik} h_{ik} (\phi - M_i) \bar{\Psi}_{ik} \Psi_{ik}, \quad (4.23)$$

where λ , f_i , g_{ik}^2 and h_{ik} are the couplings. M_i are mass scales which cover, in steps, the range of values of ϕ_0 over which warm inflation occurs.

In the first principles approach the time scales for thermalization have to be checked for self-consistency. This amounts to showing that the time-scale of all the microphysical process, which add up to energy production and thermalization, are much faster than all the characteristic macrophysical time scales, in particular the motion of the inflation field, $(\phi_0/\dot{\phi}_0)$, and the Hubble time, $(1/H)$, which corresponds to an efold of inflation. Berera *et al.* (1998, 1999); Berera (2000); Yokoyama & Linde (1999) examined these consistency conditions and showed regimes where the particle decay widths, corresponding to inflaton decay into

light particles, are bigger than the Hubble time and the motion of the zero-mode during inflation.

For structure formation, the vital difference between standard and warm inflation is that the fluctuations resulting in the latter are thermal and not quantum fluctuations.

An interesting part of this calculation is that it will show that warm inflation, which simultaneously induces fluctuations in the inflaton field and frictionally damps its motion, generates fluctuations which also undergo a transition where they cease to develop (except gravitationally), a ‘thermal freeze-out’, and this occurs *before* the fluctuation leaves the causal horizon.

4.2.2 The Warm Inflation Bispectrum

We will carry out a calculation of the warm inflation bispectrum, based on equation (4.19), up to second order in the fluctuation. This calculation will be formally similar to the calculation of Gangui *et al.* (1994) for supercooled inflation, reviewed in Section 4.1, where they used the stochastic approach. The fluctuations leading to structure formation from warm inflation are thermal, and not quantum, fluctuations. These thermal fluctuations, and equation (4.19), are classical at all times. In contrast to this, in the stochastic approach of Gangui *et al.* (1994) the classical limit is represented through the use of Heaviside functions, equation (4.8). Therefore, our warm inflation calculation is as follows: we expand $\phi(\mathbf{x}, t)$ in terms of the homogeneous, spatially averaged, ‘background’ field, which is dependent only on time, and the first-order and second-order fluctuations,

$$\delta\phi(\mathbf{x}, t) = \delta\phi_1(\mathbf{x}, t) + \delta\phi_2(\mathbf{x}, t), \quad (4.24)$$

where $\delta\phi_2 = \mathcal{O}(\delta\phi_1^2)$, and then take the Fourier transforms, finding

$$\frac{d}{dt}(\delta\phi_1(\mathbf{k}, t)) = \frac{1}{\Gamma}[-k^2\delta\phi_1(\mathbf{k}, t) - V''(\phi_0(t))\delta\phi_1(\mathbf{k}, t) + \eta(\mathbf{k}, t)] \quad (4.25)$$

$$\frac{d}{dt}(\delta\phi_2(\mathbf{k}, t)) = \frac{1}{\Gamma}[-k^2\delta\phi_2(\mathbf{k}, t) - V''(\phi_0(t))\delta\phi_2(\mathbf{k}, t) - \frac{1}{2}V'''(\phi_0(t)) \int d^3p \delta\phi_1(\mathbf{k} - \mathbf{p}, t)\delta\phi_1(\mathbf{p}, t)]. \quad (4.26)$$

The wavenumbers in the above equations represent physical and not comoving coordinates,

$$k_{\text{phys}} = k_{\text{com}} e^{Ht}. \quad (4.27)$$

The Universe needs to have undergone sixty e-folds of inflation to solve the horizon and flatness problems (Section 1.2, Appendix F). The time-dependence of the k -vectors could be a complicating effect, and in order to resolve this we carry out integrations of equations (4.25) and (4.26), over time, in steps of Hubble times, during each of which k is taken to be approximately constant.

The solutions to (4.25) and (4.26) which result are

$$\delta\phi_1(\mathbf{k}, t) = A(k, t) \int_{t_0}^t dt' \frac{\eta(\mathbf{k}, t')}{\Gamma} A(k, t')^{-1} + A(k, t) \delta\phi_{M1}(\mathbf{k}, t_0) \quad (4.28)$$

and

$$\delta\phi_2(\mathbf{k}, t) = A(k, t) \int_{t_0}^t dt' B(t') \left[\int \frac{dp^3}{(2\pi)^3} \delta\phi_1(\mathbf{p}, t') \delta\phi_1(\mathbf{k} - \mathbf{p}, t') \right] A(k, t')^{-1} + A(k, t) \delta\phi_{M2}(\mathbf{k}, t_0), \quad (4.29)$$

where

$$A(k, t) = \exp^{-\int_{t_0}^t \left(\frac{k^2}{\Gamma} + \frac{v''(\phi_0(t'))}{\Gamma} \right) dt'} \quad (4.30)$$

$$B(t) = -\frac{V'''(\phi_0(t))}{\Gamma}. \quad (4.31)$$

t_0 is the time of the beginning of the corresponding e-fold of inflation, and t and t' are time coordinates measured from t_0 .

The second term on the right hand side of each of these equations consists of a *memory* term, an integration constant representing the value of each of the fluctuations at the beginning of that particular e-fold of inflation, multiplied by the function $A(\mathbf{k}, t)$. This decreases over time as $A(\mathbf{k}, t)$ decreases with time. The first term on the right hand side of each of these equations is the thermalizing term. Looking back at equation (4.25), the first two terms on the right hand side are potential terms and the third term represents a driving oscillation. One sees

from looking at the first term that the damping becomes more effective for larger k . However if $\frac{k^2}{\Gamma}$ is sufficiently small a mode of oscillation will be inflated out of the horizon before it relaxes. There is a physical scale, k_F , where $\phi(k_F)$ freezes in. This is the point where the memory term becomes important in relation to the other term. The freeze-out wavenumber is defined at the point of equality in the relation

$$\frac{k^2 + V''(\phi_0)}{H\Gamma} > 1. \quad (4.32)$$

In general for warm inflation $V''(\phi_0) < \Gamma H$, so the above condition can be simplified to $k_F = \sqrt{\Gamma H}$.

Hereafter the scale k_F will be referred to as the freeze-out wavenumber. In supercooled inflation the freeze-out wavenumber would correspond to the Hubble scale, as the quantum fluctuation becomes classical on exiting the causal horizon. For warm inflation the fluctuations freeze in *before* horizon exit.

Wick's theorem states that correlation can be expanded in terms of sums of products of lower-order correlation functions and a residual, *connected*, part of the higher-order correlation, i.e. $\langle abcd \rangle = \langle abcd \rangle_c + \sum_{\text{perms}} \langle abc \rangle \langle d \rangle + \sum_{\text{perms}} \langle ab \rangle \langle cd \rangle + \langle a \rangle \langle b \rangle \langle c \rangle \langle d \rangle$, the c subscript labelling a connected correlation. The scalar field perturbations have mean zero, $\langle \delta\phi(\mathbf{k}, t) \rangle = 0$, and are Gaussian to first order, $\langle \delta\phi_1(\mathbf{k}_1, t) \delta\phi_1(\mathbf{k}_2, t) \delta\phi_1(\mathbf{k}_3, t) \rangle = 0$. Thus, the lowest order nonvanishing contribution to the inflaton bispectrum comes from the correlation of two first order perturbations with one second order perturbation, which can be expanded in terms of first order perturbations, equation (4.29),

$$\begin{aligned} \langle \delta\phi(\mathbf{k}_1, t) \delta\phi(\mathbf{k}_2, t) \delta\phi(\mathbf{k}_3, t) \rangle &= \langle (\delta\phi_1(\mathbf{k}_1, t) + \delta\phi_2(\mathbf{k}_1, t)) (\delta\phi_1(\mathbf{k}_2, t) + \delta\phi_2(\mathbf{k}_2, t)) \\ &\quad (\delta\phi_1(\mathbf{k}_3, t) + \delta\phi_2(\mathbf{k}_3, t)) \rangle \\ &\simeq \langle \delta\phi_1(\mathbf{k}_1, t) \delta\phi_1(\mathbf{k}_2, t) \delta\phi_2(\mathbf{k}_3, t) \rangle + \text{perms} \quad (4.33) \end{aligned}$$

$$\begin{aligned} &= A(k_3, t) \int_{t_0}^{t_3} A(k_3, t')^{-1} B(t') \left[\int \frac{d^3p}{(2\pi)^3} \langle \delta\phi_1(\mathbf{k}_1, t_1) \delta\phi_1(\mathbf{p}, t') \rangle \right. \\ &\quad \left. \langle \delta\phi_1(\mathbf{k}_2, t_2) \delta\phi_1(\mathbf{k}_3 - \mathbf{p}, t') + (\mathbf{k}_1 \leftrightarrow \mathbf{k}_2) \right] + \text{perms}. \end{aligned}$$

The contributing modes to the bispectrum, being horizon-size or close to horizon-size, will have undergone thermal freeze-out.

To test the effectiveness of this inflation model, the interest is in the largest scale, the 60th efold of inflation, which corresponds to the largest presently observable

scale. This scale contains the first observable perturbation to exit the inflationary horizon.

The freeze-out wavenumber, k_F , is dependent on H , but recall H varies very slowly during inflation. So we can treat k_F as a constant with H evaluated 60 e-folds before the end of inflation, which corresponds to the largest observable scale. The rest of the development of the wavevector can be calculated with a multiplicative factor of δt , where $\delta t = t_H - t_F$. t_H represents the time at Hubble crossing of the smallest of the three inflation perturbation modes, and t_F represents the time that the last of the three wavevectors freezes in,

$$e^{H\delta t} = \frac{k_F}{H}. \quad (4.34)$$

This is everything which is needed to calculate the three-point correlation function in Fourier space of the gravitational potential due to warm inflation.

So, when the first wavelength corresponding to present observations crosses the horizon, we have

$$\begin{aligned} \langle \delta\phi(\mathbf{k}_1, t_H)\delta\phi(\mathbf{k}_2, t_H)\delta\phi(\mathbf{k}_3, t_H) \rangle &= A(k_F)\delta t A(k_F)^{-1}B(t_F) \\ &\quad [2P_\phi(\mathbf{k}_1)P_\phi(\mathbf{k}_2)(2\pi)^3\delta^3(\mathbf{k}_1 + \mathbf{k}_2 + \mathbf{k}_3)] + \text{perms}, \end{aligned} \quad (4.35)$$

where P_ϕ is defined by

$$\langle \delta\phi(\mathbf{k}_1)\delta\phi(\mathbf{k}_2) \rangle = (2\pi)^3\delta^3(\mathbf{k}_1 + \mathbf{k}_2)P_\phi(\mathbf{k}_1). \quad (4.36)$$

The relation between the scalar field fluctuation and the gravitational field is given in equation (4.9).

Thus the bispectrum of the gravitational potential is given by

$$\begin{aligned} \langle \Phi(\mathbf{k}_1)\Phi(\mathbf{k}_2)\Phi(\mathbf{k}_3) \rangle &= -2 \left(\frac{3H}{5\dot{\phi}} \right)^3 \left[\frac{1}{H} \ln \left(\frac{k_F}{H} \right) \frac{V'''(\phi_0(t_F))}{\Gamma} \right] \\ &\quad (2\pi)^3\delta^3(\mathbf{k}_1 + \mathbf{k}_2 + \mathbf{k}_3) [P_\phi(\mathbf{k}_1)P_\phi(\mathbf{k}_2) + P_\phi(\mathbf{k}_1)P_\phi(\mathbf{k}_3) + P_\phi(\mathbf{k}_2)P_\phi(\mathbf{k}_3)]. \end{aligned} \quad (4.37)$$

4.3 Comparisons with The Predictions of Other Models

4.3.1 Estimating the Magnitude of the Non-Gaussianity

Gangui et al. calculated the skewness for a variety of possible inflation models using the expression in equation (4.12).

To solve the horizon problem of the FRW model, the Universe must undergo ~ 60 e-folds of inflation (Section 1.2, Appendix F). Recalling the quantity defined in equation (4.12); for the largest presently observable scale, this quantity is

$$X_{60} = X(\alpha_{60}). \quad (4.38)$$

Writing Gangui et al's equation (4.12) for this scale,

$$\begin{aligned} \langle \Phi(\mathbf{k}_1)\Phi(\mathbf{k}_2)\Phi(\mathbf{k}_3) \rangle &= \frac{5m_{\text{pl}}X_{60}}{24\pi} \left[\frac{X_{60}}{2m_{\text{pl}}} - \frac{2X'_{60}}{X_{60}} - \frac{2m_{\text{pl}}}{16\pi X_{60}} \int_{k_*}^{k_{60}} \frac{dk}{k} X''_{60} X_{60} \right] \\ & (2\pi)^3 \delta^3(\mathbf{k}_1 + \mathbf{k}_2 + \mathbf{k}_3) [P_\Phi(\mathbf{k}_1)P_\Phi(\mathbf{k}_2) + P_\Phi(\mathbf{k}_1)P_\Phi(\mathbf{k}_3) + P_\Phi(\mathbf{k}_2)P_\Phi(\mathbf{k}_3)], \end{aligned} \quad (4.39)$$

it becomes clear that for single-field, slow-roll inflation, one can write a general expression for the bispectrum

$$\begin{aligned} \langle \delta\Phi(\mathbf{k}_1)\delta\Phi(\mathbf{k}_2)\delta\Phi(\mathbf{k}_3) \rangle &= A_{\text{infl}} \\ & (2\pi)^3 \delta^3(\mathbf{k}_1 + \mathbf{k}_2 + \mathbf{k}_3) [P_\Phi(\mathbf{k}_1)P_\Phi(\mathbf{k}_2) + \text{perms}]. \end{aligned} \quad (4.40)$$

Comparative estimates for the non-Gaussianity of the cosmic microwave background can thus be calculated using A_{infl} and the shape of the inflationary potential.

To compare expression (4.37) to an equation of the form above, the bispectrum must be written in terms of the power spectra of the peculiar gravitational potential.

$$\langle \Phi(\mathbf{k}_1)\Phi(\mathbf{k}_2) \rangle = (2\pi)^3 \delta^3(\mathbf{k}_1 + \mathbf{k}_2) P_\Phi(\mathbf{k}_1). \quad (4.41)$$

$\langle \delta\phi\delta\phi \rangle \sim P_\phi$ so, from equation (4.9)

$$P_\phi = \left(\frac{5}{3}\right)^2 \left(\frac{\dot{\phi}}{H}\right)^2 P_\Phi. \quad (4.42)$$

A_{infl} in the bispectrum of the gravitational field for warm inflation, from equation (4.37), is

$$A_{\text{infl}}^{\text{warm}} = -2 \left(\frac{5\dot{\phi}}{3H}\right) \left[\frac{1}{H} \ln\left(\frac{k_F}{H}\right) \frac{V'''(\phi_0(t_F))}{\Gamma} \right]. \quad (4.43)$$

$A_{\text{infl}}^{\text{warm}}$ can be evaluated with the aid of Berera (1997), which explores the temperature and expansion behaviour of the Universe for various shapes of inflationary potential for the case of warm inflation.

Turning to the specific potentials, we consider potentials of the form

$$V(\phi_0) = \lambda M^{4-q} (M - \phi_0)^q, \quad (4.44)$$

in the region $0 < \phi < M$, where ϕ begins at 0. Quantum field theories with interaction terms in the Lagrangian $\sim \phi^N$ with $N > 4$ are non-renormalizable in four space-time dimensions, meaning that the interactions themselves will always have unconstrained momenta (see e.g. Peskin & Schroeder, 1995, chapter 10).

λ is dimensionless. M set at the grand unified scale $\sim 10^{14}\text{GeV}$. These potentials are not of the form of a symmetry breaking potential. They can, however, lead to inflation occurring in a scenario where the polynomial potential makes up part of another potential where, at some point, the slow-roll or strong dissipation conditions are locally satisfied allowing inflation to begin, and at a later stage the potential locally has a form which causes inflation to end.

Berera (1997) finds a solution for ϕ to be

$$\phi(t) = M \left\{ 1 - \left[\frac{q(q-2)\lambda M^2}{\Gamma} t + 1 \right]^{\frac{1}{2-q}} \right\}, \quad (4.45)$$

for $q \neq 2$. From this we find the form of $\dot{\phi}$.

For the purpose of a primary comparison with supercooled inflation, we selected the case where $q = 4$. Berera (1997) gives the number of e-folds of inflation, N_e , for this quartic potential to be

$$N_e = \frac{1}{2} \left(1 + \frac{2\pi\Gamma^2}{3m_{\text{pl}}^2\lambda} \right), \quad (4.46)$$

and from this, for $N_e = 60$, we find the value of the dissipation coefficient, Γ , in terms of the coupling constant λ .

The fluctuations in the scalar field caused by thermal interactions with the radiation field are related to the temperature by

$$\delta\phi^2 = \frac{k_F T}{2\pi^2}. \quad (4.47)$$

T can be calculated using the relation $\rho_r = (g_*\pi^2/30)T^4$ taking into account the relation between the radiation energy density and the scalar field potential presented in equation (4.15), the stress-energy equation for a Universe dominated by these two terms.

These quantities do not fix the value of the coupling constant for the inflaton potential term in the Lagrangian, λ . To fix the coupling constant we needed to

consider the form of the warm inflation power spectrum. We assume a general power-law form of the scalar field power spectrum.

$$P_{\Phi}(k) = \delta_H^2 k^{n-4}. \quad (4.48)$$

Taylor & Berera (2000) find n for the case of strong dissipation to be unity for a quartic potential. The value of the amplitude, δ_H^2 , is fixed by the 1991 COBE CMB satellite data (Smoot *et al.*, 1991; Bunn & White, 1995; Bunn *et al.*, 1996)

$$\delta_H \equiv \frac{2}{5} \frac{H}{\dot{\phi}} \delta\phi = 1.94 \times 10^{-5}, \quad (4.49)$$

in the case $n = 1$.

Using equations (4.49), (4.48), (4.46) and (4.45), the value of λ

$$\lambda = 3.81 \times 10^{-16}, \quad (4.50)$$

and this gives us all the quantities needed to evaluate A_{infl} for warm inflation, equation (4.43)

$$A_{\text{infl}}^{\text{warm}} = 7.44 \times 10^{-2}. \quad (4.51)$$

The equivalent quantity to A_{infl} for supercooled inflation appears in Gangui *et al.* (1994) as $\Phi_3 \equiv A_{\text{infl}}^{\text{supercooled}} = 5.56 \times 10^{-2}$ for a quartic potential. Therefore for this potential the prediction of non-Gaussianity for warm inflation is of the same order as that predicted for supercooled inflation.

General relativistic second-order perturbation theory produces further contributions to A_{infl} for both models. $A_{\text{infl}}^{\text{2nd order}} = \mathcal{O}(1)$ (Pyne & Carroll, 1996; Komatsu & Spergel, 2001). So it appears that either of the two former contributions to the bispectrum is a correction to this larger non-Gaussian contribution.

4.3.2 The Bispectrum of the Cosmic Microwave Background

We followed the standard method to convert the bispectrum of the 3-D gravitational perturbation at horizon exit to the bispectrum of the distribution of the CMB over the sky, outlined in Wang & Kamionkowski (2000) and Section 1.3 of this thesis, modelling the Sachs-Wolfe effect, applicable for the CMB power spectrum upto angular multipoles of $l \sim 50$.

$$a_{lm} \equiv \int d^2\Omega \frac{\Delta T(\Omega)}{T} Y_{lm}^*(\Omega). \quad (4.52)$$

The CMB bispectrum has the form:

$$\langle a_{l_1 m_1} a_{l_2 m_2} a_{l_3 m_3} \rangle = \begin{pmatrix} l_1 & l_2 & l_3 \\ m_1 & m_2 & m_3 \end{pmatrix} B_{l_1 l_2 l_3}, \quad (4.53)$$

where $\begin{pmatrix} l_1 & l_2 & l_3 \\ m_1 & m_2 & m_3 \end{pmatrix}$ is a *Wigner-3J*. The Wigner 3-J symbols are a more symmetrical form of the Clebsch-Gordon coefficients, $C_{m_1 m_2 m_3}^{l_1 l_2 l_3}$, which are the familiar coefficients obtained when transforming between angular momentum bases in quantum mechanics, and one is related to the other as

$$C_{m_1 m_2 m_3}^{l_1 l_2 l_3} = (-1)^{-m_3 + l_1 - l_2} \sqrt{2l_3 + 1} \begin{pmatrix} l_1 & l_2 & l_3 \\ m_1 & m_2 & -m_3 \end{pmatrix}. \quad (4.54)$$

The functional form of the Wigner or Clebsch-Gordon coefficients can be found in, e.g. Abramowitz & Stegun (1965), Section 27.

The bispectrum estimator of the CMB, averaged over m , can be written as

$$B_{l_1 l_2 l_3} = \left(\frac{1}{3}\right)^3 (4\pi)^4 \sqrt{\frac{(2l_1 + 1)(2l_2 + 1)(2l_3 + 1)}{4\pi}} \begin{pmatrix} l_1 & l_2 & l_3 \\ 0 & 0 & 0 \end{pmatrix} \int dk_1 dk_2 k_1^2 k_2^2 A_{\text{infl}} P_\Phi(k_1) P_\Phi(k_2) \times j_{l_1}^2(k_1 \Delta \eta) j_{l_2}^2(k_2 \Delta \eta) + \text{perms.} \quad (4.55)$$

The j_l s are spherical bessel functions. The normalization of the density perturbations Bunn *et al.* (1996) is specified at the present Hubble scale $k = a_0 H_0$. The density perturbations are related to the perturbations to the gravitational potential via the Poisson equation. Thus

$$P_\Phi(k = a_0 H_0) = \frac{9}{2} \pi^2 \Omega_0^{-2} \delta_H^2 k^{-3} \left(\frac{k}{k_*}\right)^{n-1}, \quad (4.56)$$

although this is simpler for a spacially flat Universe with an inflationary power spectrum with n equal to 1. The density perturbations develop with time, but comoving gravitational perturbations do not develop.

To find if the difference between the two models is detectable, for either the Sachs-Wolfe region or the bispectrum calculated upto higher multipoles using modified Boltzmann codes Komatsu & Spergel (2001), we carried out a calculation of the total error on an evaluation of A_{infl} from the bispectrum. This is calculated inversely weighting the error on the bispectrum according to cosmic variance, Verde *et al.* (2000) outlines the approach. Many values of l_1 , l_2 and l_3 do not contribute to the bispectrum, or the weighted error, due to the restrictions on the

number of independent bispectrum triangles. The *triangle relations* specify that the Wigner-3Js $\begin{pmatrix} l_1 & l_2 & l_3 \\ 0 & 0 & 0 \end{pmatrix}$ are non-zero when $|l_1 - l_2| \leq l_3$ and $l_1 + l_2 + l_3$ is even.

$$\sigma_{A_{\text{infl}}}^{-2} \sim \sum_{l_1 \leq l_2 \leq l_3} \frac{(B_{l_1 l_2 l_3} A_{\text{infl}}^{-1})^2}{C_{l_1} C_{l_2} C_{l_3}}. \quad (4.57)$$

The calculations of the error on A_{infl} carried out by Verde *et al.* (2000) and Komatsu & Spergel (2001) show the values of A_{infl} we found in the previous section are undetectable for the Sachs–Wolfe region.

4.4 Conclusions

We have calculated the non-Gaussianity expected for a warm inflation scenario in the case of strong dissipation. Such a calculation has not been carried out before, and until now it has not been known whether the non-Gaussianity generated by warm inflation would be greater than or less than that predicted for standard inflation. The inherently classical mechanism for the generation of fluctuations in warm inflation, which is palpably different from the corresponding mechanism for supercooled inflation, has been shown to produce a level of non-Gaussianity of approximately the same magnitude.

The non-Gaussianity caused by higher-order gravitational effects is an order of magnitude greater than the non-Gaussianity generated by the self-interaction of the inflaton field in either warm inflation or supercooled inflation, and even this level of non-Gaussianity is undetectable in the Sachs-Wolfe regime. With the best foreground subtraction, in the case where this relation could be applied to the entire range of CMB power spectrum values, Planck could not obtain an error on A_{infl} of less than 10.

It is interesting to note that warm inflation also occurs in the weak-dissipative regime, $\Gamma < H$ (Berera & Fang, 1995; de Oliveira & Ramos, 1998; de Oliveira & Jors, 1998). The non-Gaussianity for the weak dissipation picture has yet to be calculated.

Chapter 5

Conclusions

In this thesis I have outlined three research topics. My research has been on developing tests, analysis methods and predictions of early Universe theories for the new high quality data expected from the MAP and Planck satellite experiments. This data, of high accuracy and completeness, will lead to accurate determination of cosmological parameters, provided that certain theoretical hurdles are passed.

The basic assumption of current parameter estimation techniques is about the nature of the structure formation model which seeded the cosmological large-scale structure. This is assumed to be a single-field, slow-roll inflation model with the present Universe having ingredients including a cold dark matter component and possibly a cosmological constant component.

Before the data can usefully be analysed for parameter fitting the observations must be tested for consistency with inflation. As a result my first project, which I outline in Chapter 2, is a model-independent test of the Gaussianity of the anisotropies in the CMB. A Gaussian spectrum of perturbations would be a key signature of a single field inflation model, and the limiting case for large numbers of fields in multiple field inflation models. We carried out the calculation of the correlation function of peaks in the microwave background for Gaussian perturbations distributed over a sphere. The resulting expression, for a given power spectrum, has **no** other parameter dependence, and, making no flat sky-approximation, applies for all sky separations, so is complete.

We also carried out a comparison of the bispectrum as a discriminant for Gaussianity versus the correlation function of peaks, using a simulated $12.5^\circ \times 12.5^\circ$ dataset modelling a cosmic string seeded field of CMB anisotropies. The bispec-

trum could not distinguish the data from a Gaussian field. We found, however, that the peak correlation function displayed clear excess of correlation on small scales for the cosmic string model. For this model, the correlation function of peaks was significantly better at detecting the non-Gaussianity.

In the absence of a well-motivated non-Gaussian model to test, it makes no sense to ask whether this method is better than others. One should try everything; however, the example of a string map, where the non-Gaussian features are perhaps more easily characterized on the real sky, it is not surprising that a sky-based non-Gaussian test fares better than a Fourier-based test. Furthermore, the wealth of structure in the peak-peak correlation function means that agreement with the theoretical Gaussian curve would be a powerful argument in favour of inflation.

In Chapter 3 I reviewed my second project, which is a method of extremely fast parameter estimation for inflationary models from the CMB power spectrum, using the MOPED algorithm (Heavens *et al.*, 2000). This process can be relatively time-consuming using a brute-force maximum likelihood solution. MOPED reduces the $\lesssim 2000$ to ~ 12 uncorrelated numbers, allowing very rapid estimation of parameters, as well as a factor ~ 100 less storage for model predictions.

The improvement in CPU time to calculate a likelihood with compressed data, with close to the same shape at the maximum likelihood peak, over that required for the Planck-size dataset with 2000 power spectrum datapoints and ~ 12 parameters, is a speed up factor of around 500 million. This large acceleration is based on the presumption that CMBFAST power spectra are pre-computed prior to launch. This chapter represents the most extreme application of the MOPED method to date. The speed-up in the likelihood evaluation is stunning, to the extent that this step of the analysis need never be dominant, so the data pipeline will be dominated by bottlenecks elsewhere (Tegmark *et al.*, 2001).

The third and final project I included in this thesis is based on a variation on the standard inflationary scenario. Recalling that the standard inflation model makes the assumption that the inflation field and radiation field do not interact during the inflationary phase, and that it needs the reheating mechanism to convert the larger part of the stress-energy of the Universe at the end of the inflationary stage into radiation. The unresolved problems in the preheating mechanism, which lead to inflation exiting to a Universe with too high a temperature, are

avoided altogether in the warm inflationary scenario.

I investigated the CMB properties of the Warm Inflation model, concentrating on its non-Gaussian properties. In Chapter 4, I reviewed the calculation of the CMB bispectrum of the fluctuations for a Warm Inflation model, and the examination its testability. We compute the gravitational bispectrum of the fluctuations generated for Warm Inflation, for the particular case of strong dissipation, and the form of the resulting CMB bispectrum in the Sachs-Wolfe regime. Our conclusion is the number of bispectrum modes which would be required to observe the non-Gaussian effects is not sufficient in the Sachs-Wolfe region of the CMB bispectrum.

We find that the predictions for the bispectrum of warm inflation with strong dissipation are essentially the same as for standard supercooled inflation. In a sense this is a disappointment, as there is no prospect of distinguishing warm inflation from supercooled on the basis of this non-Gaussianity test.

These projects present a base from which further tests of the CMB can deepen our understanding of the mechanisms which cause structure to exist in the Universe. There are several some gaps still in the understanding of the consequences and predictions of inflation models, which should to be addressed before we deal with large datasets. There are a number of early Universe models which predict a structure-seeding spectrum of primordial density perturbations. Consistency tests of the form of fluctuations together with accurate predictions of non-Gaussianity are an important tool in sorting inflationary theories.

Branching off particularly from the projects covered in this thesis is the possibility for calculating the bispectrum for warm inflation up to high multipoles. This would involve much more than using the full form of the photon transfer function. For most forms of inflationary potential, for example a quartic or exponential potential, the assumptions which hold within a small number of e-folds of inflation cannot be held true. For example, changes in the Hubble parameter will have to be taken into account when correlating a mode of fluctuation which exited the horizon 60 e-folds before the end of inflation with one which left at the last e-fold. Likewise, one has to take into account the effect of bispectrum modes being binned together, with a bispectrum triangle of the same size, but falling at the beginning, middle and end of inflation, with all inflationary quantities being significantly different at each of these times. This calculation would be more

complicated, but the basis for it is in Chapter 4, and may produce a result which could be tested against the CMB. Another project of interest is the calculation of non-Gaussianity for weak dissipation regime for the warm inflationary scenario.

Branching off more broadly from the work in this thesis is the usefulness of developing tests of non-Gaussianity which could distinguish Braneworld early Universe models. The growing number of well-motivated early Universe models strengthens the argument for thorough consistency tests within the cosmological parameter estimation machine which will be operating on the CMB maps.

Bibliography

- Abramowitz, M., Stegun, I. A., 1965. *Handbook of Mathematical Functions with Formulas, Graphs and Mathematical Tables*. U.S. Department of Commerce, National Bureau of Standards.
- Adler, R. J., 1981. *The Geometry of Random Fields*. Chichester : Wiley.
- Aghanim, N., Forni, O., 1999, *Astron. Astrophys.*, **347**, 409.
- Albrecht, A., Steinhardt, P., 1982, *Phys. Rev. Lett.*, **48**, 1220.
- Albrecht, A., Steinhardt, P., Turner, M., Wilczek, F., 1982, *Phys. Rev. Lett.*, **48**, 1437.
- Avelino, P. P., Martins, C. J. A. P., 2000, **85**, 1370.
- Balbi, A., Ade, P., Bock, J., Borrill, J., Boscaleri, A., Bernardis, P. D., Ferreira, P. G., Hanany, S., Hristov, V., Jaffe, A. H., Lee, A. T., Oh, S., Pascale, E., Rabbii, B., Richards, P. L., Smoot, G. F., Stompor, R., Winant, C. D., Wu, J. H. P., 2001, *Ap. J.*, **545**, L1.
- Balbi, A., Ade, P., Bock, J., Borrill, J., Boscaleri, A., Bernardis, P. D., Ferreira, P. G., Hanany, S., Hristov, V., Jaffe, A. H., Lee, A. T., Oh, S., Pascale, E., Rabbii, B., Richards, P. L., Smoot, G. F., Stompor, R., Winant, C. D., Wu, J. H. P., 2001, *Ap. J.*, **558**, L145.
- Banday, A. J., Zaroubi, S., Górski, K. M., 2000, *Ap. J.*, **533**, 575–587.
- Banks, T., Kaplan, D. B., Nelson, A., 1994, *Phys. Rev. D*, **49**, 779.
- Bardeen, J. M., Steinhardt, P. J., Turner, M. S., 1983, *Phys. Rev. D*, **28**, 679.
- Bardeen, J. M., Bond, J. R., Kaiser, N., Szalay, A. S., 1986, *Ap. J.*, **304**, 15.

- Barreiro, R., Sanz, J., Martínez-González, E., Cayon, L., J.Silk, 1997, *Ap. J.*, **478**, 1.
- Barreiro, R., Sanz, J., Martínez-González, E., J.Silk, 1998, *Mon. Not. R. Astr. Soc.*, **296**, 693.
- Barreiro, R., Martínez-González, E., Sanz, J., 2001, *Mon. Not. R. Astr. Soc.*, **322**, 411.
- Barrow, J. D., Coles, P., 1990, *Mon. Not. R. Astr. Soc.*, **244**, 188.
- Berera, A., 1995, *Phys. Rev. Lett.*, **75**, 3218.
- Berera, A., 1996, *Phys. Rev. D*, **54**, 2519.
- Berera, A., 1997, *Phys. Rev. D*, **55**, 3346.
- Berera, A., 2000, *Nuclear Phys. B.*, **585**, 666.
- Berera, A., Fang, L., 1995, *Phys. Rev. Lett.*, **74**, 1912.
- Berera, A., Kephart, T. W., 1999, *Phys. Lett. B*, **456**, 135.
- Berera, A., Kephart, T. W., 1999, *Phys. Rev. Lett.*, **83**, 1084.
- Berera, A., Ramos, R. O., 2001, *Phys. Rev. D*, **63**, 103509.
- Berera, A., Gleiser, M., Ramos, R. O., 1998, *Phys. Rev. D*, **58**, 123508.
- Berera, A., Gleiser, M., Ramos, R. O., 1999, *Phys. Rev. Lett.*, **83**, 264.
- Bond, J. R., 1995, **74**, 4369.
- Bond, J. R., Efstathiou, G. P., 1987, *Mon. Not. R. Astr. Soc.*, **226**, 655.
- Bond, J. R., Jaffe, A. H., Knox, L., 1998, **57**, 2117B.
- Bond, J. R., Crittenden, R. G., Jaffe, A. H., Knox, L., 1999, *Comput. Sci. Eng.*, **1**, 21.
- Borrill, J., 1999, **59**, 7302.
- Bromley, B., Tegmark, M., 1999, *Ap. J. Lett.*, **524**, 79.
- Bunn, E. F., Sugiyama, N., 1995, *Ap. J.*, **446**, 49.

- Bunn, E. F., White, M., 1995, *Ap. J.*, **450**, 477.
- Bunn, E. F., Liddle, A. R., White, M., 1996, *Phys. Rev. D*, **54**, 5917.
- Coles, P., 1988, *Mon. Not. R. Astr. Soc.*, **234**, 509.
- Coles, P., Lucchin, F., 1995. *Cosmology: The Origin and Evolution of Cosmic Structure*. Wiley.
- Colless, M., 2dF Galaxy Redshift Survey Team, Large scale structure from the 2df galaxy redshift survey, in *American Astronomical Society Meeting*, volume 197, page 8905, 2000.
- Coulson, D., Crittenden, R., Turok, N., 1994, *Phys. Rev. Lett.*, **73**, 2390.
- Cress, C. M., Probing density fluctuations in the universe with the first radio survey, in *IAU Symposium: Cosmological Parameters and the Evolution of the Universe*, volume 183, page 244, 1999.
- Davis, R. L., Hodges, H. M., Smoot, G. F., Steinhardt, P. J., Turner, M. S., 1992, *Phys. Rev. Lett.*
- de Bernardis, P., Ade, P., Bock, J., Bond, J., Borrill, J., Boscaleri, A., Coble, K., Contaldi, C., Crill, B., Troia, G. D., Farese, P., Ganga, K., Giacometti, M., Hivon, E., Hristov, V., Iacoangeli, A., Jaffe, A., Jones, W., Lange, A., Martinis, L., Masi, S., Mason, P., Mauskopf, P., A. Melchiorri, Montroy, T., Netterfield, C., Pascale, E., Piacentini, F., Pogosyan, D., Polenta, G., Pongetti, F., Prunet, S., Romeo, G., Ruhl, J., Scaramuzzi, F., 2001, submitted to *Ap. J.*, **astroph-0105296**.
- de Carlos, B., Casas, J. A., Quevedo, F., Roulet, E., 1993, *Phys. Lett. B*, **318**, 447.
- de Oliveira, H. P., Jors, S. E., 1998, *Phys. Rev. D*, **64**, 063513.
- de Oliveira, H. P., Ramos, O. R., 1998, *Phys. Rev. D*, **57**, 741.
- Dolgov, A., Linde, A., 1982, *Phys. Lett. B*, **116**, 329.
- Ellis, G. F. R., Lyth, D. H., Mijić, M. B., 1986, *Phys. Lett. B*, **174**, 176.
- Falk, T., Rangarajan, R., Srednicki, M., 1993, *Ap. J. Lett.*, **403**, 1.

- Ferreira, P., Magueijo, J., Gorski, K., 1998, *Ap. J. Lett.*, **503**, 1.
- Fisher, R. A., 1935, *J. Roy. Stat. Soc.*, **98**, 39.
- Forni, O., Aghanim, N., 1999, *Astron. Astrophys. Suppl.*, **137**, 553.
- Freedman, W. L., Madore, B. F., Gibson, B. K., Ferrarese, L., Kelson, D. D., Sakai, S., Mould, J. R., Kennicutt Jr., R. C., Ford, H. C., Graham, J. A., Huchra, J. P., Hughes, S. M. G., Illingworth, G. D., Macri, L. M., Stetson, P. B., 2001, *Ap. J.*, **553**, 47.
- Gangui, A., Martin, J., 2000, *Mon. Not. R. Astr. Soc.*, **313**, 323.
- Gangui, A., Lucchin, F., Matarrese, S., Mollerach, S., 1994, *Ap. J.*, **430**, 447.
- Goldenfeld, N., 1992. *Lectures on Phase Transitions and the Renormalization Group*. Addison-Wesley.
- Gorski, K., 1994, *Ap. J.*, **430**, L85.
- Gorski K. et al., 1994, *Ap. J.*, **430**, L89.
- Gott, J. R., Park, C., Juskiewicz, R., Bies, W., Bennett, D., Bouchet, F., Stebbins, A., 1990, *Ap. J.*, **352**, 1.
- Guth, A. H., 1981, *Phys. Rev. D*, **23**, 347.
- Heavens, A. F., 1998, *Mon. Not. R. Astr. Soc.*, **299**, 805.
- Heavens, A. F., Sheth, R. K., 1999, *Mon. Not. R. Astr. Soc.*
- Heavens, A. F., Matarrese, S., Verde, L., 1998, *Mon. Not. R. Astr. Soc.*, **301**, 797.
- Heavens, A. F., Jimenez, R., Lahav, O., 2000, *Mon. Not. R. Astr. Soc.*, **317**, 965–972.
- Hinshaw, G., Kogut, A., Gorski, K., Banday, A., Bennett, C., Lineweaver, C., Lubin, P., Smoot, G., Wright, E., 1994, *Ap. J.*, **431**, 1.
- Hu, W., Sugiyama, N., 1996, *Ap. J.*, **471**, 542.
- Hubble, E. P., 1927, *Proc. Nat. Acad. Sci.*, **15**, 168.

- Jungman, G., Kamionkowski, M., Kowowsky, A., Spergel, D. N., 1996, Phys. Rev. D, **54**, 1332.
- Kamionkowski, M., Jaffe, A., 1998, Nature, **395**, 639.
- Kamionkowski, M., Spergel, D. N., Sugiyama, N., 1994, Ap. J. Lett., **426**, L57.
- Kendall, M. G., Stuart, A., 1969. *The Advanced Theory of Statistics*. London:Griffin.
- Kiefer, C., 2000, Nucl. Phys. B Proc. Suppl., **88**, 1.
- Kofman, L., Linde, A., Starobinsky, A. A., 1994, Phys. Rev. Lett., **73**, 3195.
- Kogut, A., Banday, A., Bennett, C., Hinshaw, G., Lubin, P., Smoot, G., 1995, Ap. J., **439**, L29.
- Kogut, A., Banday, A., Bennett, C., Gorski, K., Hinshaw, G., Smoot, G., Wright, E., 1996, Ap. J., **464**, L29.
- Kolb, E. W., Turner, M. S., 1990. *The Early Universe*. Addison-Wesley.
- Komatsu, E., Spergel, D. N., 2001, Phys. Rev. D, **63**, 063002.
- Landau, L. D., Lifshitz, E. M., 1977. *Quantum Mechanics (Non-relativistic Theory) Third Edition*. Pergamon Press.
- LeBellac, M., 1991. *Quantum and Statistical Field Theory*. Oxford Science Publications.
- Liddle, A. R., Lyth, D. H., 1993, Phys. Rep.
- Linde, A. D., 1982, Phys. Lett. B, **108**, 389.
- Luo, X., 1994, Ap. J. Lett., **427**, 71.
- Luo, X., 1994, Phys. Rev., **D49**, 3810.
- Luo, X., Schramm, D., 1993, Phys. Rev. Lett., **71**, 1124.
- Lyth, D. H., 2000, Phys. Lett. B, **476**, 356.
- Magueijo, J., 2000, Ap. J. Lett., **528**, 57.
- Matarrese, S., L.Verde, A.F.Heavens, 1997, Mon. Not. R. Astr. Soc.

- Matarrese, S., Verde, L., Jimenez, R., 2000, *Ap. J.*, **541**, 10.
- Mollerach, S., Matarrese, S., Ortolan, A., Lucchin, F., 1991, *Phys. Rev. D*, **44**, 1670.
- Muciaccia, P. F., Natoli, P., Vittorio, N., 1997, *Ap. J. Lett.*, **488**, L63-+.
- Mukherjee, P., Hobson, M. P., Lasenby, A. N., 2000, *Mon. Not. R. Astr. Soc.*, **318**, 1157.
- Natoli, P., de Gasperis, G., Gheller, C., Vittorio, N., 2001, *Astron. Astrophys.*, **372**, 346-356.
- Olive, S., Spergel, D., Hinshaw, G., 1999, *Ap. J.*, **510**, 551.
- Outram, P. J., Hoyle, F., Shanks, T., Croom, S. M., Boyle, B. J., Loaring, N. S., Miller, L., Smith, R. J., Probing density fluctuations in the universe with the first radio survey, in *AGN Surveys, Proceedings of IAU Colloquium*, eds. R. Green, E. Khachikian, and D. Sanders, volume 184, ASP, 2001.
- Pando, J., Valls-Gabaud, D., Fang, L., 1998, **79**, 1611.
- Partridge, R. B., 1995. *3K: The Cosmic Microwave Background Radiation*. Cambridge University Press.
- Peacock, J. A., 1996. Inflationary cosmology and structure formation. Lectures given at the EADN summer school "The structure of the universe", Leiden, July 1995, astro-ph/9601135.
- Peacock, J. A., 1999. *Cosmological Physics*. Cambridge University Press.
- Peebles, P. J. E., 1993. *Principles of Physical Cosmology*. Princeton University Press.
- Pen, U.-L., Seljak, U., Turok, N., 1997, *Phys. Rev. Lett.*, **79**, 1611.
- Penzias, A. A., Wilson, R. W., 1965, *Ap. J.*, **142**, 419.
- Percival, W., Baugh, C., Bland-Hawthorn, J., Bridges, T., Cannon, R., Cole, S., Colless, M., Collins, C., Couch, W., Dalton, G., Propis, R. D., Driver, S., Efstathiou, G., Ellis, R., Frenk, C., Glazebrook, K., Jackson, C., Lahav, O., Lewis, I., Lumsden, S., Maddox, S., Moody, S., Norberg, P., Peacock, J.,

- Peterson, B., Sutherland, W., Taylor, K., 2001, *Mon. Not. R. Astr. Soc.*, **327**, 1297.
- Perlmutter, S., Aldering, G., Goldhaber, G., Knop, R. A., Nugent, P., Castro, P. G., Deustua, S., Fabbro, S., Goobar, A., Groom, D. E., Hook, I. M., Kim, A. G., Kim, M. Y., Lee, J. C., Nunes, N. J., Pain, R., Pennypacker, C. R., Quimby, R., Lidman, C., Ellis, R. S., Irwin, M., McMahon, R. G., Ruiz-Lapuente, P., Walton, N., Schaefer, B., Boyle, B. J., Filippenko, A. V., Matheson, T., Fruchter, A. S., Panagia, N., Newberg, H. J. M., Couch, W. J., Project, T. S. C., 1999, *Ap. J.*, **517**, 565.
- Peskin, M. E., Schroeder, D., 1995. *An Introduction to Quantum Field Theory*. Addison-Wesley.
- Pyne, T., Carroll, S. M., 1996, *Phys. Rev. D*, **53**, 2920.
- Rae, A. I. M., 1980. *Quantum Mechanics*. Institute of Physics Publishing, Bristol and Philadelphia.
- Reif, F., 1965. *Fundamentals of Statistical and Thermal Physics*. McGraw-Hill Kogakusha.
- Robinson, J., Gawiser, E., Silk, J., 2000, *Ap. J.*, **532**, 1–16.
- Salopek, D. S., Bond, J. R., 1990, *Phys. Rev. D*, **42**, 3936.
- Seljak, U., Zaldarriaga, M., 1996, *Ap. J.*, **469**, 437.
- Simatos, N., Perivolaropoulos, L., 2000, **0009294**.
- Slipher, V. M., Table prepared for A. S. Eddington, in *The Mathematical Theory of Relativity*, page 162, Cambridge University Press, 1924.
- Smoot, G. F., Bennett, C. L., Kogut, A., Aymon, J., Backus, C., de Amici, G., Galuk, K., Jackson, P. D., Keegstra, P., Rokke, L., Tenorio, L., Torres, S., Gulkis, S., Hauser, M. G., Janssen, M. A., Mather, J. C., Weiss, R., Wilkinson, D. T., Wright, E. L., Bogges, N. W., Cheng, E. S., Kelsall, T., Lubin, P., Meyer, S., Moseley, S. H., Murdock, T. L., Shafer, R. A., Silverberg, R. F., 1991, *Ap. J.*, **371L**, L1.

- Smoot, G. F., Bennett, C. L., Kogut, A., Wright, E. L., Aymon, J., Boggess, N. W., Cheng, E. S., De Amici, G., Gulkis, S., Hauser, M. G., Hinshaw, G., Jackson, P. D., Janssen, M., Kaita, E., Kelsall, T., Keegstra, P., Lineweaver, C., Loewenstein, K., Lubin, P., Mather, J., Meyer, S. S., Moseley, S. H., Murdock, T., Rokke, L., Silverberg, R. F., Tenorio, L., Weiss, R., Wilkinson, D. T., 1992, *Ap. J. Lett.*, **396**, L1.
- Smoot, G. F., Tenorio, L., Banday, A., Kogut, A., Wright, E. L., Hinshaw, G., Bennett, C. L., 1994, *Ap. J.*, **437**, 1.
- Stolyarov, V., Hobson, M. P., Ashdown, M. A. J., Lasenby, A. N., 2001, *astro-ph*, **0105432**.
- Stompor, R., Abroe, M., Ade, P., Balbi, A., Barbosa, D., Bock, J., Borrill, J., Boscaleri, A., de Bernardis, P., Ferreira, P. G., Hanany, S., Hristov, V., Jaffe, A. H., Lee, A. T., Pascale, E., Rabii, B., Richards, P. L., Smoot, G. F., Winant, C. D., Wu, J. H. P., 2001, *Ap. J.*, **561**, L7.
- Szapudi, I. ., Prunet, S., Pogosyan, D., Szalay, A. S., Bond, J. R., 2001, *Ap. J. Lett.*, **548**, L115.
- Takada, M., Komatsu, E., Futamase, T., 2000, *Ap. J. Lett.*, **533**, 83.
- Taylor, A. N., Berera, A., 2000, *Phys. Rev. D*, **62**, 083517.
- Tegmark, M., 1997, *Ap. J. Lett.*, **480**, L87.
- Tegmark, M., 1997, *Phys. Rev. D*, **55**, 5895.
- Tegmark, M., Taylor, A., Heavens, A., 1997, *Ap. J.*, **480**, 22.
- Tegmark, M., Zaldarriaga, M., Hamilton, A. J., 2001, *Phys. Rev. D*, **63**, 043007.
- Turner, M. S., Cosmology update 1998, in *Proceedings of Wein 98*, 1998.
- Verde, L., Heavens, A., Matarrese, S., Moscardini, L., 1998, *Mon. Not. R. Astr. Soc.*, **300**, 747.
- Verde, L., Wang, L., Heavens, A. F., Kamionkowski, M., 2000, *Mon. Not. R. Astr. Soc.*, **313**, 141.
- Vogele, M. S., Szalay, A. S., 1996, *Ap. J.*, **465**, 34.

Wang, L., Kamionkowski, M., 2000, Phys. Rev. D, **61**, 063504.

Wright, E. L., 1996, page 9612006.

Yi, I., Vishniac, E. T., 1993, Phys. Rev. D, **48**, 950.

Yokoyama, J., Linde, A., 1999, Phys. Rev. D, **60**, 083509.

Appendix A

Measuring the Hubble Constant

The range of values of the Hubble constant given in equation (1.5) are the result of the *Hubble Space Telescope Key Project* (Freedman *et al.*, 2001) to measure the Hubble constant.

The *Hubble Law* relates an object's distance, d , to its recession velocity, v , given that this object is moving with the cosmic flow:

$$v = H_0 d \tag{A.1}$$

The Hubble Law is implicit for a homogeneously expanding, homogeneous and isotropic universe.

To estimate the Hubble constant one can use the distance–luminosity relation of equation (1.2) to provide, d , and the spectroscopic observations of the object to determine the velocity of the object. This is only possible if we know the absolute luminosity, L , of the object. *Cepheids* are bright variable stars with a period of variation in their luminosity related to their absolute luminosity. This relationship can be calibrated using the presence of Cepheid variables in the *Large Magellanic Cloud*. The distance of the Large Magellanic Cloud from us has been determined directly from local kinematic distance measures.

The distance from us to which Cepheids can be observed has been extended to about 25Mpc. At this distance velocities which are *local*, meaning apart from the Hubble flow, are not cumulatively averaged out and thus affect the determination of H_0 . For Hubble parameter estimation, the further the better. Cepheid variables absolute distances to Leo I group, the Virgo cluster and the Fornax cluster

have been calculated by Freedman *et al.* (2001) with the Hubble space telescope data.

From these intermediate scales, distances to further objects can be determined using a variety of methods which link distance to other observable quantities.

The surface–brightness fluctuation method supplements the Cepheid method, and relates the fluctuations in the light from a galaxy, used to estimate the number of stars it contains, to the total apparent brightness. The range of this method is limited to approximately 70Mpc.

The empirical Tully–Fisher relation relates the circular rotation velocity, v_c , of a spiral galaxy to the absolute luminosity.

$$L \propto v_c^4. \quad (\text{A.2})$$

This relation applies to about 150Mpc.

The fundamental plane relation relates the surface brightness, I_0 , and the central velocity dispersion, σ_v , of elliptical galaxies to the absolute luminosity,

$$L \propto I_0^{-0.7} \sigma_v^3. \quad (\text{A.3})$$

This takes the distance ladder up to approximately 400Mpc. The sum of the extensions leads to the evaluation of the Hubble parameter range:

$$H_0 = 72 \pm 8 \text{ km s}^{-1} \text{ Mpc}^{-1}. \quad (\text{A.4})$$

Appendix B

Robertson-Walker Metric

The metric

$$ds^2 = c^2 dt^2 - a^2(t) dl^2, \quad (\text{B.1})$$

can be worked out accounting for curvature as on a 3D surface in a 4D space, with line element Peebles (1993),

$$dl^2 = dx^2 + dy^2 + dz^2 + dw^2. \quad (\text{B.2})$$

Transforming from 4D Cartesian to polar coordinates : A, χ, θ, ϕ ,

$$\begin{aligned} dx &= dA \\ dy &= Ad\chi \\ dz &= A \sin \chi d\theta \end{aligned} \quad (\text{B.3})$$

$$dw = A \sin \chi \sin \theta d\phi \quad (\text{B.4})$$

So now we are sitting in four spatial dimensions. We can look at our three dimensions as a surface within this larger space. The FRW model models a symmetric space, and the surface of a sphere is symmetric, with no preferred direction. For a closed model our space can be calculated as the surface of a 3-sphere of radius R ,

$$x^2 + y^2 + z^2 + w^2 = R^2. \quad (\text{B.5})$$

So we define ourselves to be on the surface $A = \text{const} = R$, the geometry of our Universe thus depending on the value we choose to define our surface at. This leaves the three angular coordinates

$$dl^2 = R^2 [d\chi^2 + \sin^2 \chi d\Omega] \quad (\text{B.6})$$

$$d\Omega = d\theta^2 + \sin^2 \theta d\phi^2. \quad (\text{B.7})$$

For the negative curvature case, and an open Universe, $R \rightarrow iR$, $\chi \rightarrow -i\chi$ so $dl^2 \rightarrow R^2[d\chi^2 + \sinh^2\chi d\Omega]$. For a flat Universe $R \rightarrow \infty$.

Now, reverting to the positive curvature case, and changing coordinates to $r = R\chi$,

$$dr = Rd\chi, \quad (\text{B.8})$$

therefore

$$\begin{aligned} dl^2 &= [dr^2 + R^2 \sin^2\chi d\Omega] \\ &= [dr^2 + R^2 \sin^2\left(\frac{r}{R}\right) d\Omega]. \end{aligned} \quad (\text{B.9})$$

Appendix C

The Friedmann Equation

The Greek indices $\mu = (0, i) = (0, 1, 2, 3)$.

The Friedmann equations are arrived at by modelling the Universe as a perfect fluid. Using Einstein's equations, which are

$$\mathcal{R}^{\mu\nu} - \frac{1}{2}\mathcal{R}g^{\mu\nu} \equiv G^{\mu\nu} \quad (\text{C.1})$$

$$= \frac{8\pi G}{c^4}T^{\mu\nu} + \Lambda g^{\mu\nu}, \quad (\text{C.2})$$

and the energy momentum tensor of a perfect fluid,

$$T^{\mu\nu} = (\rho + \frac{p}{c^2})u^\mu u^\nu - \frac{p}{c^2}g^{\mu\nu}, \quad (\text{C.3})$$

where ρ is the energy density of the fluid and p is the pressure. u^μ is the 4-velocity at the spacetime point $x^\mu = (ct, x, y, z)$, and $g_{\mu\nu}$ is the metric tensor, and $g^{\mu\nu}$ is its inverse, $ds^2 = g_{\mu\nu}dx^\mu dx^\nu$ defining the line element. Λ is the cosmological constant.

$\mathcal{R}^{\mu\nu}$ is the Ricci tensor, a function of the metric and derivatives of the metric, and \mathcal{R} is the Ricci scalar $\mathcal{R} = \mathcal{R}^\mu{}_\mu = \mathcal{R}^{\mu\nu}g_{\mu\nu}$.

Plugging all of these into the field equation, equation (C.2), the 0-0 component gives

$$\frac{\dot{a}^2}{a^2} = \frac{8\pi\rho G}{3} + \frac{c}{R^2 a^2} + \frac{\Lambda}{3}, \quad (\text{C.4})$$

and the i - i component gives

$$\frac{2\ddot{a}}{a} + \frac{\dot{a}^2}{a^2} - \frac{c}{R^2 a^2} = -\frac{8\pi G p}{c^2} + \Lambda. \quad (\text{C.5})$$

Substituting (C.4) into (C.5) gives the second Friedmann equation, independent of $\dot{a}(t)$,

$$\frac{\ddot{a}}{a} = -\frac{4\pi G}{3} \left(\frac{3p}{c^2} + \rho \right) + \frac{\Lambda}{3}. \quad (\text{C.6})$$

Appendix D

Energy and Length Units

D.1 Energy Units

There are occasions in the text where length, time, mass and temperature units are referred to in terms of energy: $[L]$ and $[t] \sim [E]^{-1}$, $[M]$ and $[T] \sim [E]$.

Here is a brief reminder of why. Any physical quantity multiplied by factors of h , c or k_B give something in terms of energy.

Using the de Broglie relation to relate the energy, E , of a wave to its frequency, f : $E = \hbar\omega$ (recalling $\hbar = h/2\pi$ and $\omega = 2\pi f$), gives $E = \hbar f$. For relativistic particles $c = \lambda f$. $E = \frac{\hbar c}{\lambda}$ i.e.

$$\frac{[L]}{\hbar c} = [E]^{-1}. \quad (\text{D.1})$$

Again using the de Broglie relation above $E = \hbar f$,

$$\frac{[t]}{\hbar} = [E]^{-1}. \quad (\text{D.2})$$

Mass is trivial,

$$[M]c^2 = [E]. \quad (\text{D.3})$$

Thermal energy, $E = k_B T$,

$$[T]k_B = [E]. \quad (\text{D.4})$$

In particle physics \hbar , c and k_B are set equal to each other and equal to one. When studying the Early Universe, where there is a smooth, thermalized distribution of relativistic particles, essentially all quantities can be characterized from the thermal energy, $k_B T$ and the only length scale of interest is the wavelength of a particle.

Defining a Planck time	$t_{\text{pl}} \simeq G^{\frac{1}{2}} \simeq 10^{-43}\text{s}$
a Planck length	$l_{\text{pl}} \simeq ct_{\text{pl}} = t_{\text{pl}} \simeq G^{\frac{1}{2}}$
a Planck density	$\rho_{\text{pl}} \simeq \frac{1}{Gt_{\text{pl}}^2} \simeq \frac{1}{G^2}$
a Planck mass	$m_{\text{pl}} \simeq \rho_{\text{pl}}l_{\text{pl}}^3 \simeq \left(\frac{1}{G}\right)^{\frac{1}{2}}$
a Planck energy	$E_{\text{pl}} \simeq m_{\text{pl}} \simeq \left(\frac{1}{G}\right)^{\frac{1}{2}}$
a Planck temperature	$T_{\text{pl}} \simeq \frac{E_{\text{pl}}}{k_B} \simeq \left(\frac{1}{G}\right)^{\frac{1}{2}} k_B^{-1}$.

When gravity becomes important, a different set of units is more useful.

D.2 Length Units

This system is not used in this thesis, but is referred to for completeness. Leaving out \hbar and using c , k_B and G to convert all quantities to powers of **length**.

Energy,	$[E]Gc^{-4} = [L]$
Time,	$[t]c = [L]$
Mass,	$[M]Gc^{-2} = [L]$
Temperature,	$[T]k_BGc^{-4} = [L]$.

Appendix E

Derivation of Formalism for Slow-Roll Inflation

E.1 Deriving the equation of motion

The equation of motion for a scalar field dominated FRW Universe is obtained by extremising the action S in equation (1.72), plugging in the form of the Lagrangian density from equation (1.64)

$$S_\phi = \int d^4x a^3 \left(\frac{1}{2} \dot{\phi}^2 - V(\phi) \right). \quad (\text{E.1})$$

$\delta S_\phi = 0$ gives the equation of motion of the field,

$$\begin{aligned} \delta S_\phi &= \int d^4x a^3 \left(\dot{\phi} \delta \dot{\phi} - V'(\phi) \delta \phi \right) \\ &= \int d^4x a^3 \left(\dot{\phi} \frac{d}{dt}(\delta \phi) - V'(\phi) \delta \phi \right) \\ &= \int d^4x \frac{d}{dt} (a^3 \dot{\phi} \delta \phi) + \int \left(-\frac{d}{dt} (a^3 \dot{\phi}) \delta \phi - V'(\phi) \delta \phi \right) d^4x, \end{aligned} \quad (\text{E.2})$$

and, given that all well behaved fields disappear at infinity,

$$= 0 - \int \left(3a^2 \dot{a} \dot{\phi} + a^3 \ddot{\phi} + a^3 V'(\phi) \right) \delta \phi d^4x. \quad (\text{E.3})$$

This must be 0 for all $\delta \phi$ so

$$3a^2 \dot{a} \dot{\phi} + a^3 \ddot{\phi} + a^3 V'(\phi) = 0, \quad (\text{E.4})$$

and dividing through by a^3 gives equation (1.73).

E.2 Deriving the Alternate Form of the Slow-Roll Conditions

We have the two slow roll conditions in the forms of equation(1.75) and equation(1.76)

$$\begin{aligned} |\ddot{\phi}| &\ll |3H\dot{\phi}| \\ \frac{\dot{\phi}^2}{2} &\ll V(\phi). \end{aligned}$$

Differentiating the equation of motion (equation 1.77), and using what the slow-roll conditions mean, i.e. slow-roll, that H changes slowly with time,

$$\ddot{\phi} \simeq \frac{-V''(\phi)\dot{\phi}}{3H}. \quad (\text{E.5})$$

Therefore the first condition can be rewritten as:

$$|-V''(\phi)| \ll |9H^2|. \quad (\text{E.6})$$

Recall we have set Ω to 1 therefore $\rho = \rho_c$,

$$\rho_c = \frac{3H^2}{8\pi G} \simeq V(\phi), \quad (\text{E.7})$$

so, replacing $G \sim m_{\text{pl}}^{-2}$ (Appendix D),

$$9H^2 \simeq \frac{24\pi V(\phi)}{m_{\text{pl}}^2} \quad (\text{E.8})$$

$$\left| \frac{V''}{V} \right| \ll \frac{24\pi}{m_{\text{pl}}^2}. \quad (\text{E.9})$$

The equation of motion (1.77) can also be used to rewrite the second condition. First rewriting it a little to get something of the form of $\dot{\phi}^2$ on one side,

$$\dot{\phi}^2 \simeq \frac{(V'(\phi))^2}{9H^2} \quad (\text{E.10})$$

$$\simeq \frac{(V'(\phi))^2}{24\pi V(\phi)} m_{\text{pl}}^2. \quad (\text{E.11})$$

So the second slow-roll condition gives

$$\frac{1}{2} \frac{(V'(\phi))^2}{24\pi V(\phi)} m_{\text{pl}}^2 \ll V(\phi) \quad (\text{E.12})$$

$$\left| \frac{V'(\phi)}{V(\phi)} m_{\text{pl}} \right| \ll (48\pi)^{\frac{1}{2}}. \quad (\text{E.13})$$

Appendix F

Solving the Horizon Problem with Inflation

Calculating, using natural units, the number of efolds required to stretch the end-inflation horizon to the present horizon size, about $3000h^{-1}$ Mpc, given an end of inflation temperature for typical inflation models, 10^{15} GeV.

The development of the scale factor with radiation temperature is determined by the following relation

$$\rho_r \equiv \left(\frac{g_* \pi^2}{30} \right) T^4, \quad (\text{F.1})$$

where g_* represents the number of degrees of freedom for the radiation field. In Section 1.1 we learned that

$$\rho_r \propto a^{-4}, \quad (\text{F.2})$$

so $a \propto (1/T)$. The energy of a relativistic particle is related to its temperature by $E = k_B T$, where k_B is Boltzmann's constant. All this leads to the fact that the scale at the end of inflation is

$$a_{EI}^{-1} = \frac{E_{EI}}{E_r}, \quad (\text{F.3})$$

recalling that $a_0 \equiv 1$. E_r is the present radiation energy, $E_r = k_B T_r$, where T_r is the temperature of today's CMB, $\sim 3K$.

$1/H$ is of the order of the physical horizon in size. So the comoving horizon at the end of inflation is approximately

$$\frac{1}{H_{EI} a_{EI}}. \quad (\text{F.4})$$

Simplifying by considering a flat, cosmological constant-free universe at inflation end. From equation (1.9),

$$H^2 = \frac{8\pi\rho G}{3}. \quad (\text{F.5})$$

Appendix D gives the relation $E_{\text{pl}} \simeq G^{\frac{1}{2}}$. Just above it is shown that $\rho_{EI} \propto T_{EI}^4 \propto E_{EI}^4$, and for inflation $V = \rho$.

Thus

$$H \sim \frac{E_{EI}^2}{E_{\text{pl}}}. \quad (\text{F.6})$$

The comoving horizon at the end of inflation, equation(F.4), can be written, in terms of energies, as

$$\frac{1}{H_{EI}a_{EI}} \simeq \left(\frac{E_{\text{pl}}}{E_r}\right) E_{EI}^{-1}. \quad (\text{F.7})$$

The number of e-folds required to solve the cosmological horizon problem of the HBB model is therefore (Peacock, 1999):

$$N_{\text{obs}} = \ln \left[\frac{3000h^{-1}\text{Mpc}}{\left(\frac{E_{\text{pl}}}{E_r}\right) E_{EI}^{-1}} \right] \simeq 60. \quad (\text{F.8})$$

This changes for different inflation potentials and reheating temperatures.

Appendix G

The Bispectrum of a Gaussian Field

A multivariate Gaussian field has the following form (Bardeen *et al.*, 1986; Adler, 1981)

$$P(x_1, \dots, x_n) = \frac{1}{(2\pi)^{\frac{n}{2}} (\det M)^{\frac{1}{2}}} \exp \left[-\frac{1}{2} (M^{-1})_{ij} x_i x_j \right] \quad (\text{G.1})$$

$$\Delta x_i = x_i - \langle x_i \rangle_{\substack{\text{range of} \\ \text{all } x}} \quad (\text{G.2})$$

M_{ij} is a positive definite symmetric matrix. I am using the Einstein summation convention, where all repeated indices are summed over. The distribution we are going to be comparing the CMB theories to is a joint probability distribution of independent scalar Gaussian fields with zero mean, $\Delta x_i = x_i$.

The moments of the distribution $\mu_n = \langle x^n \rangle$ can be calculated using a Fourier transform, or *characteristic function* of the distribution. A distribution $P(x_1, \dots, x_n)$ has characteristic function

$$G(k_1 \dots k_n) = \int d^n x P(x_1, \dots, x_n) \exp[ik_i x_i]. \quad (\text{G.3})$$

The characteristic function is the generating function for the moments of the distribution

$$(-i)^n \left. \frac{\partial^n G}{\partial k^n} \right|_{k=0} = \mu_n. \quad (\text{G.4})$$

For the distribution above

$$G(k_1, \dots, k_n) = \exp \left(-\frac{1}{2} M_{ij} k_i k_j \right), \quad (\text{G.5})$$

so

$$\langle x_i x_j \rangle = M_{ij}. \quad (\text{G.6})$$

As the fields are independent, M_{ij} is diagonal. We have

$$\langle x_i x_j \rangle = \delta_{ij} F(x_i, x_j), \quad (\text{G.7})$$

where F is some function. $\delta(\mathbf{k})$ is a complex quantity, made up of two independent Gaussian fields.

$$\delta(k) = \delta^{\text{real}} + i\delta^{\text{imag}} \quad (\text{G.8})$$

$$\langle \delta^{\text{real}}(\mathbf{k}_1) \delta^{\text{real}}(-\mathbf{k}_2) \rangle + \langle \delta^{\text{imag}}(\mathbf{k}_1) \delta^{\text{imag}}(-\mathbf{k}_2) \rangle = F(\mathbf{k}_1, \mathbf{k}_2) \delta(\mathbf{k}_1 + \mathbf{k}_2) \quad (\text{G.9})$$

$$= \langle \delta(\mathbf{k}_1) \delta^*(-\mathbf{k}_2) \rangle, \quad (\text{G.10})$$

thus we have the form

$$\langle \delta(\mathbf{k}_1) \delta(\mathbf{k}_2) \rangle = F(\mathbf{k}_1, \mathbf{k}_2) \delta(\mathbf{k}_1 + \mathbf{k}_2), \quad (\text{G.11})$$

consistent with equation (1.94). Rewriting (G.5)

$$G(k_1, \dots, k_n) = \prod_{ij} \exp \frac{1}{2} \langle x_i x_j \rangle (ik_i)(ik_j) \quad (\text{G.12})$$

$$= \prod_{ij} 1 + \left[\frac{1}{2} \langle x_i x_j \rangle (ik_i)(ik_j) \right] + \frac{1}{2!} \left[\frac{1}{2} \langle x_i x_j \rangle (ik_i)(ik_j) \right] \left[\frac{1}{2} \langle x_k x_l \rangle (ik_k)(ik_l) \right] + \dots \quad (\text{G.13})$$

To find $\langle x_1 \dots x_n \rangle$ where n is even, the result will be a product of $\langle x_i x_j \rangle$ s. To find $\langle x_1 \dots x_n \rangle$ for n odd, $(-1)^n \frac{\partial^n G}{\partial k_1 \dots \partial k_n} \Big|_{\mathbf{k}=0}$ will be zero. Therefore, for a multivariate, independent Gaussian distribution with zero mean, the quantity $\langle \delta(\mathbf{k}_1) \delta(\mathbf{k}_2) \delta(\mathbf{k}_3) \rangle = (2\pi)^3 B(\mathbf{k}_1, \mathbf{k}_2, \mathbf{k}_3) \delta_D^3(\mathbf{k}_1 + \mathbf{k}_2 + \mathbf{k}_3)$ will be zero.

Appendix H

The Thermal Property of the CMB

The average photon occupation number per mode, $\mathcal{N} = \langle N \rangle$ is given by the Planck function

$$\mathcal{N} = \frac{1}{\exp\left[\frac{\hbar\omega}{k_B T}\right] - 1}. \quad (\text{H.1})$$

Finding the number of modes in a box of side L , where L is large compared to scales of interest.

Conventional notation for waves, such as the radiation in the box, has the form $A \exp(i\mathbf{k} \cdot \mathbf{r})$ where the wave is the real part of the function. Convention also dictates that integers n , m and l count the number of waves in the box in each direction

$$\mathbf{k} = \frac{2\pi}{L} \begin{pmatrix} n \\ m \\ l \end{pmatrix}, \quad (\text{H.2})$$

so we have a 3D standing wave mode counter:

$$\mathbf{N} = \begin{pmatrix} n \\ m \\ l \end{pmatrix} \quad (\text{H.3})$$

thus

$$d^3 N = \frac{V}{(2\pi)^3} d^3 k \quad (\text{H.4})$$

$$= \frac{V}{(2\pi c)^3} \omega^2 d\omega d\Omega, \quad (\text{H.5})$$

where $d^3 k$ is expanded in spherical coordinates, and $\omega = ck$.

The energy per frequency mode, in unit volume, moving in any direction, is

$$u(\omega)d\omega = \begin{array}{cccc} \text{mean number} & \text{number} & \text{polarisation} & \text{energy} \\ \text{of photons} & \times \text{ of modes} & \times \text{ states} & \times \\ \text{per mode} & & & \text{of} \end{array} \quad (\text{H.6})$$

$$= \frac{1}{\exp\left[\frac{\hbar\omega}{k_B T}\right] - 1} \times \frac{V}{(2\pi c)^3} \omega^2 d\omega \times 2 \times \hbar\omega \times 4\pi \quad (\text{H.7})$$

$$= \frac{\hbar}{\pi^2 c^3} \frac{\omega^3 d\omega}{\exp\left[\frac{\hbar\omega}{k_B T}\right] - 1}, \quad (\text{H.8})$$

the Planck blackbody function.

We are assuming that the photons are free streaming and not interacting, therefore the photon number is conserved. The expansion of the Universe stretches the wavelength of a mode as

$$\lambda \propto a(t), \quad (\text{H.9})$$

where $a(t)$ is the expansion scale factor of the Universe. So the frequency, ω , varies as $\frac{1}{a(t)}$. The number of photons per unit volume with frequency ω in the range $d\omega$ is equation(H.8) divided by $\hbar\omega$. At some later time t' the Universe scale factor is a' .

$$n(\omega)d\omega = \frac{1}{\pi^2 c^3} \frac{\omega^2 d\omega}{\exp\left[\frac{\hbar\omega}{k_B T}\right] - 1}. \quad (\text{H.10})$$

π , c , \hbar and k_B are of course constant. The three quantities that change are ω , T and the number of photons per unit volume. The total photon number is conserved, therefore the number per unit volume at the later time is scaled by $\frac{1}{a^3}$.

$$n'(\omega')d\omega' = \frac{n(\omega)d\omega a^3}{a'^3} \quad (\text{H.11})$$

$$= \frac{A\omega'^2 d\omega'}{\exp\left[\frac{\hbar\omega'}{k_B T}\right] - 1} \left(\frac{a^3}{a'^3}\right) \quad (\text{H.12})$$

$$= \frac{A\omega^2 \left(\frac{a'^2}{a^2}\right) d\omega \left(\frac{a'}{a}\right)}{\exp\left[\frac{\hbar\omega a}{k_B a' T'}\right] - 1} \left(\frac{a^3}{a'^3}\right). \quad (\text{H.13})$$

Thus the blackbody behaviour is preserved, with temperature redshifted by $T' = \frac{T a}{a'}$.

Appendix I

The Silk Damping Scale

The Silk damping scale, λ_s , is a measure of the photon diffusion length before decoupling. Most of the Silk damping effects itself at decoupling. Before this time the photons are trapped within matter over- and under-densities along with the baryons. The mean free path of the photons, λ_γ , increases as the ionisation fraction grows. Estimating the mean of the square distance, $(\Delta d)^2$, travelled by a photon during a period of time, Δt :

$$\langle(\Delta d)^2\rangle \simeq N \frac{\lambda_\gamma(t)^2}{a(t)^2}, \quad (\text{I.1})$$

where N represents the mean number of collisions of a photon within the time interval, $\Delta t/\lambda_\gamma(t)$.

So, we can estimate the Silk damping scale by summing up the distance travelled by the photon up to the time of decoupling, t_{dec} , corresponding to 90% ionisation,

$$\lambda_s^2 = \int_0^{t_{\text{dec}}} dt \frac{\lambda_\gamma}{a(t)^2}. \quad (\text{I.2})$$

The Silk Damping Scale

The Silk Damping Scale is a measure of the damping of silk fibers. It is defined as the ratio of the damping to the stiffness of the fiber. The damping is measured by the loss of energy in a cycle of vibration, and the stiffness is measured by the force required to stretch the fiber. The scale is used to compare the damping of different silk fibers and to determine the effect of various factors on the damping of silk fibers.

The damping of silk fibers is affected by several factors, including the type of silk fiber, the length of the fiber, the diameter of the fiber, and the frequency of vibration. The damping of silk fibers is also affected by the environment in which the fiber is used, such as the humidity and the temperature. The Silk Damping Scale is a useful tool for comparing the damping of different silk fibers and for determining the effect of various factors on the damping of silk fibers.

Appendix J

Calculating the Variance of the Bispectrum Estimator

To test the Gaussian hypothesis, we need to quantify the variation in the quantity

$$D_\alpha = \frac{\text{Re}(\delta_{\mathbf{k}_1} \delta_{\mathbf{k}_2} \delta_{\mathbf{k}_3})}{(2\pi)^2 \left(\frac{L}{2\pi}\right)^2} \quad (\text{J.1})$$

$$= \frac{1}{L^2} \frac{1}{2} (\delta_{\mathbf{k}_1} \delta_{\mathbf{k}_2} \delta_{\mathbf{k}_3} + \delta_{\mathbf{k}_1}^* \delta_{\mathbf{k}_2}^* \delta_{\mathbf{k}_3}^*). \quad (\text{J.2})$$

Let

$$\delta_{\mathbf{k}_1} \delta_{\mathbf{k}_2} \delta_{\mathbf{k}_3} = z. \quad (\text{J.3})$$

The variance is $\sigma_D^2 = \langle D_\alpha^2 - (\overline{D_\alpha})^2 \rangle$. According the Gaussian hypothesis, $\overline{D_\alpha} = 0$,

therefore

$$\sigma_D^2 \propto \left\langle \frac{1}{4} (z^2 + 2zz^* + z^{*2}) \right\rangle \quad (\text{J.4})$$

$$= \frac{1}{4} \langle \delta_{\mathbf{k}_1} \delta_{\mathbf{k}_2} \delta_{\mathbf{k}_3} \delta_{\mathbf{k}_1} \delta_{\mathbf{k}_2} \delta_{\mathbf{k}_3} + \delta_{-\mathbf{k}_1} \delta_{-\mathbf{k}_2} \delta_{-\mathbf{k}_3} \delta_{-\mathbf{k}_1} \delta_{-\mathbf{k}_2} \delta_{-\mathbf{k}_3} + 2\delta_{\mathbf{k}_1} \delta_{\mathbf{k}_2} \delta_{\mathbf{k}_3} \delta_{-\mathbf{k}_1} \delta_{-\mathbf{k}_2} \delta_{-\mathbf{k}_3} \rangle. \quad (\text{J.5})$$

Wick's theorem states that a correlation can be expanded into a sum of its connected parts and all the permutations of its constituents in lower order correlations:

$$\begin{aligned} \langle \delta_{\mathbf{k}_1} \delta_{\mathbf{k}_2} \delta_{\mathbf{k}_3} \delta_{\mathbf{k}_4} \delta_{\mathbf{k}_5} \delta_{\mathbf{k}_6} \rangle &= \langle \delta_{\mathbf{k}_1} \delta_{\mathbf{k}_2} \rangle_c \langle \delta_{\mathbf{k}_3} \delta_{\mathbf{k}_4} \rangle_c \langle \delta_{\mathbf{k}_5} \delta_{\mathbf{k}_6} \rangle_c + \langle \delta_{\mathbf{k}_1} \delta_{\mathbf{k}_2} \delta_{\mathbf{k}_3} \rangle_c \langle \delta_{\mathbf{k}_4} \delta_{\mathbf{k}_5} \delta_{\mathbf{k}_6} \rangle_c \\ &+ \langle \delta_{\mathbf{k}_1} \delta_{\mathbf{k}_2} \rangle_c \langle \delta_{\mathbf{k}_3} \delta_{\mathbf{k}_4} \delta_{\mathbf{k}_5} \delta_{\mathbf{k}_6} \rangle_c + \langle \delta_{\mathbf{k}_1} \rangle_c \langle \delta_{\mathbf{k}_2} \delta_{\mathbf{k}_3} \delta_{\mathbf{k}_4} \delta_{\mathbf{k}_5} \delta_{\mathbf{k}_6} \rangle_c + \text{cyclic permutations}, \end{aligned} \quad (\text{J.6})$$

where the subscript c denotes a connected part.

For a Gaussian field the only non-zero parts of this expression have the form $\langle \delta(\mathbf{k})\delta(-\mathbf{k}) \rangle$ therefore for the equilateral case

$$\text{Var}(\text{Re } z) = \frac{1}{4} \times 2 \langle \delta(\mathbf{k}_1)\delta(-\mathbf{k}_1) \rangle \langle \delta(\mathbf{k}_2)\delta(-\mathbf{k}_2) \rangle \langle \delta(\mathbf{k}_3)\delta(-\mathbf{k}_3) \rangle. \quad (\text{J.7})$$

$$= \frac{1}{2} L^6 P^3(k) \quad \text{as } |\mathbf{k}_1| = |\mathbf{k}_2| = |\mathbf{k}_3| \quad (\text{J.8})$$

$$D_\alpha = \frac{\text{Re}(z)}{L^2}, \quad (\text{J.9})$$

therefore

$$\sigma_D^2 = \left(\frac{1}{L^2} \right)^2 \text{Var}(\text{Re } z) = \frac{L^2}{2} P^3(k). \quad (\text{J.10})$$

But it also has to be taken into account that we are calculating the variance of an average over a shell of N values. The above value is the variance of a single D_α . Using the central limit theorem gives the final size of the Gaussian error bar,

$$\sigma_{N-D_\alpha} = \frac{L}{\sqrt{2N}} P^{3/2}(k). \quad (\text{J.11})$$

However, when I calculated the bispectrum for the equilateral triangles, I did not assume isotropy of the distribution when calculating $[\delta(\mathbf{k}_1)]^3$. I used the values for $\delta(\mathbf{k})$ at each of the three triangle vertices to make sure not to lose any of the information about the density field in the data.

For the zero-area triangle case: $\text{Var}(\text{Re } z) = \text{equation (J.5)}$.

Again, from the Wick's theorem expansion the only Gaussian contribution is from the $2zz^*$ cross-term. But now $\mathbf{k}_2 = \mathbf{k}_3$ so as well as the

$$\langle \delta(\mathbf{k}_1)\delta(-\mathbf{k}_1) \rangle \langle \delta(\mathbf{k}_2)\delta(-\mathbf{k}_2) \rangle \langle \delta(\mathbf{k}_3)\delta(-\mathbf{k}_3) \rangle \quad (\text{J.12})$$

there is a term contributing which is

$$\langle \delta(\mathbf{k}_1)\delta(-\mathbf{k}_1) \rangle \langle \delta(\mathbf{k}_2)\delta(-\mathbf{k}_3) \rangle \langle \delta(\mathbf{k}_3)\delta(-\mathbf{k}_2) \rangle. \quad (\text{J.13})$$

Therefore

$$\text{Var}(\text{Re } z) = 2P(\mathbf{k}_1)P^2(\mathbf{k}_2) \quad (\text{J.14})$$

and

$$\sigma_{N-D_\alpha} = \frac{L}{\sqrt{N}} P^{1/2}(k_1)P(k_2). \quad (\text{J.15})$$

Appendix K

The Langevin Equation

The form of the Lagrangian for scalar field theory is often related to the *Landau Free Energy*, L , of statistical mechanics (LeBellac, 1991; Goldenfeld, 1992). The form of the equation of motion in equation (4.19) is a result of extending the analogy to dynamic critical phenomena. The rate of change of the order parameter of a statistical field, $\phi(\mathbf{x})$, of a system which is slightly out of equilibrium is

$$\frac{\partial\phi(\mathbf{x})}{\partial t} = -\Gamma\frac{\delta L}{\delta\phi(\mathbf{x})} + \eta(\mathbf{x}, t) \quad (\text{K.1})$$

where $\delta/\delta\phi(\mathbf{x})$ is a functional derivative with respect to ϕ , the first term on the right hand side results from a phenomenological assumption of generally linear response and Γ is a phenomenological parameter, and the second term is a *noise* term, $\eta(\mathbf{x}, t)$, which arises from the macroscopic degrees of freedom that make the dynamics not purely relaxational. This is known as the Langevin equation, analogously, once more, to the original form of this equation in statistical physics. The equation in statistical physics models the behaviour of a sufficiently small macroscopic particle immersed in a liquid, which exhibits a random behaviour of motion, *Brownian motion*.

Looking, for simplicity, at the problem in 1D. Consider a particle of mass m , whose centre of mass position is $x(t)$ and velocity is $v = dx/dt$, undergoing Brownian motion. Neglecting any gravitational, electromagnetic or other force fields external to the system and modelling all of the degrees of freedom of the system apart from x as a heat reservoir at temperature T , and the force exerted on the particle as $F(t)$:

$$m\frac{dv}{dt} = F(t). \quad (\text{K.2})$$

$F(t)$ will depend on the positions of many constantly moving particles, and will thus be a rapidly, and irregularly, fluctuating function of t . One can attempt to describe the behaviour of the particle in statistical terms by making it one of an *ensemble*. So we are looking at many similar systems of particles, each surrounded by a liquid heat bath acting with a force $F_i(t)$. If there are N such systems, the average force exerted on a particle in any system, i , of the ensemble at time t will be

$$\bar{F} = \frac{1}{N} \sum_{i=1}^N F_i(t). \quad (\text{K.3})$$

As $F(t)$ is a rapidly fluctuating function of time then, from equation (K.2), v also fluctuates in time, so writing the ensemble average of the velocity, $\bar{v} = v - v'$. $\bar{v}(t)$ will vary more slowly with time than $v'(t)$, as a result of the average, and $v'(t)$ will vary more slowly than $F'(t)$ because of the mass of the particle. The reverse relationship must, logically, apply. The interaction force, F , must itself be affected by the motion of the particle.

$$F = \bar{F} + F', \quad (\text{K.4})$$

again the prime representing the rapidly varying part of the function, and, if we assume no preferred direction, the average value of F' vanishes. Expanding \bar{F} in terms of \bar{v} gives

$$\bar{F} = -\alpha\bar{v}, \quad (\text{K.5})$$

where α is some positive friction constant which acts to decrease \bar{v} . Thus we will have

$$m \frac{d\bar{v}}{dt} = -\alpha\bar{v}, \quad (\text{K.6})$$

and, more fully,

$$m \frac{dv}{dt} = -\alpha v + F'(t), \quad (\text{K.7})$$

representing the combined effects of the interactions of the system as a dissipation term and a thermal fluctuation with mean zero. This is the Langevin equation of statistical physics.